MEMORIAL
U N I V E R S I T Y

Dipolar-Depletion: study of a field-tunable colloid-polymer system

by

© **Shivani Semwal**

A thesis submitted to the School of Graduate Studies in partial fulfillment of the requirements for the degree of Doctor of Philosophy.

Department of Physics and Physical Oceanography

Memorial University

May 2022

St. John's, Newfoundland and Labrador, Canada

Abstract

Colloidal gels are an important class of materials with mesoscale building blocks, and they have wide-ranging applications, from water purification to cement to biotechnology. However, the formation of colloidal gels is beset by inadequate control over phase behaviour and slow aging kinetics. In this work, we report on experiments that examine structure, structural relaxation and dynamics in colloid-polymer suspensions, with fine, tunable control: the concentration of non-adsorbing polymer controls the strength of a depletion attraction, and an external electric field induces dipolar interactions that are instantly switchable and tunable in strength. ßWith these switchable interactions, we have studied the "dipolar-depletion" phase diagram in real space via fluorescence confocal laser scanning microscopy. We show combining depletion with dipolar interactions, at lower polymer concentrations, lowers the field threshold for observing ordered sheet-like dipolar structures. At intermediate polymer concentrations, depletion-induced clusters suppress field-induced ordering. At high depletion strengths, we can create partially ordered gel states. We also quantitatively characterize the transition from reversible to irreversible structures, and use the cycling of the external field to accelerate aging in a gel-forming system. For processes that take months or years to study, such as the collapse of certain gels, such accelerated aging would prove extremely useful. In addition, we characterize our model system by measuring the Zeta potential and charge on the colloids that we use to study the phase diagram *via* both AC and DC microelectrophoresis. We compare AC and DC measurements and find that there is no electrode polarization effect in a partially polar solvent.

Dedicated to my late grandparents

Dada & Dadi

Lay summary

Colloids – mesoscale particles suspended in a fluid – are found in many forms, and their study is highly relevant for industrial applications. Colloidal studies can be conducted by finely tuning the particle interaction by altering the particle coating, solvent conditions, or solutes present.

Colloids are often seen as an experimental model systems to understand "phase transitions": how atoms and molecules crystallize or fail to crystallize. Importantly, it is also possible to form a gel from colloidal particles under certain conditions. Gels are a disordered network of particles. They have wide-ranging applications from water purification to cement to biotechnology but the formation of colloidal gels is beset by inadequate control over phase transitions and by very slow aging kinetics.

We have conducted experiments on a colloid-polymer mixture. The colloids are hard-sphere-like: we control the electrostatic screening length by adding salt, we measure it *via* the conductivity, and measure the colloid charge using AC microelectrophoresis. In our research, we create an experimental colloidal model system that combines two important interactions — depletion interactions (by adding polymer) and the dipolar interaction (by applying an external electric field) — and report a novel phase diagram. Depletion is an isotropic, short-ranged attractive interaction that gives rise to disordered cluster and gel states. Dipolar interactions give rise to anisotropic ordered structures; since they are electrically controlled, they are switchable and tunable. This provides fine, tunable control over colloidal phase transitions.

Using a field-induced tunable interaction, we show that we can accelerate the aging process in gels by cycling the field on and off. Our work is an example of how introducing novel combinations of interactions results in new phase behavior, leading the way for new classes of materials.

Acknowledgements

I would like to express my gratitude to my supervisors, Dr. Anand Yethiraj and Dr. Ivan Saika-Voivod. This thesis would not have been completed without your invaluable supervision, support and guidance. I enjoyed and learned a lot from the numerous and often long discussions we had. I can not imagine having better supervisors and mentors for my Ph.D. Your advice on research as well as on my career has been invaluable.

I would also like to thank my supervisory committee Dr. Kris Poduska and Dr. James LeBlanc, for their insightful comments and questions. My sincere thanks goes to Dr. Alfons van Blaaderen for collaborating with us and allowing me to conduct research in their lab at Utrecht University in the Netherlands. I thank Anna Nikolaenkova for showing me how to perform microelectrophoresis experiments and preparation of the sample cell. I have significantly benefited from our valuable discussions.

I want to thank many people who contributed to the research through helpful discussions and other ways. I thank Dr. Valerie Booth for giving me access to the biochemistry lab to use the DLS equipment. Lars Kurandt-Jaeger from Anton Paar for a loan of the refractometer to measure the refractive index. I also thank Dr. Celine Schneider for training me to use NMR. Derrick P. Earle for his help in preparing the sample cell for the electrophoresis experiment. Venky and Yanitza, for their assistance in both NMR and rheology experiments. Fred Perry for his technical support in the lab. I am also very grateful to John Jerrett for helping me recover lost data from the corrupted external hard drive.

I thank all my friends in St. John's for a cherished time spent together and for making me feel at home. I am thankful to Kanachi for her companionship and the

v

Statement of contribution

The experiments and analysis discussed in this thesis represent the work that I carried out during my Ph.D. My supervisors, Dr. Anand Yethiraj and Dr. Ivan Saika-Voivod, have contributed to the work undertaken as a part of this thesis.

The manuscript, *"Tunable colloids with dipolar and depletion interactions: towards field-switchable crystals and gels"* that include results from Chapters 3 and 4, is submitted to *Physical Review X*.

Table of contents

List of tables

List of figures

xiii

List of symbols

A amplitude
a particle radius
c_p polymer concentration
c^* overlap polymer concentration
c_s salt concentration
c_i concentration of ions
D_0 diffusion coefficient
d_c cut-off distance
D_α generalized diffusion constant
E field strength
e elementary charge
f frequency
$g(r)$ radial distribution function
k_B Boltzmann constant
M dimensionless mobility
M_w molecular weight of the polymer
N_n number of neighbors
N_A Avogadro number
$P(x)$ probability distribution of displacements
r distance between the particle centers
R_g radius of gyration
R_H hydrodynamic radius
T Temperature
t time
U interaction potential
V_{ex} escluded volume
v_e electrophoretic velocity
v velocity
v_p particle velocity
v_l liquid velocity

List of symbols

z_s stationary layer

z depth

Z charge

α anomalous exponent

ϵ_o permittivity of vacuum

ϵ_s dielectric constant of the solvent

ϵ_c dielectric constant of the particle

ζ zeta

η viscosity

κ^{-1} Debye screening length

Λ^0 molar conductance

λ_B Bjerrum length

λ dipolar strength parameter

μ_e electrophoretic mobility

ξ polymer to colloid size ratio

ρ density

σ conductivity

σ_c diameter of a colloid

σ_p diameter of a polymer

τ structural relaxation time

ϕ volume fraction

ψ_s bond order parameter

Ψ dimensionless zeta potential

List of abbreviations

AO	Asakura and Oosawa
bcc	body-centred cubic
bco	body-centred orthorhombic
bct	body-centered tetragonal
CHB	cyclohexyl bromide
CLSM	Confocal laser scanning microscopy
Decalin	decahydronapthalene
DCG	dipolar chain gel
DID	depletion-induced disordering
DIO	depletion-induced ordering
DLS	dynamic light scattering
DLVO	Derjaguin, Landau, Verwey and Overbeek
E.F.	Electric Field
fcc	face-centred cubic
IDL	Interactive Data Language
ITO	indium- tin-oxide
MSD	mean-squared displacement
NA	numerical aperture
NBD	7-nitrobenzo-2-oxa-1,3 diazole
NMR	neutron magnetic resonance
PB	Poisson-Boltzmann
PS	polystyrene
PHSA	poly-12-hydroxystearic acid
PMMA	poly(methyl methacrylate)
TBAB	tetrabutylammonium bromide

Chapter 1

Introduction

1.1   Colloids

Colloids are particles that undergo Brownian motion in a fluid phase. The random motion resulting from the collision between the molecules in the solvent and colloidal particles due to thermal motion is called Brownian motion. This phenomenon was first observed by Robert Brown in 1827 when studying small pollen grains in water under a microscope [3]. Later, in 1905, Albert Einstein provided a theoretical explanation for the Brownian motion in terms of statistical fluctuations [4]. The size of colloidal particles ranges from nanometres to a few microns. In this size range, Brownian motion is always important, and enables colloids to effectively sample configurations.

A colloidal suspension is kinetically stable when colloids do not aggregate in a suspension. Whether the colloidal particles aggregate or not is determined by the combination of attractive and repulsive forces. The van der Waals force is responsible for the attraction between the colloids and causes them to coagulate. In a colloidal system, the attraction between particles results from the coupling between fluctuating dipoles, whose magnitude depends on the polarizability of a material [5]. Therefore,

colloidal particles are always dispersed in a refractive index matched solvent to minimize such interaction. Another advantage of a refractive-index matched system is that it suppresses the scattering of light and thus allows confocal microscopy studies of colloidal suspensions. Colloids can be sterically stabilized by grafting the surface of the particles with polymer "hairs" that prevents the colloids to aggregate. These polymer hairs on two colloidal particles are repulsive in a good solvent for the polymer. They can also be charge-stabilised: this results in repulsion between the colloids. In the 1980s, sterically stabilized poly(methyl methacrylate) (PMMA) spheres were prepared that behaved like hard spheres and equilibrium phase behavior was observed [6].

Colloids are of interest from a fundamental point of view as they can be used as an experimental model system to mimic atomic systems [7]. Unlike atoms, micron-scale colloids have a typical length scale comparable to the wavelength of visible light: this makes them accessible for microscopy and light scattering experiments. Also, the real-space structure and real-time dynamics of colloids can be relatively easily obtained experimentally due to their large size compared to atoms. In this thesis, confocal microscopy is used as the main experimental technique to study the colloidal system in real-time, real space and at a single-particle level.

Over the past decades, colloids have stimulated interest and shed light on fundamental problems of condensed matter physics, including the kinetics of crystallization and the nature of glassy states [7, 8, 9, 10]. Self-assembling colloidal particles thus provide a fascinating experimental model system for studying the fundamental aspects of the crystallizing behavior of atoms. Past studies of colloids have revealed many interesting phenomena, including a variety of crystal structures, crystal twinning and the glass transition [11]. Colloids behave like hard spheres in the absence of

all interactions. Computer simulations have predicted, and experiments have found, that for hard spheres, a fluid phase exists at low particle volume fractions (ϕ) and for $0.494 < \phi < 0.545$, the fluid and the crystal coexist. Above $\phi = 0.58$, an amorphous or glass phase is observed [12]. A very productive synergy between simulation and experiments has been developed in colloidal self-assembly studies.

1.2 Colloidal Interactions

Colloidal particles dispersed in a sufficiently polar solvent acquire a charge either due to dissociation of surface groups or due to adsorption of ions from the solvent onto the surface of the particles. If the surface of the colloidal particle is negatively charged, free negative ions in the solvent are repelled from the particle surface while positive ions are attracted towards the surface. Thus, a charged colloid is surrounded by a diffuse cloud of oppositely charged micro-ions also called as counterions. The surface charge and the counter-ions around the particles forms the electric double layer. The concentration of counterions is high close to the particle due to strong electrostatic interactions between the charge on the particle and ions.

The suspension of charged colloids is often described by a screened Coulomb potential, or equivalently, a Yukawa potential $\approx e^{-\kappa r}/r$, where r is the distance between the centre of the two colloidal particles and κ measures the effectiveness of the screening and is the inverse of the Debye screening length [13, 14, 15]. In the experimental system studied in this thesis, van der Waals interactions are likely smaller than $k_B T$. Their magnitude is somewhat reduced because our particles are sterically stabilized and the refractive index closely matches with the solvent.

The interaction between hard sphere colloids with diameter σ_c can be determined

using linearization of the mean-field Poisson-Boltzmann (PB) theory used by Derjaguin, Landau, Verwey and Overbeek (DLVO) [16, 17]

$$\beta U(r) = \begin{cases} U_c \frac{\exp[-\kappa \sigma_c (r/\sigma_c - 1)]}{r/\sigma_c}, & r \geq \sigma_c \\ \infty, & r < \sigma_c, \end{cases} \tag{1.1}$$

where $U(r)$ is a short range repulsive potential, $\beta = 1/k_B T$ with k_B, the Boltzmann constant and T, the absolute temperature and U_c is the potential at contact. The potential in contact can in turn be written as

$$U_c = \frac{Z^2 \lambda_B}{(1 + \kappa \sigma_c/2)^2 \sigma_c}, \tag{1.2}$$

where Z is the charge of the colloids and λ_B is the Bjerrum length of the suspending medium. Next, one can write an expression for the Bjerrum length,

$$\lambda_B = \frac{e^2}{4\pi \epsilon_s \epsilon_0 k_B T}, \tag{1.3}$$

with e the elementary charge, ϵ_s the relative dielectric constant of the solvent and ϵ_0 the permittivity of vacuum. The Bjerrum length is the distance at which the electrostatic interaction energy between two elementary charges is comparable to the thermal energy, $k_B T$. For the system used in this thesis (PMMA in CHB-decalin), $\lambda_B = (9.2 \pm 0.5)$ nm.

Finally, the Debye screening length is given by,

$$\kappa^{-1} = (8\pi \lambda_B c_s)^{-\frac{1}{2}}, \tag{1.4}$$

where c_s is the concentration of the salt. The κ^{-1} is the thickness of the double layer surrounding a colloidal particle and also a measure of the interaction range between two colloids. In our system κ^{-1} has a value of 0.095 ± 0.005 μm and $\sigma_c = 1.3$ μm. Typically, charged colloids of diameter σ_c can reasonably be treated as hard spheres if $\sigma_c \gg \kappa^{-1}$ i.e. $\kappa\sigma_c \gg 1$; practically, a system with $\kappa\sigma_c \sim 10$ can be termed "hard-sphere-like".

Another advantage of using colloids as a model system is that the interactions between colloids can be tuned, for example, by adding salt to screen charges, by adding polymer to induce attractive "depletion" interaction [18, 12, 19, 20] or by using various other methods to produce anisotropic interactions [21, 22, 23, 24]. In Section 1.2.1 and 1.2.2, we further discuss the anisotropic dipolar interaction and polymer-induced depletion interactions in detail.

1.2.1 Dipolar Interaction

Due to their relatively large size, colloids can easily be influenced by an external field, like an electric field, a magnetic field or gravity. The application of an external electric field can be used to manipulate the interactions, dynamics and structure of colloids in a suspension. When an electric field is applied, colloidal particles acquire a dipole moment parallel to the field due to a dielectric constant mismatch between the particles and solvent. These induced dipoles are always aligned with the field (z-axis) as shown in Fig 1.1(b). At sufficiently large external electric field, the polarization of the colloids due to the field results in forces much stronger than the Brownian forces, and hence leads to structural transitions in the colloidal suspension [25, 26, 27]. Previously in experimental studies, at lower particle densities and sufficiently strong fields, formation of strings (chains) was observed [28, 29, 30, 31].
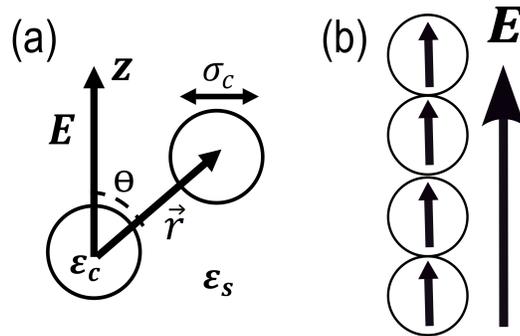
Figure 1.1: Dipolar Interaction. (a) application of electric field. (b) Dipolar chains along the direction of electric field (z axis).
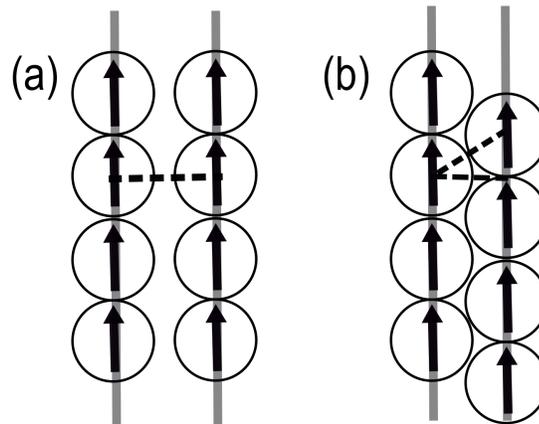
Figure 1.2: Stacked and staggered configuration. Two dipolar chains interacting through the (a) stacked interaction (b) the staggered interaction.

The interaction between two chains is attractive at close distances if they are half a particle diameter out of phase along the field direction z ("staggered") and repulsive if the particle positions in the chains are "in phase" or "stacked" along z (Fig. 1.2) [32]. The attractive interaction between chains leads to the formation of sheets (along the z axis), which are metastable. At high densities and high electric field (i.e., high dipolar strength), the body-centered tetragonal (bct) phase is known to be the stable structure. The bct structure manifests as an in-plane structure (perpendicular to the

electric field) with four-fold symmetry [26, 33, 34, 25, 35, 36]. The dipolar interaction is tunable in strength and instantly switchable. The dipole-dipole interaction between the particles separated by the displacement vector $R = (r, \theta)$ is expressed as [32],

$$\frac{U_{\text{dip}}(r, \theta)}{k_B T} = \frac{\lambda}{2} \left(\frac{\sigma_c}{r}\right)^3 \left(1 - 3\cos^2\theta\right). \tag{1.5}$$

Here, θ is the angle that r forms with the z axis along the direction of the electric field as shown in Fig 1.1(a) and λ is the dimensionless prefactor. λ is also called the dipolar strength parameter,

$$\lambda = \frac{4\pi\epsilon_0\epsilon_s\beta^2\sigma_c^3 E^2}{2k_B T}, \tag{1.6}$$

where E is the electric field, ϵ_0 is the permittivity of vacuum and ϵ_s is the dielectric constant of the solvent. The polarizability of the particles in the suspension is determined by β,

$$\beta = \frac{\epsilon_c - \epsilon_s}{\epsilon_c + 2\epsilon_s}, \tag{1.7}$$

where ϵ_c is the dielectric constant of the particles.

The dipole-dipole interaction energy scales with the particle volume (σ_c^3) and the square of the external electric field (E) (eq. 1.6). According to equation 1.5, colloids attract if $\theta < 54.7°$ or $\theta > 125.3°$, and repel otherwise.

The addition of long-range or electrostatic repulsion to the colloidal suspension can keep particles separated and stable against aggregation. Yethiraj *et al.* [35] and Leunissen *et al.* [37] explored ordered crystalline phases in real space using confocal microscopy in a charged and sterically stabilized colloidal suspension consisting of PMMA spheres, stabilized by polyhydroxystearic acid, and dispersed in a solvent

mixture of cyclohexyl bromide (CHB) and decalin. This solvent mixture matches both refractive index and density of the particle, allowing bulk 3D measurements with little sedimentation. They showed that combining electrostatic repulsion and field-induced dipolar interparticle interactions gives rise to a rich phase sequence that includes body centered tetragonal (bct), face-centred cubic (fcc), body-centred cubic (bcc) and body-centred orthorhombic (bco) phases.

Agarwal *et al.* reported that chains of particles aggregate to form a well-defined stable cellular network, possibly due to weak van der Waals attractions competing with dipolar interactions [38]. Field-switchable dipolar interactions have also been used to uncover path-dependent routes for crystal-to-crystal phase transformation kinetics in ultrasoft microgel colloids [39], and this is an example of how combinations of interactions help drive the development of new classes of materials. Field-induced interactions can be further useful for understanding and finding applications for electrorheological fluids. When an electric field at sufficiently high field strength is applied to a colloidal suspension with dielectric constant mismatch, the chain-like or columnar sructures formed results in changes to the rheological properties of the system. This is known as the electro-rheological effect [25, 34]. The electric field is used as a pseudo-thermodynamic temperature to study the dynamics of the melting transition of a bct crystal into a string fluid phase. The study of phase diagrams in such a system helps in understanding the mechanisms by which equilibrium and non-equilibrium phase transitions take place.

1.2.2   Depletion Interaction

The order-disorder transition of particles having purely repulsive interactions becomes richer when attractive interactions are added [11]. Such attractive interactions lead to

a gas-liquid phase transition. There are many ways to control colloidal interactions, discussed above in this section. In a colloidal suspension, the addition of electrolytes to screen the electrostatic repulsion between charged particles can induce aggregation due to van der Waals attractions. This onset of aggregation further obscures the equilibrium gas-liquid transition. An alternative approach to produce a weak, long-range attraction between colloids is to add non-adsorbing polymer to a suspension [11, 40]. The addition of a non-adsorbing polymer induces an effective "depletion" attraction between the particles, first predicted by Asakura and Oosawa [41], leading to a separation between colloid-rich (liquid-like) and colloid-poor (gas-like) phases. There is a spherical shell of thickness $\sigma_p/2$, referred to as a depletion zone, around the colloidal particles from which the mass centers of the polymers are excluded (Fig. 1.3). Each colloid reduces the free volume available to the polymer by an amount V_{ex},

$$V_{ex} = \frac{4\pi}{3}\left(\frac{\sigma_c}{2} + \frac{\sigma_p}{2}\right)^3 = \frac{\pi}{6}(\sigma_c + \sigma_p)^3, \tag{1.8}$$

When two colloidal particles approach each other sufficiently closely $(r < \sigma_c + \sigma_p)$, the individual excluded volumes overlap. This overlap leads to an increase in available free volume to the polymer. The extent to which this increase in volume available to the polymer is favoured entropically can be modelled through an effective interaction potential U, given by [42]

$$U = \begin{cases} \infty & r \leq \sigma_c \\ -\Pi V_{overlap} & \sigma_c < r \leq \sigma_c + \sigma_p \\ 0 & r > \sigma_c + \sigma_p \end{cases} \tag{1.9}$$

where Π is the polymer osmotic pressure, V_{overlap} is the overlap volume of the depletion zones, r is the distance between the particle centers, σ_{c} is the diameter of the colloidal particles, and $\sigma_p = 2R_{\text{g}}$ is the effective diameter of a polymer with radius of gyration R_{g}. The depletion interaction may thus be seen to emerge by the creation of a polymer "vacuum" in $V_{overlap}$, and thus an imbalance of the force on the colloids from the polymer osmotic pressure. The depletion interactions between colloidal particles is easy to manipulate by varying the interaction range set by the polymer size $(2R_{\text{g}})$ and depth of the potential, which is well controlled by the polymer concentration, c_{p}. In the Asakura and Oosawa model (AO-model), the colloids are considered as hard spheres and polymers as small spheres with no internal conformational degrees of freedom and are excluded from the colloids by a centre-of-mass distance of $(\sigma_c + \sigma_p)/2$. As polymer chains are added, attraction between colloidal particles increases causing the colloidal suspension to phase separate into a colloid-rich (colloidal liquid and crystals) and colloid-poor (colloidal gas) region at high polymer concentrations. Such microscopic interactions between particles can control the phase stability of colloid-polymer mixtures. According to the AO-model, the colloid-colloid attraction increases monotonically with c_{p}.

In the 1980s, Napper [43] and Vincent [44] suggested that the restabilization of the colloidal dispersions occurs at high polymer concentrations. This is due to the presence of the polymer chains that hinders colloid-colloid interactions and thus avoids the aggregation as c_{p} increases. It was further studied by Yethiraj *et al.* [45] where they modeled a colloid-polymer system such that colloid particles were treated as hard spheres and the polymer as a string of freely jointed hard spheres suspended in a solvent that doesn't interact with either colloids or the polymer. Their study proposed the existence of non-monotonic behaviour in the attraction between particles as c_{p}

increases. At a moderate c_p, particles aggregate whereas at high c_p, restabilization was observed [45]. Hence, it contradicts the AO approach at large c_p due to polymer-polymer interactions [46].
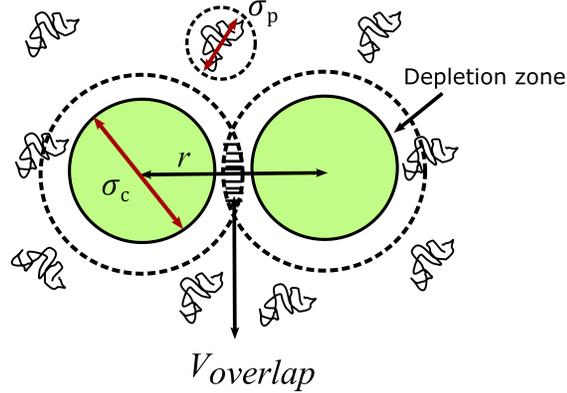
Figure 1.3: Depletion Interaction. Two hard spheres of size σ_c are surrounded by the depletants of size σ_p. The excluded volume per particle V_{ex} (eq. 1.8) is indicated by the dashed line (spherical shells) around the colloidal spheres (shown in green). The polymers impose an osmotic pressure on the colloids which results in an attractive interaction when there is an overlap of the excluded volumes ($V_{overlap}$).

In the absence of polymer, a fluid phase exists at a low volume fraction, $\phi < 0.494$, and for $0.494 < \phi < 0.545$, fluid and crystal coexist. For $\phi > 0.58$, an amorphous phase or a glassy state is observed [12]. In 1983, based on the AO model, Gast $et\ al$ [47] found that the addition of polymer expands the fluid-solid coexistence region when $R_g < \sigma_c$. In addition, for sufficiently large $\xi = R_g/\sigma_c$, a stable fluid-fluid and a three-phase coexistence of colloidal gas, fluid and solid was observed. For $\xi < 0.3$, the fluid-crystal coexistence region broadened, whereas a fluid-fluid phase transition was found for $\xi > 0.3$. For $\xi \approx 0.4$, a coexisting gas-liquid-solid three phase system was predicted based on the theory of Lekkerkerker $et\ al.$ (polymer-polymer interactions are ignored) [48]. This three-phase coexistence region was further experimentally demonstrated by the work of both Pusey $et\ al.$ [49] and Leal-Calderon $et\ al.$ [50]. Subsequently,

Ilett *et al.* [51] experimentally determined the phase diagrams of colloid-polymer mixtures with ξ = 0.08, 0.24 and 0.57. At ξ = 0.08, gas-solid coexistence and at ξ = 0.57, gas-liquid coexistence was observed that was consistent with the result from the theory of Lekkerkerker *et al.* [48]. At $\xi \approx 0.24$, a crossover between the two topologies, gas-solid coexistence and gas-liquid coexistence, was found.

In past years, phase diagrams with similar topologies as functions of ξ and c_p have been extensively studied theoretically, experimentally, and with computer simulations [18, 52, 53, 51, 54, 55, 19]. It was found that the phase diagram of colloid-polymer mixtures has a sensitive dependence on ξ and c_p. Dibble *et al.* [18] observed the structure of a colloid-polymer system on increasing the short-range interactions by varying c_p. Their experimental model system consisted of monodisperse sterically stabilized PMMA spheres dispersed in density and refractive index matched solvent mixtures (CHB and cis-trans decalin) that minimized the effects of sedimentation, and van der Waals forces. In such a system, where the screening parameter $\kappa\sigma_c$ = 1.39 (note: such a relatively small value means this is not a hard-sphere system), turning on polymer-induced short-range attraction, with ξ= 0.043, gives rise to a network of particles and clusters. The non-adsorbing polymer used as the depletant is monodisperse polystyrene (PS), a linear polymer, of molecular weight M_w=900,000 g/mol with $R_g = (43 \pm 1)$ nm. As the depletant concentration is further increased, clusters become increasingly immobile [18]. In this thesis, we have used confocal microscopy and a similar experimental model system with ξ= 0.066, and $\kappa\sigma_c$ = 13.7 $\pm$ 1.1 (which indicates a more hard-sphere-like system).

Campbell *et al.* [55] explored the phases as a function of the particle volume fraction ϕ_c and c_p. A phase change from a fluid of small, spherical stable clusters to the clusters forming a solid connected network of particles at high c_p was observed

[55]. This network of densely packed strings of particles with no change in local structure was identified as a gel [55, 18]. A substantial amount of work has been done to understand the dynamics of gels [56, 57, 20, 58]. Gels are arrested amorphous materials characterized by the presence of an open percolating network that forms at low volume fractions [51, 18, 55]. Controlling the state point by varying c_p in a colloid-polymer mixture results in a gel state at high c_p [18, 59]. The onset of cluster and gel formation in a system with short range attractions can be parameterized by ϕ_c, ξ and strength of attraction, U/k_BT. This framework for attractive colloids has been discussed by Lu *et al.* in Fig. 4 of Ref. [19] where three phases: fluid, fluid of clusters and gel phase were observed in a three-dimensional state diagram. For colloids with short-range attractions comparable to k_BT, the gelation boundary coincides with the equilibrium liquid-gas transition and gel formation appears to be driven by spinodal decomposition [59].

Colloidal gels have been extensively studied theoretically, experimentally and with computer simulations [42, 51, 53, 54, 18, 19, 59, 55]. Stronger inter-particle bonding results in non-equilibrium kinetics with power-law cluster size distributions [60, 58]. While there is some understanding of mechanisms of gel formation, gel aging (a slow dynamical process where the properties of a gel continue to change with time) and failure are less understood. There have been reports of multi-scale dynamics [20], an increase in gel strength up to the point of failure [61], and dynamic precursors for the catastrophic failure under constant load [62], but a coherent understanding is lacking.

While one can drive phase change or gelation with depletion interactions, obtaining the true interaction potential (U/k_BT) in such a system is a challenge. Interaction between particles results in a fluid to solid transition depending on the magnitude of U/k_BT. Teece *et al.* [2] and Dibble *et al.* [18] have reported values for U/k_BT by

using the AO theory [41] that seem unrealistic. These values are very high compared to the previous reported range of well depths obtained via experiments [63] as well as simulations [64] for the onset of aggregation and phase separation. In contrast, Lu *et al.* [19] experimentally determined U/k_BT using the cluster mass distribution of particles and report much more reasonable values (i.e., the right order of magnitude) that are in agreement with both experiments and simulations.

In this thesis, we discuss experiments on a unique set of colloidal interactions where field-induced dipolar and attractive depletion interactions are added together to hard sphere colloids. Introducing an interaction with fine, tunable control to a colloidal-polymer suspension increases the degree of control over phase behaviour. In such a system with multiple interactions, we have also experimentally set up a dynamical method to determine U/k_BT from a known $c_{\rm p}$ that defines the state in a phase diagram.

1.3   Thesis Outline

In Chapter 2, we focus on the properties of colloids suspended in a solvent of intermediate polarity and the tools we use to study them. In Chapter 3, we report experiments and analysis of the phase behaviour while varying both the polymer concentration (depletion interactions) and field strength (dipolar interactions). We study the phase transitions in the dipolar-depletion phase diagram where the external electric field is used as a switch to reversibly and repeatedly change phase in a sample. On applying switchable dipolar interactions to depletion colloids, we report a new "dipolar-depletion" phase diagram (Chapter 3). In this phase diagram, we encounter both an ordering regime where depletion attraction results in stronger

dipolar ordering, and an inverted ordering regime where stronger depletion attraction results in disordering. In Chapter 4, with the help of a control parameter i.e., an external electric field, we probe reversibility in both the ordered and disordered regime in the phase diagram. We also accelerate the aging phenomenon by cycling through the field. Here, an external field is used as a switch to achieve reversible control of interparticle interactions such that we can cycle through a phase transition several times, resulting in better quantitative studies of phase transition kinetics (Chapter 4). To further investigate aging in our system, we also study the dynamics that show an interesting transition from a liquid-like to a gel-like behaviour. We also measure the charge on colloids that we use to study the phase diagram in Chapter 3 and 4. In Chapter 5. we discuss a technique called micro-electrophoresis that we use to measure charge in our refractive index matched system. We use two different micro-electrophoresis methods i.e., AC and DC. We compare these two methods to understand the polarization effect in a non-aqueous solvent by measuring the velocity v of colloids in an electric field E and compute the electrophoretic mobility (μ_e) as a function of frequency.

Chapter 2

Characterization and experimental techniques

2.1 Introduction

In the experiments discussed in this thesis, we use fluorescent-labeled polymethyl methacrylate (PMMA) spherical colloids suspended in the solvent mixtures of cyclohexyl bromide (CHB) and cis-trans decahydronapthalene (decalin). The density of the solvents is matched with the particle density by tuning the mass ratios of CHB and cis-trans decalin to reduce the sedimentation. At density matching, the refractive index of the solvent mixture and PMMA particle is nearly identical. This minimizes the light scattering and fluorescence confocal microscopy can be used to look into the bulk of such a suspension. Therefore, PMMA colloids suspended in such a non-aqueous solvent mixture have been used widely as a model system in colloid science.

This chapter outlines the properties of PMMA and the solvent mixtures of CHB and decalin that are being extensively used in the experiments described in other

chapters. It also addresses experimental techniques and particle tracking methods used for the characterization and analysis. The particle tracking method is used to extract the two dimensional (2D) or three dimensional (3D) particle coordinates from confocal microscopy image stacks.

2.2 General properties of the solvent mixture

We use a refractive index and density matched system consisting of spherical PMMA colloids in a solvent mixture of CHB (80wt%) and cis-trans decalin (20wt%). To "clean" the solvent, we de-ionize the solvent before use by first adding activated alumina (Al_2O_3; 58A, $\sim$ 150 mesh, Sigma-Aldrich) and keep the solvent in a rotator for a day. We then centrifuge the solvent for 10 minutes such that alumina sediments to the bottom, and remove the clean solvent to another vial. After that, we add molecular sieves (4A, 10-18 mesh, Acros Organics) to the solvent and keep it undisturbed for 2 days [65]. The physical properties of the solvent mixture are summarized in the table below. The rheometer in our lab (MCR 301) was used to determine the viscosity of the solvent mixture. The refractive index measurement was done using a refractometer on loan from Anton Paar.

Table 2.1: General properties of a solvent at $T = 23°C$. The dielectric constant value is taken from the dielectric constant plot in Fig. 6 of Ref. [1]

solvent mixture	viscosity, η (mPas)	density, ρ (kg/l)	dielectric constant, ϵ_s	Refractive Index
CHB/cis-trans decalin	2.12 ± 0.05	1.17	6.1 ± 0.3	1.49 ± 0.01

2.3 Conductivity measurements on the solvent

The conductivity of a solvent is linked to the concentration of ionic solutes in the suspension. Therefore, it is related to the Debye-Hückel screening length, κ^{-1}.

2.3.1 Debye-Hückel screening length

An exponential distance dependence of the electric potential arises from the linearized Poisson-Boltzmann equation, with a characteristic lengthscale that is called the Debye–Hückel screening length (discussed in Section 1.2),

$$\kappa^{-1} = \sqrt{\frac{\epsilon_s \epsilon_0 k_B T}{2 N_A c_i e^2}}. \tag{2.1}$$

In the above, $e = 1.6 \times 10^{-19}$ C is the elementary charge, $N_A = 6.022 \times 10^{23}$ is Avogadro's number, $\epsilon_s = (6.1 \pm 0.3)$, the relative dielectric constant of the solvent, ϵ_0, the permittivity of the vacuum (8.85×10^{-12} F/m) and c_i is the concentration of dissociated ions in the solvent. The ion concentration in a suspension is estimated from the conductivity by using the following relation,

$$c_i = \frac{\sigma}{\Lambda^0}, \tag{2.2}$$

where $\sigma = 18000 \times 10^{-12}$ S/cm (1 Siemen is 1 Ω^{-1}) is the conductivity and $\Lambda^0 = 22.65$ cm^{2}S/mol, is the molar conductance of the electrolyte at infinite dilution. The conductivity measurements are performed on a Scientifica model 627 conductometer. It works for conductivities ranging between 0.1 pS/cm and 20000 pS/cm. The solvent CHB with dielectric constant $\epsilon \approx 7$ can be classified as a partially-polar solvent in

which charge dissociation occurs spontaneously in comparison to apolar solvents with $\epsilon \approx 2$ [65]. The ionic species H^+ and Br^- present in CHB arise from a partial decomposition of CHB and are the major species that contribute to the conductivity [66, 65]. We use available literature values to obtain a rough estimate for Λ^0 for HBr in CHB by using Walden's rule [67]. Walden's rule states that the product of viscosity η and Λ^0 for a solvent is the same for different solvents.

$$\Lambda_1^0 \eta_1 = \Lambda_2^0 \eta_2, \tag{2.3}$$

where Λ_1^0 is the (unknown) molar conductance in CHB, Λ_2^0 is the (known) molar conductance in reference solvent 2 and η_1 and η_2 are the viscosities of the respective solvents. Here, the reference solvent 2 is ethanol ($\Lambda_2^0 = 88.9$ cm^{2}S/mol and $\eta_2 = 1.08$ mPas) and the unknown Λ_1^0 of CHB is calculated using eq. 2.3 where $\eta_1 = 2.26$ mPas at $T = 293$ K is from the literature [68].

We determine the Debye length (κ^{-1}) of the solvent mixture containing 20 wt% cis-trans decalin in CHB using eq. 2.1. For $c_i = 7.95 \times 10^{-7}$ mol/L, we calculate $\kappa^{-1} = (0.095 \pm 0.005)$ μm.

2.3.2 Electrolyte screening by adding tetrabutylammonium bromide salt

Cleaning of the solvent significantly reduces the amount of HBr acid in the CHB, resulting in a long Debye length, up to $\sim$10 μm. However, for the experiments discussed in this thesis, hard sphere system like behavior is required. Such interactions were controlled by tuning the Debye screening length by adding salt, tetrabutylammonium bromide (TBAB). The concentration of TBAB added to the suspension is

73 ± 2 μM. The addition of salt increases the conductivity, resulting in smaller Debye lengths. The extent of screening in such a low-polar solvent can be determined by the electrolyte concentration.

2.4 Colloid-polymer suspension

2.4.1 Suspension Preparation

The solvent mixture of CHB/cis-trans decalin is added to dry PMMA particles in a small vial. The PMMA particles used in the experiments were synthesized by Andrew Schofield [69]. They are sterically stabilized with poly-12-hydroxystearic acid (PHSA). The suspension is then mixed on a vortex mixer for a few minutes until no trace of dry particles is visible. PMMA particles are porous, and when suspended in CHB/decalin, they swell slightly over time. Therefore, the suspension is kept for at least 2 days to equilibrate before an experiment. The diameter (σ_c) of PMMA in the CHB-decalin mixture used in the experiments is 1.3 μm. The suspension was found to be density and refractive index-matched in a mixture of 20 wt% cis-trans decalin in CHB. To induce a short-range attractive depletion interaction in a system, a stock solution of non-adsorbing polystyrene polymer was added to the dry PMMA colloidal particles and then the mixture is vortexed for 5-10 minutes. As reported in the literature, the solvent mixture of CHB-decalin is a good solvent for the polymer polystyrene [18]. In a good solvent, polymer behaves like a random coil whereas in a poor solvent a single polymer chain collapses [70].

2.4.2 Experimental characterization of polymer

The non-adsorbing polymer used to induce an effective attraction between colloids is monodisperse linear polystyrene (Pressure Chemical, Pittsburgh, PA) of molecular weight $M_{\mathrm{w}} = 9.0 \times 10^5$ g/mole and polydispersity $M_{\mathrm{w}}/M_{\mathrm{n}} \leq 1.10$. The range and magnitude of attraction interaction in a colloid-polymer suspension is controlled by varying polymer size i.e., radius of gyration, R_{g}, and concentration, c_{p}. Therefore, it is important to characterize the R_{g} and overlap concentration c^*, of the non-adsorbing polymer. The overlap concentration is one of the most important characteristic properties of a polymer solution. At concentrations $c < c^*$, the so-called dilute regime, the steric and frictional interactions due to neighboring polymer coils are negligible [71]. The concentration at which the imaginary spheres circumscribing neighbouring polymer coils are close enough to overlap is termed as the overlap concentration [72, 18],

$$c^* \cong \frac{3M_{\mathrm{w}}}{4\pi R_{\mathrm{g}}^3 N_{\mathrm{A}}}. \tag{2.4}$$

To calculate c^*, the R_{g} of the polystrene is determined by using two different techniques, nuclear magnetic resonance (NMR) and dynamic light scattering (DLS). Both these techniques measure the diffusion coefficient (D) of the particle. Then using the Stokes-Einstein equation, one can calculate the hydrodynamic radius (R_{H}),

$$R_{\mathrm{H}} = \frac{k_B T}{6\pi \eta D}, \tag{2.5}$$

where, k_B is the Boltzmann constant, T is the temperature and $\eta = (2.12 \pm 0.05)$ mPa.s is the solvent viscosity .
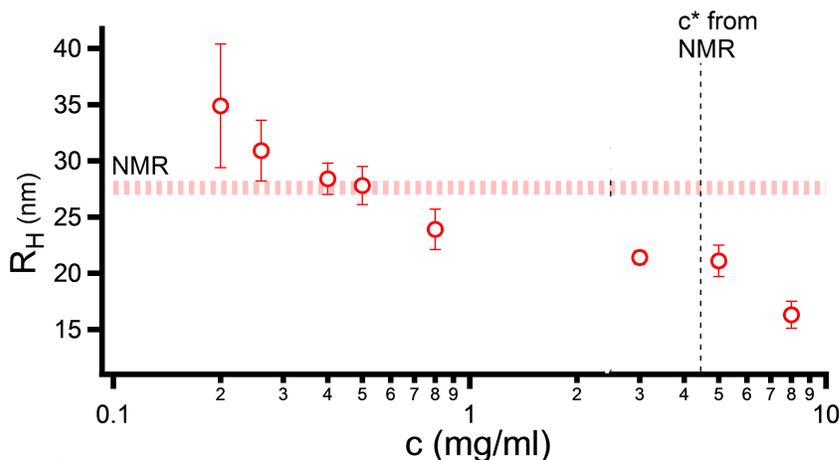
Figure 2.1: Measurement of the hydrodynamic radius (R_H) of the polymer (polystrene) using NMR yields a value of (27.5 ± 0.7) nm. This is consistent, within uncertainties, with the apparent radius from dynamic light scattering (DLS).

Pulse-field-gradient NMR measures the molecular self-diffusion coefficient whereas dynamic light scattering (DLS) measures the mutual diffusion coefficient. Interactions between the polymer molecules can be reduced by diluting the polymer solution. Hence, for DLS measurements, as the concentration is lowered, thus reducing the polymer-polymer interactions, the measured diffusion coefficient approaches the value expected for the self-diffusion coefficient. However, practically, reducing polymer concentration also increases the measurement errors.

For DLS experiments, we have used a series of polymer concentration as shown in Fig. 2.1. At higher polymer concentration, R_H is computed from the mutual diffusion coefficient, which is not the true polymer size. The R_H calculated at lower concentration is in agreement, within the uncertainty, with the value obtained from the NMR (self-diffusion coefficient), dashed line. The NMR experiment was carried out at $c = 0.8$ mg/ml. The hydrodynamic radius thus obtained is (27.5 ± 0.7) nm.

The solvent mixture of CHB and cis-trans decalin is a good solvent for polystyrene [18]. For a good solvent, R_g=1.59R_H [73, 74]. Therefore, the experimentally calculated value of R_g is (43 ± 1) nm. Using Equation 2.4, we find that c^*= 4.5 ± 0.1 mg/ml, not too different from the value, i.e., c^*= 5.3 mg/ml, reported in Dibble *et al.* [18].

2.4.3 Electric-field cell preparation
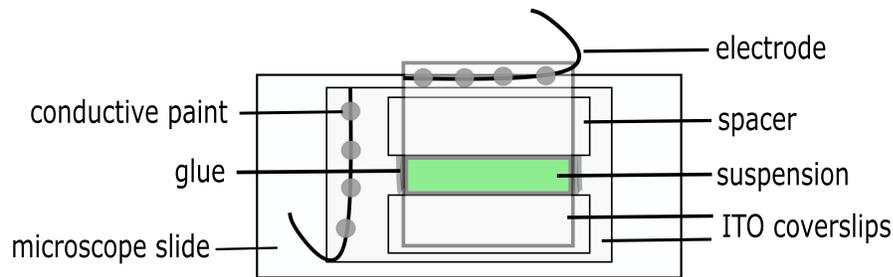
Figure 2.2: Schematic diagram of a top-view of an electric field cell. The sample space that is filled with colloidal suspension is shown in green.

We use electric field cells made of two optically transparent ITO (indium-tin-oxide) coated conducting slides with electrodes and a 0.15 mm thick glass spacer (a strip of #1 coverslip) between the conducting slides, shown in Fig. 2.2. A first conducting slide (conducting slide facing up) is glued to the microscopic slide using an ultraviolet curing optical adhesive (Norland Optical Adhesive 61) and dried under the UV lamp (UV lamp Spectroline model SB-100P) for 15-20 min. A second conducting slide (with conducting side facing down) is placed on top, with the spacer in between, is glued on. The connecting wires (0.05mm Ni 95/(Al + Mn + Si)5 thermocouple wire from Goodfellow) are glued to the conducting plates and dried under the UV lamp. Then the connection of wires to the conducting plate is made by using a conductive

silver paint from SPI supplies. The thickness of the sample is measured using a micrometer gauge. The thickness of the electric field cells used in the experiments is approximately in the range between 180 μm - 195μm. We apply an AC electric field, a sinusoidal AC voltage to the cell at frequency 1 MHz. The field strength is in the range between 0 V/μm and 0.53 V/μm (discussed in Chapters 3 and 4).

2.5   Confocal laser scanning microscopy (CLSM)

In 1957, Minsky first described the principle of confocal microscopy [75]. Confocal laser scanning microscopy (CLSM) has been used to study the fluorescent dyed colloid particles in a suspension discussed in this thesis. In CLSM, laser light is focused on the colloids using the objective lens which excites the fluorescent dye of colloids. The sample used for the experiments reported in this thesis was labelled with a fluorescent dye, 7-nitrobenzo-2-oxa-1,3 diazole (NBD), that is excited with the laser of wavelength 488 nm. It excites with blue light and emits green light. For illumination and detection, the fluorescent dye is matched with the appropriate sets of excitation and emission filters. The emitted light from the fluorescently labeled particles is then passed through a dichromatic mirror that transmits light of a longer wavelength and finally focused on a pinhole and detector as shown in Fig 2.3. The standard single-point-scanning confocal microscope uses two pinholes, unlike bright field microscopy. One of these pinholes is placed in the back focal plane of the objective in front of the light source, and the other one is in the focal plane in front of the detector. Both these pinholes lie in a focal plane that is conjugate to the plane of the sample in focus, hence it is called confocal. Therefore, by having a confocal pinhole, light excited from any point outside the focal plane is efficiently rejected by the detector. Thus,
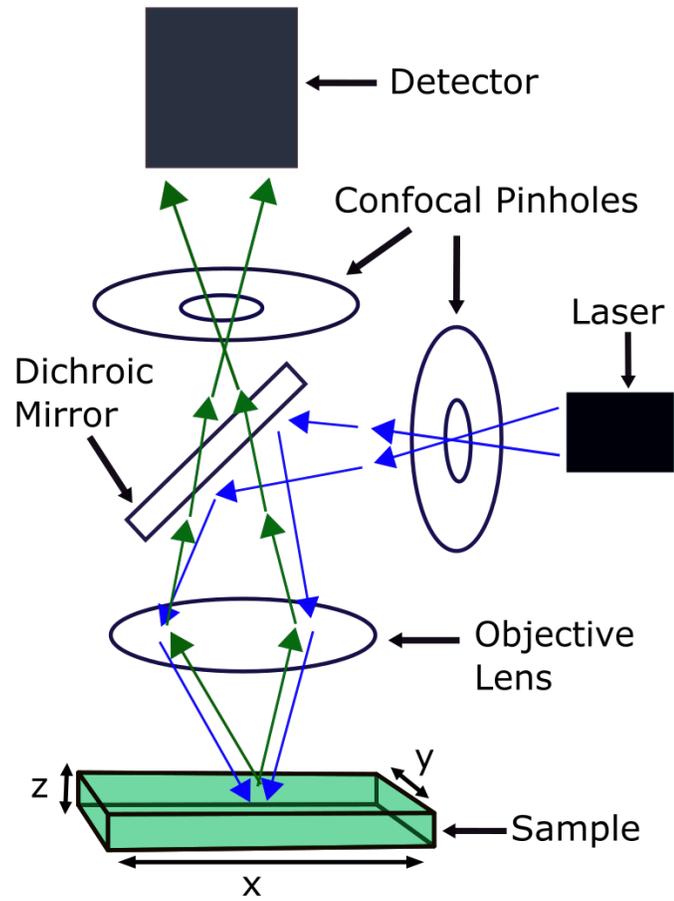
Figure 2.3: Schematic diagram of a confocal microscope

it reduces the noise due to other elements. A 2D image of a slice in the sample is made by lateral scanning the point through the focal plane at a particular depth. The sample is imaged point-by-point in a confocal microscope, and only a small portion of the sample is illuminated, excluding out-of-focus light. When a colloidal suspension is not refractive-index matched, multiple scattering makes the suspension opaque (an example is milk). Refractive index matching makes the suspension transparent, and the particles are only visible because of their fluorescent labeling. The depth of imaging in a refractive-index matched system containing fluorescently labeled particles is determined by the working distance of the objective lens. This technique can also be used for the 3D analysis of a colloidal suspension by scanning many thin sections through the sample at different focal depths [76, 77], thus allowing for both 2D time series (xyt) and 3D z-stack (xyz). All the images are recorded in one grey-scale image in the range from 0 to 256 for 8-bit recording. The confocal image stack series are then analyzed to extract the spatial coordinates of the particle using a particle tracking algorithm written in IDL (Interactive Data Language) [78].

We have used two confocal microscopes, namely a Nikon C1 confocal unit (configured on the front port of a Nikon Eclipse 80-i upright microscope), and a Visitech VT-Infinity3 confocal unit (configured on the left port of a Nikon TE-2000U inverted microscope). In the Nikon C1, there is a single pinhole that is scanned, and the detection is also done with a point (photomultiplier tube) detector that is placed behind a confocal pinhole. In the VT-Infinity3, there is an array of 2500 pinholes that are simultaneously scanned, and the detector is a fast (pco.Edge 5.5) scMOS camera. For regular confocal imaging of structure (Chapters 3 and 4) we used the C1 confocal, while in applications that require rapid imaging of dynamics (Chapter 5) we used the VT-Infinity3.
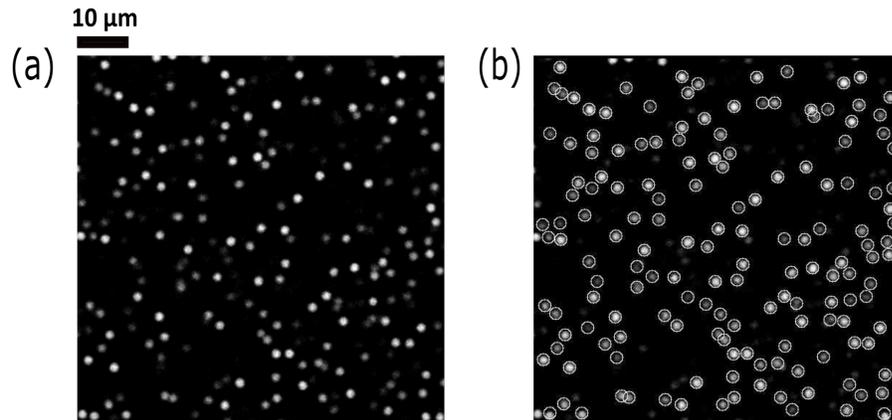
Figure 2.4: (a) Confocal image of PMMA in a solvent mixture (b) Analyzed image using particle tracking algorithm in IDL.

2.6 Particle Tracking

The microscopy images discussed in this thesis have been analyzed using particle tracking algorithms described by Crocker and Grier [78, 79]. Colloidal particles in a suspension are in Brownian motion such that their positions constantly change in time. Therefore, a sequence or series of images obtained from confocal microscopy is used to reconstruct the particle trajectories by extracting the particle coordinates. Particles need to be identified in successive frames to obtain good trajectories to study the dynamics of a colloid suspension.

For 2D analysis, xy coordinates and time are extracted from a stack of tiff images. One such image is shown in Fig. 2.4 (a). First, a stack of tiff images are read by using a function called readtiffstack.pro. Then, the positions of all the local intensity maxima in the image are identified using the feature finding function, feature.pro. A circular mask of diameter slightly greater than the particle diameter in pixels is placed around each of the local maxima, Fig. 2.4(b) and the x and y centroids of

particles are calculated within the circular mask. The x-y centroids are calculated in pixels using standard image convolution and the size of a pixel is used to convert the position coordinates to microns. The information about all the particle positions from feature.pro is then tracked using track.pro where the input is an estimated maximum distance moved by a particle in a single time interval. When there is a steady drift, for example, in the DC electrophoresis experiment (Chapter 5), the magnitude of the mean drift is subtracted from the position before determining the particle ID, but then is added on to calculate the mean square displacement. The maximum displacement moved in a single time interval is quickly estimated by eye during the image acquisition process using image visualization software, Fiji. The output from track.pro contains a list of data sorted into a series of trajectories, and track.pro also assigns a unique identity (id) number to each identified trajectory. The analysis for a 3D data set is done in a way that is analogous to that for a 2D + time dataset, with the correlation of features in subsequent frames being used to identify the z coordinate rather than to obtain dynamical information.

Chapter 3

The dipolar-depletion phase diagram

3.1 Introduction

In this chapter, we explore the phase behavior when polymer-induced depletion inter-
actions and field-induced dipolar interactions are added together to hard-sphere-like
colloids. In our experiments, we use a widely-used simple model system amenable to
both theory and experiment that is composed of micrometer-sized PMMA colloidal
particles and polystyrene (PS) polymer dispersed in a solvent mixture of CHB and
cis-trans decalin at a fixed $\phi = 0.10$ and $\xi = 0.066$. We have demonstrated exper-
iments on both colloidal suspension and colloid-polymer solution at different field
strengths. We establish a new *dipolar-depletion* phase diagram and quantify different
regimes in the phase diagram using the radial distribution function and local bond
order parameter in the 2D xy plane for field along $z-$direction.

This chapter is organized as follows. First of all, we describe our experimental
approach and data analysis methods in Sections 3.2 and 3.3, respectively. In Section
3.4, we discuss results with respect to the dipolar-depletion phase diagram (3.4.1) and
quantitative analysis of the phase diagram (3.4.2). Finally, we summarize our main

conclusions in Section 3.5.

3.2 Experimental Section

We use fluorescently labeled polymethyl methacrylate (PMMA) spheres obtained from A. Schofield (Edinburgh). The particles are fluorescently labeled with 7-nitrobenzo-2-oxa-1,3 diazole (NBD). The PMMA colloids of diameter $\sigma_c = 1.3$ μm are dispersed in a refractive index and density matched solvent mixture of CHB and cis-trans decalin. To obtain a hard-sphere-like system, we add salt, tetrabutylammonium bromide (TBAB), to the solvent mixture that screens the electrostatic interactions. Non-adsorbing polymer, polystyrene of molecular weight, $M_w = 9.0 \times 10^5$ g/mol, $R_g = (43 \pm 1)$ nm and $\xi = 2R_g/\sigma_c = 0.066$ is used as a depletant. The size of polystyrene is measured using dynamic light scattering (DLS) and nuclear magnetic resonance (NMR) (discussed in Chapter 2). The Debye screening length of particles, κ^{-1}, in a suspension with TBAB, is (0.095 ± 0.005) μm, and $\kappa\sigma_c = 13.7 \pm 1.1$. The conductivity of the solvent is measured using a Scientifica model627 conductivity meter.

We prepare colloidal suspensions with $\phi_c = 0.10$ by mixing dry particles with the stock solution of the polymer at different c_p and then vortexing the mixture for 5-10 min. Before experiments, a particle suspension is allowed to equilibrate for at least 3-4 days. The suspension is then transferred to an electric-field cell where two ITO (indium-tin-oxide) coated slides with electrodes and a 0.15 mm thick glass spacer in between is used (Fig. 2.2, Chapter 2). Samples are visualized using a Nikon C1 confocal microscope using a 60x magnification oil immersion objective lens with numerical aperture NA = 1.4 and an excitation wavelength of 488nm. Images are recorded at a scanning speed of approximately 1.49 frames per second where 2D xy

cross-section images have a field of view 256×256 pixels (1 pixel has a side length of 0.276 μm). The centres of particles are located using particle tracking routines by Crocker and Grier [78]. For an electric field experiment, the field strength E (peak amplitude of a sinusoidal oscillation at 1MHz wave) ranges between 0 V/μm and 0.53 V/μm. The electric field is generated using a function generator (Tektronix AFG 3022) at a constant peak-to-peak voltage, i.e, 5 V and a wide band amplifier (Krohn-Hite7602M) is used to vary the gain to yield a zero-peak potential difference ranging from 0 to 100 V, yielding a zero-peak field strength in the range between 0 V/μm and 0.53 V/μm.

3.3   Data Analysis

3.3.1   Radial distribution function

In a colloid-polymer mixture, fluid structure can be affected by adding anisotropic dipolar interaction to the system and varying c_p as well. The change in the structure is reflected in the radial distribution function ($g(r)$). For a dilute colloidal dispersion,

$$g(r) = \exp(-U(r)/k_B T) \tag{3.1}$$

where $U(r)$ is the pair interaction and $k_B T$ is the thermal energy. It gives information about the average spacing between the particles and thus, the structure of a system. We characterize the positional order through $g(r)$ by analysing the position of particles in two dimensions [78]. We compute the 2D $g(r)$, in the 2D xy plane of a 3D system where the electric field is applied along the z-axis, by analyzing a sequence of 100 images with a 256 × 256 pixels field of view at different field strengths. In the 2D
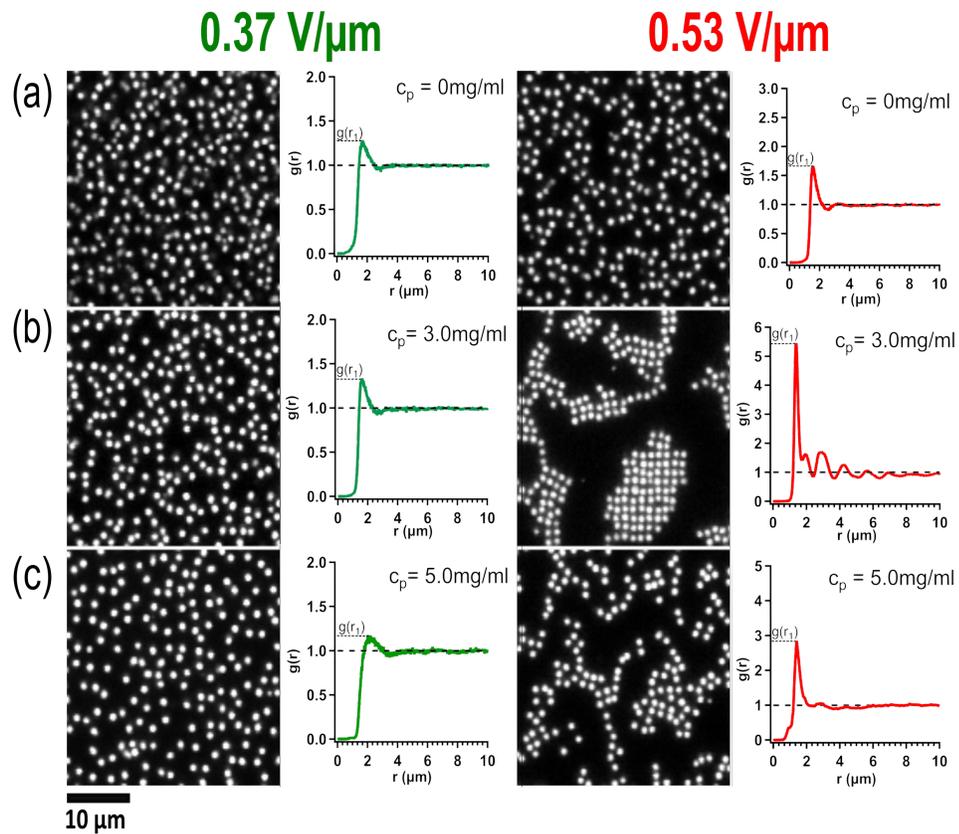
Figure 3.1: Radial distribution function ($g(r)$) at different field strengths (E). **a)** $c_p = 0$ mg/ml at $E = 0.37$ V/μm and 0.53 V/μm **b)** $c_p = 3$ mg/ml at $E = 0.37$ V/μm and 0.53 V/μm. **c)** $c_p = 5$ mg/ml at $E = 0.37$ V/μm and 0.53 V/μm. Height of the first peak of $g(r)$ denoted by $g(r_1)$ in the graphs varies E and c_p. Regions of interest shown are of size 128×128 pixels in the x-y plane with the field applied perpendicular to the plane of images.
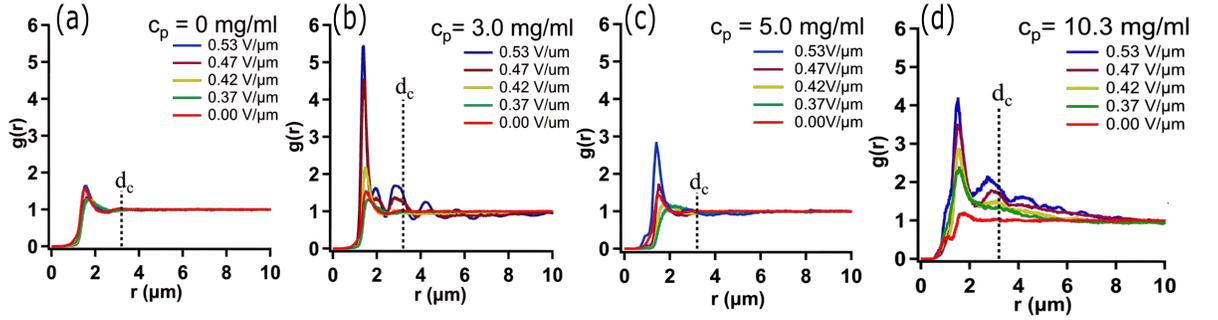
Figure 3.2: Field dependence of $g(r)$. Radial distribution function ($g(r)$) at different field strengths (E) and polymer concentrations **a)** $c_p = 0$ mg/ml **b)** $c_p = 3$ mg/ml **c)** $c_p = 5$ mg/ml and **d)** $c_p = 10.3$ mg/ml. The cut-off distance d_c (black dotted line) is optimally a value slightly less than the second $g(r)$ maximum.

$g(r)$ analysis, first, we count all particles that are in a spherical shell of thickness dr at a distance r away from a reference particle. This total count is further divided by the total number of particles (N) and then it is divided by the volume of the spherical shell which is $2\pi r dr$ for a two dimensional $g(r)$. Further, the calculated $g(r)$ is normalized by the particle number density. The resolution along the depth direction, i.e., along z, is not as good as the xy resolution due to the larger point spread function (PSF) along z. Therefore, at high fields when we have dipolar chains with particles in contact, we restrict ourselves largely to imaging in two dimensions.

Fig. 3.1 shows both 2D snapshots, for different c_p at field amplitudes $E = 0.37$ V/μm (left panel) and 0.53 V/μm (right panel), and the corresponding 2D $g(r)$, from which the height $g(r_1)$ of the first peak, at $r = r_1$, is determined. We observe, for $c_p = 0$ mg/ml, 3 mg/ml and 5 mg/ml, that $g(r_1)$ increases when the field is increased from $E = 0.37$ V/μm to $E = 0.53$ V/μm. The individual particles in the 2D snapshots are actually chains in the field direction (z-axis, into the page) as shown in Fig. 3.3 (b, right panel). The height of the first peak of the radial distribution $g(r_1)$ function quantifies the nearest neighbor particle in a first coordination shell.

In addition, Fig. 3.2 shows $g(r)$ for $c_p = 0$ mg/ml, 3 mg/ml, 5 mg/ml and 10.3 mg/ml at different E. For $c_p = 0$ mg/ml, there is an initial decrease in the height of the $g(r_1)$ peak, along with a small increase in the peak position $r = r_1$. This is likely because of the formation of dipolar chains, which would repel each other. At the highest field, however, the peak position shifts back towards lower r_1 and the peak height increases. This indicates the formation of chain-chain clusters, which require neighbouring chains to be offset in registry by half a particle diameter ("staggered" [32]). The chain-chain interaction is repulsive if the particle positions in the chains are "in phase" or "stacked" along z, while the interaction is attractive if they are half a particle diameter out of phase ("staggered"). At $c_p = 3$ mg/ml, 5 mg/ml and 10.3 mg/ml, $g(r_1)$ increases as field strength increases from 0 V/μm to 0.53 V/μm due the formation of ordered and disordered structures in the xy plane (discussed below in Section 4.4.1).

Further, we quantify the symmetry in a structure by considering the neighboring particles of a given particle. A cut-off filter is applied: the distance between two particles must be less than a cut-off distance d_c in order for them to be considered neighbours. The value of this cut-off distance is set to $d_c = 3.3$ μm $\approx 2.5 \times \sigma_c$ (Fig. 3.2); this value is obtained by examining the $g(r)$ at zero field and picking a value just less than the second maximum of $g(r)$ such that it also includes some second nearest neighbor particles. The sensitivity of this method was fine-tuned by using more than one d_c and then comparing images that are labeled with the obtained local order parameter with the actual image of particles. This is shown next.
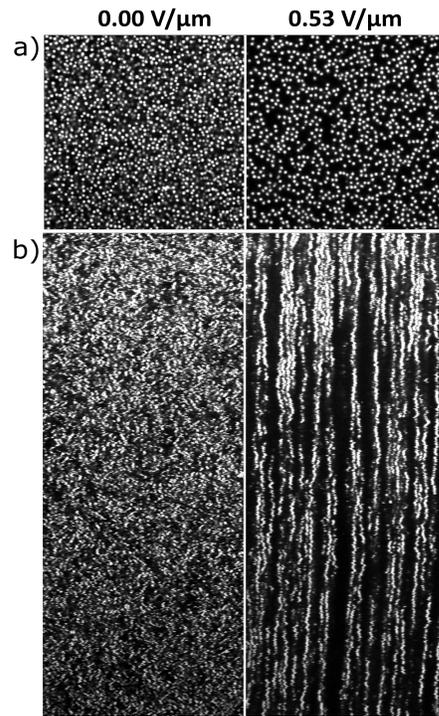
0.00 V/μm   **0.53 V/μm**

Figure 3.3: Microscopy images captured in the **a)** xy and **b)** xz plane for $c_\mathrm{p} = 0$ mg/ml at $E = 0.00$ V/μm and 0.53 V/μm respectively. At $E = 0.53$ V/μm particles form long chains along the direction of electric field.

5 μm
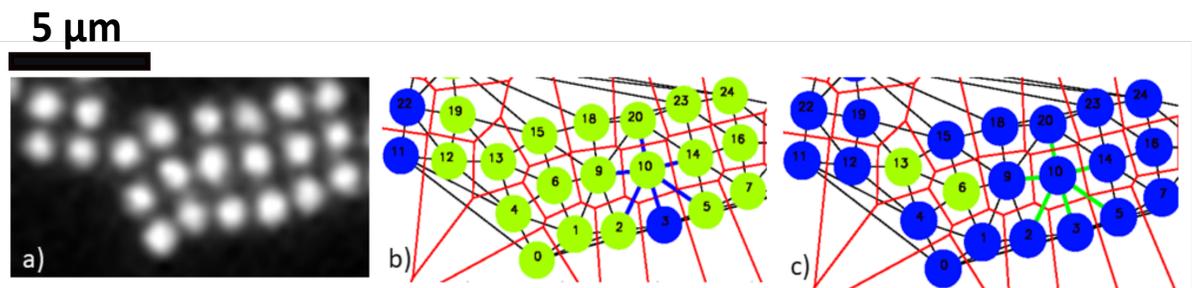
Figure 3.4: Identifying nearest neighbors using the Delaunay triangulation. **a)** 2D microscopy image of colloidal particles with a field of view 139×56 pixels (1 pixel = 0.276 μm) at $c_\mathrm{p} = 3$ mg/ml and $E = 0.53$ V/μm. Tracked particles are marked with an id. **b)** Nearest neighbors are identified using both the Delaunay graph (black) and Voronoi diagram (red). Local bond order parameter $\bar{\psi}_s$ when **b)** $s = 4$ and **c)** $s = 8$. Blue color particles indicates a high order parameter i.e., when $\bar{\psi}_s > 0.5$ and low order ($\bar{\psi}_s \leq 0.5$) is indicated by a green color.
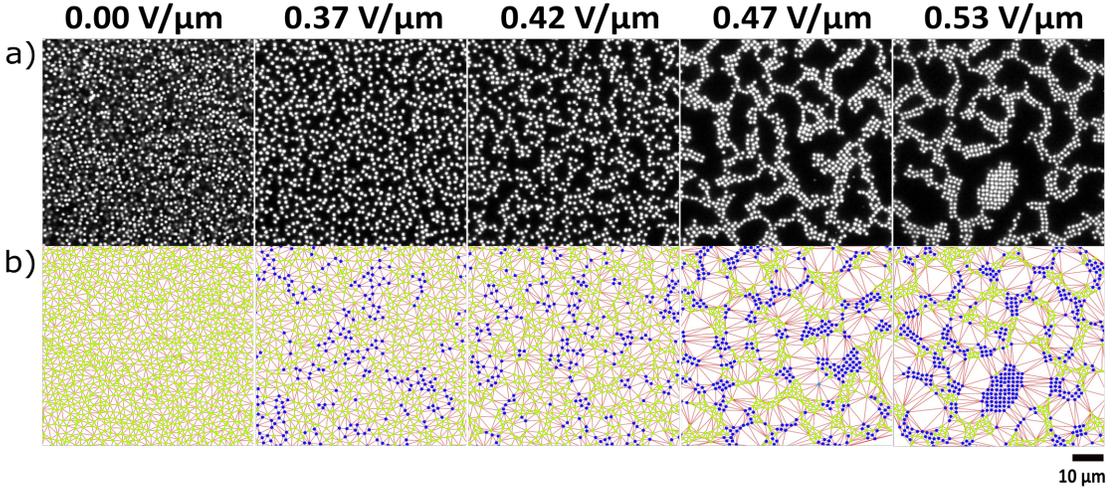
Figure 3.5: Bond order parameter ($\bar{\psi}_8$) for $c_p = 3$ mg/ml at different field strengths (E). **a)** 2D Images captured in the xy plane at different E with field of view 256×256 pixels **b)** Structure becomes more ordered, i.e., high 8-fold symmetry as E increases. Blue color denotes $\bar{\psi}_8 \geq 0.5$ and green indicates $\bar{\psi}_8 \leq 0.5$.

3.3.2 Bond order parameter

We assess the orientational order by determining the bond order parameter from the retrieved positions of the colloidal particles. The bond order parameter helps in distinguishing between a particle in the fluid and the solid phase by extracting information about the local symmetry around each particle [80, 81]. In our experiments, we determine the local order around particles at different c_{p} and E using the average bond order parameter [82]. We begin by defining a complex quantity for each particle k [36, 83],

$$\psi_s^k = \left| \frac{1}{N_k} \sum_{j=1}^{N_k} e^{is\theta_{kj}} \right|, \tag{3.2}$$

where N_k is the number of nearest neighbors of particle k, and θ_{kj} is the angle between the line connecting particle k to a neighbouring particle j and a reference axis, here

taken to be the x-axis. Applying the ideas of Ref. [82] to two dimensions, the average bond order parameter for each particle is then defined as,

$$\bar{\psi}_s(k) = \frac{1}{N_k + 1} \sum_{j=1}^{N_k+1} \psi_s^k.$$ (3.3)

The sum runs over all the nearest neighbors of particle k and particle k itself. Henceforth, we usually omit the argument of $\bar{\psi}_s(k)$, and simply write $\bar{\psi}_s$, understanding that it is a quantity defined for an individual particle. While we calculate $\bar{\psi}_s$ for $s = 2$, 4, 6, and 8, we find that $s = 8$ is a robust indicator of local 4-fold symmetry with disorder (Fig. 3.4) as it precludes the need to distinguish between the nearest and next-nearest neighbors [84, 85].

In order to identify the neighbors, we first perform a Delaunay triangulation [86]. In this process each particle coordinate is connected to its neighbors such that it forms triangles where no circumcircle of any triangle contains any particle coordinate. After this first step of identifying neighbors of particles, we use d_c obtained from $g(r)$ (Fig. 3.2) as a second parameter to further filter the non-neighbors. Fig. 3.4 shows the neighbors identified for a 2D microscopy image of particles, shown in Fig. 3.4(a), using both the Delaunay triangulation (black lines) and a Voronoi diagram (red lines). In the Delaunay triangulation, a 4-fold structure can sometimes encounter diagonal bonds as shown in Fig. 3.4(b) where, for example, particle 2 and 5 are diagonally connected to particle $k = 10$. These diagonal bonds can be accommodated by using $s = 8$ for 4-fold symmetry as shown in Fig. 3.4(c) [10, 36]. Green color particles indicate a disordered structure when $\bar{\psi}_s$ is less than a certain threshold parameter (t), that we set to be 0.5, and blue is for an ordered structure with high 4-fold symmetry where $\bar{\psi}_8$ is greater than t. In Fig. 3.4, where $t = 0.5$, it is clear that setting $s = 8$ does a notably better job of identifying regions with high four-fold symmetry.

We calculate $\bar{\psi}_8$ for each particle at different c_p and E. Fig. 3.5 shows more ordered structure with 8-fold symmetry i.e., a steady increase in regions with high $\bar{\psi}_8$ (blue particles) with increase in field. In particular, there is a sharp increase at $E = 0.47$ V/μm and 0.53 V/μm, compared with $E \leq 0.42$ V/μm.

We see in Fig. 3.4(b and c) that $\bar{\psi}_8$ captures the square symmetry of the bct crystallite rather well. Nevertheless, it can be seen that even in the samples of highest crystallinity (for example the right-most image in Fig. 3.5), a large fraction of the sample is composed of sheets (colored green or low $\bar{\psi}_8$ by the local bond order coloring). We thus find that the *fraction* of the image containing high-$\bar{\psi}_8$ order, denoted as f_8, is a very useful metric.

The fraction f_s is a global order parameter. Another global order parameter is

$$\langle \psi_s \rangle = \frac{1}{N^{\#}} \sum_{k=1}^{N^{\#}} \bar{\psi}_s(k),$$ (3.4)

where $N^{\#}$ would normally be the total number of particles in the image N. In our work, we find it useful to use an alternative, i.e., $N^{\#} = f_s N$. This follows the analysis and discussion in previous work on polycrystalline colloidal films [83]. In the bct crystals, e.g., in the right-most image in Fig. 3.4, the latter choice selects just the crystallites (blue particles) and not the sheets (green particles) joining the crystallites.

In summary, we characterize the structure of our experimental model system through a two-dimensional $g(r)$, $\bar{\psi}_s$, the fraction of particles in a 2D image with high $\bar{\psi}_s$, denoted as f_s, and $\langle \psi_s \rangle$ For detection of bct order in 2D images, we use $s = 8$.

3.4   Results and Discussion

In a colloid-polymer mixture, transitions between the fluid, cluster phases and the gel are governed by several factors [18, 19, 87, 88]. In our experiments, we vary c_p and the dipolar strength by changing the electric field E, but keep fixed both $\xi = 2R_g/\sigma_c = 0.066$ and $\phi = 0.10$.

3.4.1   Dipolar-Depletion Phase Diagram

We summarize the "dipolar-depletion" phase diagram, new to our experiments, in Fig. 3.6(a). With increasing c_p and at zero field (column 1 of Fig. 3.6(a)), one increases only the strength of the depletion interaction. This results in isotropic clustering of particles at larger c_p. In the rest of the phase diagram (columns 2 to 8) the depletion strength increases from $c_p = 0$ mg/ml to 10.3 mg/ml and the electric field increases from $E = 0.11$ V/μm, (2nd column from left) to 0.53 V/μm (right-most column). With increasing electric field, a subtle difference in focus is seen between $E = 0$ V/μm and 0.37 V/μm due to the formation of dipolar chains along the direction of electric field in the xz plane. In the latter case, most particles are simultaneously in focus. At field amplitudes of $E = 0.37$ V/μm or higher, each particle in the 2D field of view is a long chain in 3 dimensions (chains along z) as can be seen in Fig. 3.6(b) and (c).

As already hinted at in Fig. 3.1, there are two distinct dipolar-depletion regimes. The dilute polymer regime, $c_p < c^*$, where $c^* = 4.5$ mg/ml is the polymer overlap concentration for our system, and the semi-dilute polymer regime, $c_p > c^*$. Increasing the depletion strength, by increasing the polymer concentration from $c_p = 0$ mg/ml to
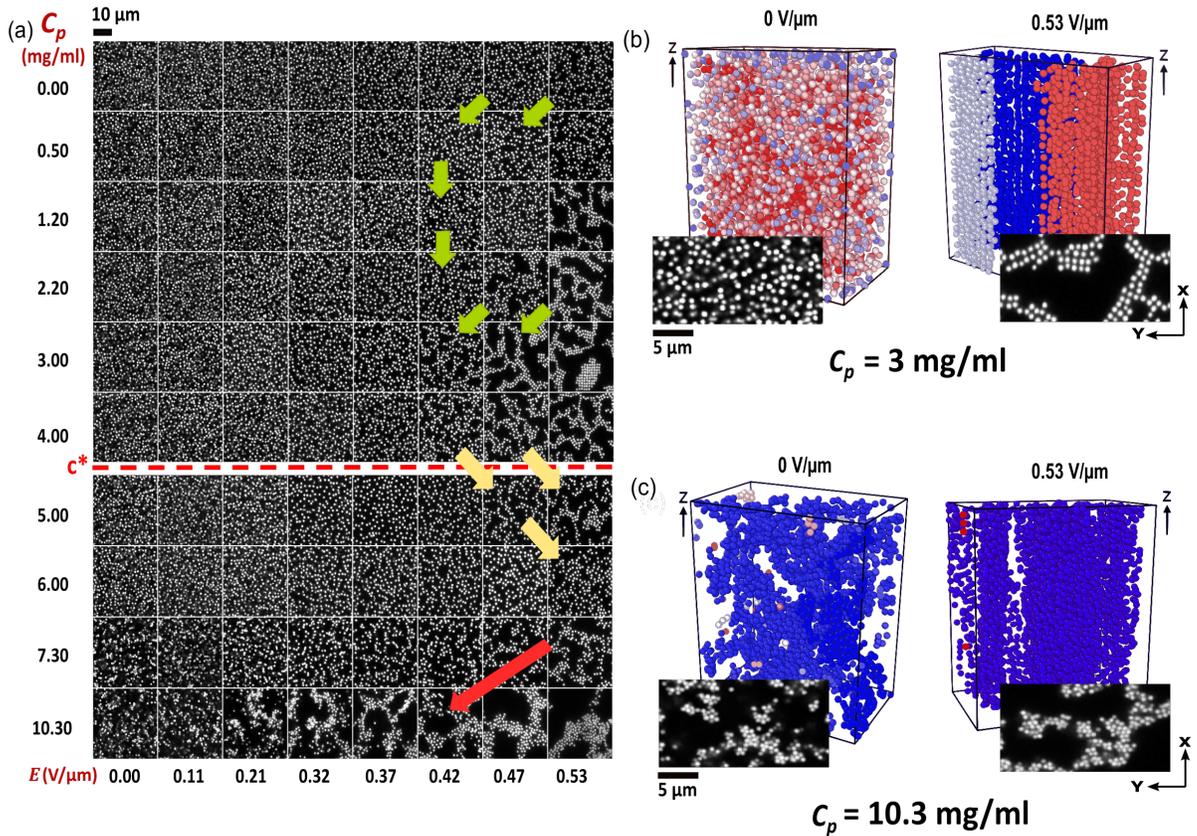
Figure 3.6: The dipolar-depletion phase diagram. **a)** 2D microscopy images of a colloid-polymer mixture as a function of polymer concentration, c_p and electric field strength, E. Each image ROI shown here is 128 pixels × 128 pixels (1 pixel = 0.276 μm). c_p increases from 0 mg/ml (top row) to 10.3 mg/ml (bottom row) as a function of external electric field (E) from 0 V/μm in the left-most column to 0.53 V/μm in the right most column. Green, yellow and red arrows qualitatively show the different regimes in the phase diagram and shifts in the field threshold (E) with c_p for observing ordered and disordered colloidal structures. Green and red arrows: field threshold lowers for $c_p = 0$ mg/ml to 3.00 mg/ml and $c_p = 7.3$ mg/ml to 10.3 mg/ml. Yellow arrows: field threshold increases for $c_p = 4.00$ mg/ml to 6.00 mg/ml. c^* (red, dashed line) is the overlap polymer concentration. **b)** 3D views $(20.24 \times 34.64 \times 40.63 \ \mu m^3)$ (generated using OVITO [89]) and inset, 2D confocal microscope images of the suspension, at $c_p = 3$ mg/ml for no-field (0 V/μm, left) and maximum field strength (0.53 V/μm, right) respectively. **c)** 3D view and 2D confocal image of a single spanning cluster at $c_p = 10.3$ mg/ml for 0 V/μm (left) and 0.53 V/μm (right).

3 mg/ml (Fig. 3.1), we see at $E = 0.53 \ V/\mu$m that the dipolar structure is enhanced and $g(r_1)$ increases from 1.6 at 0 mg/ml to 5.5 at 3 mg/ml. Curiously, increasing c_p from 3 mg/ml to 5 mg/ml results in a significant *decrease* in order and a lower value of $g(r_1)$ is observed at 0.53 V/μm.

For c_p between 0 mg/ml and 3 mg/ml (i.e., less than c^*) and $E > 0.42$ V/μm, more ordered clusters are observed as we increase c_p. In this regime, combining depletion with dipolar interactions enhances the formation of ordered structures i.e., the field threshold for the formation of ordered structures decreases as we increase c_p. This is indicated by green arrows in Fig. 3.6(a) where the field threshold is lowered for $c_p = 0$ mg/ml to 3 mg/ml. On the other hand, for 3 mg/ml $< c_p <$ 6 mg/ml and $E > 0.42$ V/μm, structural order decreases with increasing c_p and the field threshold for the onset of ordered structures increases: this is indicated by yellow arrows in Fig. 3.6(a).

A third structuring regime is observed at $c_p = 7.3$ mg/ml and 10.3 mg/ml. We observe clusters and individual particles coexist when no field is applied ($E = 0 \ \mu$m). At $E = 0.53$ V/μm, big clusters with larger voids are observed. Occurrence of these network of clusters and large voids is observed at lower field strength for c_p= 10.3 mg/ml, i.e., the increase in c_p *decreases* the field threshold for the formation of *disordered* clusters.

Therefore, we can visually classify the phase diagram at $E_{\max} = 0.53$ V/μm into 3 different regimes (Fig. 3.6(a). Different regimes are shown by green, yellow and red arrows in the phase diagram. We show, in Fig. 3.6(b, left), a 3D image of the colloid-polymer mixture in the fluid phase for a sample with $c_p = 3$ mg/ml at $E = 0$ V/μm. This fluid phase transitions to dipolar chains in the z direction and bct crystals in the xy plane (Fig. 3.6(b, right)) as field strength increases to 0.53 V/μm.
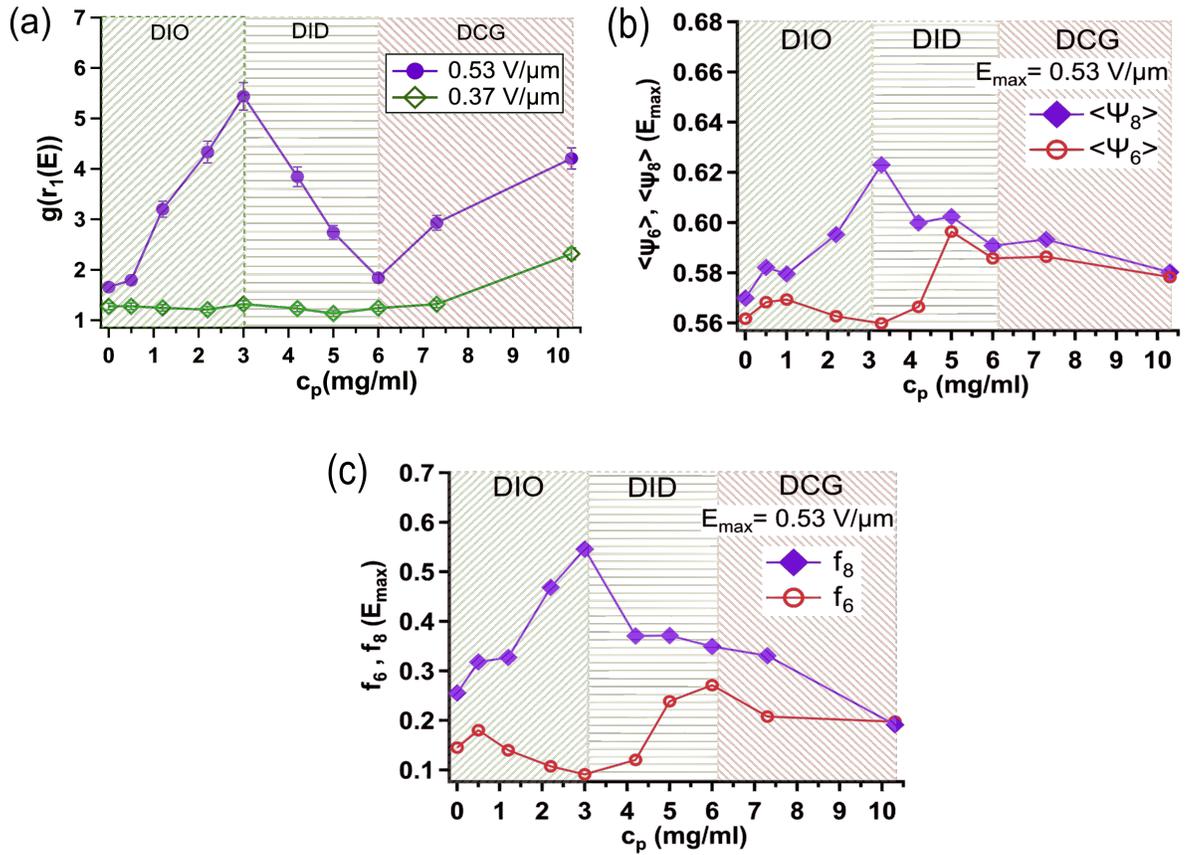
Figure 3.7: Three different regimes in the dipolar-depletion phase diagram at $E_{max} \approx 0.53$ V/μm, quantified by displaying a) $g(r_1)$, b) $\langle \psi_8 \rangle$, $\langle \psi_6 \rangle$ and c) f_8, f_6 as a function of c_p. Three different regimes are marked by different colors in the graph, DIO : depletion induced ordering (green), DID : depletion induced disordering(yellow), DCG: dipolar chain gels (red).

The fluid phase undergoes arrest to a gel phase as c_p is increased to 10.3 mg/ml at $E = 0$ V/μm (Fig. 3.6(c, left)). The gel undergoes structural rearrangement and clusters diffuse to form large aggregates in the xy plane and dipolar chains in the z direction at $E = 0.53$ V/μm as shown in Fig. 3.6(c, right).
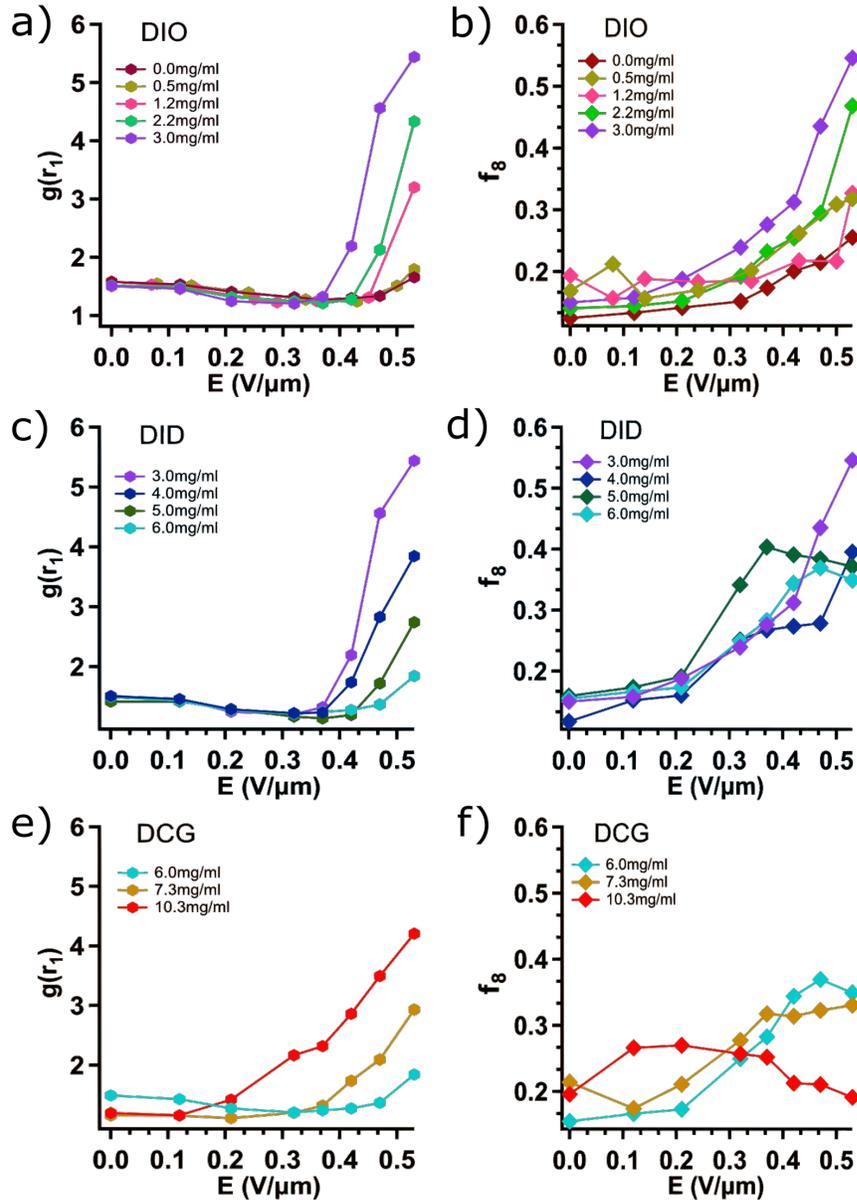
Figure 3.8: The height of the first peak of radial distribution function, $g(r_1)$ and fraction of particles with high $\bar{\psi}_8$ (f_8) varies with the field strength. **a), b)** At $E_{\max} = 0.53$ V/μm, where phase transition happens, $g(r_1)$ increases from $c_p = 0$ mg/ml to 3 mg/ml due to increase in the ordering of the structure and local orientational order, f_8, increases as well. **c), d)** Both $g(r_1)$ and f_8 decreases in the second regime (DID). **e), f)** $g(r_1)$ again increases in the third regime (DCG) from $c_p = 6$ mg/ml to 10.3 mg/ml whereas f_8 further decreases in this regime due to the formation of large disordered structures.

3.4.2 Quantitative analysis of the ordering, disordering and gel regimes

Fig. 3.7 helps quantify the above observations using the 2D $g(r)$ peak amplitude at $r = r_1$ (corresponding to the nearest-neighbor maximum) at $E = 0.37$ V/μm (intermediate field strength) and $E_{\max} = 0.53$ V/μm (high field strength) respectively. Different regimes are shown by green, yellow and red shading in the graph, which correspond to the green, yellow and red arrows in the phase diagram (Fig. 3.6).

In Fig. 3.7(a), we compute the 2D $g(r)$ by analysing a sequence of 100 images with a field of view of 256×256 pixels at different field strengths (Fig. 3.7(a)). We see at high field ($E = 0.53$ V/μm) that $g(r_1)$ (the height of the $g(r)$ peak at $r = r_1$) increases in amplitude with increasing c_p for $c_p < 3$ mg/ml. No such increase is seen at lower field ($E = 0.37$ V/μm). We also report the global order parameters ($\langle \psi_8 \rangle$ and $\langle \psi_6 \rangle$) in Fig. 3.7(b) and the fraction of particles with high $\bar{\psi}_8$ and $\bar{\psi}_6$ denoted as f_8 and f_6 respectively in Fig. 3.7(c). For $c_p < 3$ mg/ml, $\langle \psi_8 \rangle$ increases while $\langle \psi_6 \rangle$ decreases. This implies that the dipolar ordering is enhanced, in this regime, by increasing depletion strength. We call this the depletion-induced ordering (or DIO) regime.

Between $c_p = 3$ mg/ml and 6 mg/ml, the opposite trend is seen. $g(r_1)$ decreases for large E with increasing c_p (yellow shaded regime in Fig. 3.7(a)) and so does $\langle \psi_8 \rangle$ (blue shaded regime in Fig. 3.7(b)). In this regime, increasing depletion strength *weakens* dipolar order. We call this the depletion-induced disordering (DID) regime.

For $c_p > 6$ mg/ml at $E = 0.37$ V/μm and at higher fields, an increase in $g(r_1)$ is coupled with a continued decrease in $\langle \psi_8 \rangle$ to a value of 0.58 comparable to the value of $\langle \psi_6 \rangle$. This signifies the formation of disordered clusters. Note that these clusters

at high field are clusters in the xy plane of dipolar chains (along z). We call this the dipolar chain gel (DCG) regime.

In Fig. 3.7(c), we notice that f_8 and f_6 follows the same trend as seen for $\langle \psi_8 \rangle$ and $\langle \psi_6 \rangle$ shown in Fig. 3.7(b). The fraction of particles in each image that shows high $\bar{\psi}_8$, denoted as f_8 is a clear indicator of square symmetry, which in our experiments denotes bct order. Sheets (along z axis), which show up as linear structures in these 2D images have low $\bar{\psi}_8$ beacuse the crystallites are small. Therefore, f_8 is in fact a robust order parameter, which we use in all that follows.

In Fig. 3.8, we plot $g(r_1)$ and f_8 as a function of E, for the different sets of c_{p} that correspond to the different ordering regimes, DIO, DID and DCG. By examining the E dependence of these structural quantities, we hope to better understand the non-monotonic behaviour of $g(r_1)$ with c_{p} at 0.53 V/μm shown in Fig. 3.7(a).

At lower fields, for $E < 0.37$ V/μm, there is a decrease in $g(r_1)$ with E (Figs. 3.8(a) and (c)), and an increase of f_8 with E (Figs. 3.8(b) and (d)), in both the DIO and DID regimes. Even at these weaker fields, there is still a tendency to form chains along the z-axis, chains that feel a dipolar repulsion except at very close distances. Thus, in this low-field regime, increasing E increases chain-chain repulsions. This spreads out the first peak in the 2D $g(r)$ and pushes it out to larger r, and so effectively increases the packing fraction. In weakly repulsive colloidal systems, one can recover hard-sphere-like behavior simply by using an effective hard-sphere diameter, i.e., $R_{eff} = \kappa^{-1} + R$. Thus, one can rationalize the increase in chain-chain repulsions as increasing the effective packing fraction. This in turn is consistent with an increase in f_8.

At higher fields, $E > 0.37$ V/μm, where formation of sheets and dipolar (bct) structure is observed, as shown in Fig. 3.6, $g(r_1)$ behaves differently for the c_p ranges corresponding to DIO and DID. For DIO ($0 \leq c_p \leq 3.0$ mg/ml), in Fig. 3.8(a),

$g(r_1)$ rise more steeply with E as c_p increases: depletion enhances ordered crystal-like dipolar structures. This trend is also reflected somewhat less precisely in $\langle \psi_8 \rangle$, as shown in Fig. 3.8(b). In contrast, for DID ($3 \leq c_p \leq 6.0$ mg/ml), the trend is reversed; $g(r_1)$ rise more steeply with E as c_p *decreases*. For DID, depletion reduces dipolar ordering.

How do we rationalize the non-monotonic concentration dependence of $g(r_1)$ seen in Fig. 3.7(b) and above $E = 0.4$ V/μm in Fig. 3.8(a) and (c)? First, the universal decrease in $g(r_1)$ at low fields in the DIO and DID regimes arises from in-plane dipolar repulsion between colloids. As the field approaches 0.4 V/μm, system-spanning chains form along the field direction. Above 0.4 V/μm, we can rationalize the observations as a competition between dipolar chain-chain repulsions and depletion-induced attractions. The chain-chain interaction is repulsive if the particle positions in the chains are stacked along z, while the interaction is attractive if they are half a particle diameter staggered: see Figures 1 to 3 in Almudallal *et al* [32] for a pictorial discussion. There is thus an energetic barrier, i.e., stacked chains must stagger, in order to form sheets or a bct crystal. In this picture, in the DIO regime, increasing polymer concentration increases the strength of attractions, lowering the chain-chain repulsive barrier to forming sheets and bct crystals, while in the DID regime, the isotropic attractions are strong enough to create disordered stacked chain-chain clusters that compete with bct ordering. Additionally, while dipolar interactions strongly favor linear chains along z, isotropic attraction strongly favors compact clusters, the formation of which would disrupt the dipolar chains.

The above rationalization of the non-monotonic c_p dependence of dipolar structuring assumes that attraction increases monotonically with c_p. Previously reported

non-monotonicity in the depletion interaction itself [44, 45], while an intriguing possibility, is expected to arise only at concentrations much larger than the overlap concentration.

For polymer concentrations corresponding to the DCG regime, $c_p = 7.3$ mg/ml and 10.3 mg/ml, in Fig. 3.8(e) we see that $g(r_1)$ once again rises more steeply with E as c_p increases. However, the morphology of the system is quite different. Even in the absence of a field at $E = 0$, depletion-induced clusters coexist with free particles. When we apply an electric field, disordered large-scale clusters (composed of electrode-spanning columns along z) with much bigger voids are formed. While dipolar structures dominate in the DIO regime and dipolar and depletion structures compete in the DID regime, the DCG regime is depletion-dominated. Thus, at the highest concentration $c_p = 10.3$ mg/ml, significant ordering, as measured by f_8, is not achieved in Fig. 3.8(f), even at $E = 0.53$ V/μm.

3.5 Conclusion and future work

In conclusion, we have experimentally uncovered a new phase diagram by applying switchable dipolar interactions to depletion colloids. The competition between dipolar and depletion interactions gives rise to a rich phase behaviour that includes ordered (DIO) and disordered (DID and DCG) regimes. In the dilute regime of polymer concentration, depletion enhances ordering in the colloidal structures whereas in the semi-dilute regime, disordered structures are observed at higher field strengths. At c_p = 7.3 mg/ml and 10.3 mg/ml, we observe clusters diffuse and form large aggregates in the xy plane, and dipolar chains along z as field strength increases.

The refractive-index and density matched properties of the fluorescently labeled

PMMA-in-CHB and cis-trans decalin allowed us to estimate the relevant parameters from two-dimensional stack of images obtained via confocal microscopy. In particular, we analyzed the 2D radial distribution functions and local bond order parameters of the colloidal structures in the phase diagram. In this way, we found the positional correlation and orientational order as a function of field strength and quantified different regimes in the phase diagram as DIO, DID, DCG.

This work can be extended to simulation studies where colloids can be modeled as a hard sphere and the polymer as freely jointed chains. The effect of polymer flexibility or chain configuration around a sphere can be taken into account when the polymer is modeled as a free chain. Doing simulations in such a system by using the same parameters as discussed in this thesis, one can find out if a non-monotonic behavior is observed as reported by other researchers [45, 46]. Further, phase behavior can be explored by combining dipolar and depletion interactions where polymer chain configuration is considered. According to AO theory, the polymer is assumed to be a hard sphere of size smaller than the size of colloids. Therefore, considering depletant conformations would extend our understanding of dipolar-depletion beyond AO theory.

We can also use switchable dipolar interactions as a tool to examine the kinetics and probe reversibility in different regimes of the phase diagram that we discuss in Chapter 4.

Chapter 4

Dipolar-depletion: time-dependent phenomena

4.1 Introduction

The kinetics of phase transitions has been a subject of study for quite some time. They have been studied experimentally via microscopy and scattering techniques. Colloidal suspensions have been used to study the kinetics of crystal nucleation from the fluid [90], crystal-crystal transitions [35, 91, 39] and dynamics in glassy systems [92]. Presently, the underlying kinetic mechanism of such transitions is poorly understood because of the challenges of controlling the parameter that governs the phase transition. One way of controlling the interactions between colloidal particles is adding non-adsorbing polymer to the suspension. Adding a polymer induces an attraction between the colloidal particles on a scale much shorter than their diameter [41, 48]. This short-range attraction results in non-equilibrium states not seen in molecular systems, such as so-called attractive glasses and gels arising from arrested phase separation [93, 94, 95, 96, 97, 12, 98].

In the previous chapter, we discussed the structural changes in the phase diagram on combining field-induced dipolar and attractive depletion interactions to hard sphere colloids. We have shown that the local structure of the system is a strong function of both c_p and E in the fluid state. In a hard-sphere colloidal suspension, dynamical studies have characterized the formation of glass due to caging where dynamics is slower than its liquid precursor [12]. Similarly, understanding the effect of manipulating control parameters on dynamics could be a key to understanding gelation. To this end, Dibble et $al.$ [18] have correlated structure to dynamics in the gel regime where the probability distribution of displacements shows non-Gaussian behavior as c_p increases. They have described a dynamic transition predicting a strong localization due to strong short-range depletion interactions in a colloid-polymer mixture.

In this chapter, we focus on two kinds of time-dependent phenomena: the transient kinetics during phase change from ordered or disordered structures to a steady state, on one hand, and steady-state colloidal particle dynamics, on the other. First, we report on reversibility in both ordered and disordered regimes of the phase diagram by turning off the electric field after structures have formed in its presence. We determine the structural relaxation time, τ, associated with the 2D structures coming apart upon turning off the external electric field as a function of c_p. Using the dependence of τ on c_p, we establish a dynamical method to determine the attractive potential strength $(U_0/K_B T)$ from a known c_p. We also investigate whether cycling through the field can accelerate aging in the gel state.

We also study the change in colloidal particle dynamics in the dipolar-depletion phase diagram by determining the mean squared displacement (MSD) and probability distribution of displacements $(P(x))$ as a function of both c_p and E.

4.2 Data analysis

4.2.1 Mean square displacement

The mean square displacement (MSD) describes the magnitude of the particle's motion over a specific time interval. The MSD grows linearly with time (t) as,

$$\langle r^2 \rangle = 2dD_0t, \tag{4.1}$$

where r is the displacement, d is the dimensionality of the system, and D_0 is the Stokes-Einstein diffusion coefficient of the colloidal particles [4]. D_0, for colloidal particles of radius R_c in a solvent of viscosity η at temperature T, is given by

$$D_0 = \frac{k_B T}{6\pi\eta R_c}, \tag{4.2}$$

where k_B is the Boltzmann constant. In a plot of MSD as a function of t in 2-dimensions, if MSD $\propto t$ then the slope of the line is equal to $4D_0$ and the system is said to be diffusive.

The mean-squared displacement can also take on a more general scaling form, MSD $= 2dD_\alpha t^\alpha$ where D_α is the generalized diffusion constant $[D_\alpha] = m^2 s^{-\alpha}$, and α is the scaling index [99]. The colloidal particles are in Brownian motion if $\alpha = 1$, which is the normal diffusion of Eq. 4.1. If $\alpha \neq 1$, there is a deviation from the linear time dependence of the MSD and it is called as anomalous diffusion. There are different domains of anomalous diffusion: sub-diffusive, when $\alpha < 1$, and super-diffusive, when $\alpha > 1$.

In this chapter, we analyse MSD in different regimes of the phase diagram as a function of field strength (E). We determine the time-averaged MSD from the analysis of time series movies obtained from the confocal microscope as shown in Fig. 3.6 (Chapter 3). We plot $\log(\text{MSD})$ vs $\log(t)$ to determine the type of diffusion occuring in a given system.

One can also understand diffusive motion from probability theory by applying the Central Limit Theorem to the random walk problem. The Central Limit Theorem implies that the probability distribution $P(r, t)$ for a particle, initially at the origin, undergoing a random walk to be at position r is a Gaussian at time t, given by,

$$P(r, t) = (4\pi Dt)^{-d/2} \exp\left(\frac{-r^2}{2dDt}\right) \tag{4.3}$$

This Gaussian probability distribution function (PDF) shows that the mean square displacement is equal to the variance of the PDF and increases linearly with t [100],

$$\int r^2 P(r, t)\mathrm{d}r = 2dDt. \tag{4.4}$$

4.3 Experimental details

In this chapter we use the same sample used for the phase diagrams in Chapter 3 to study the kinetics during phase change (Section 4.4.1) and steady-state colloidal dynamics (Section 4.4.2).

To study accelerated aging at high c_p, we use fluorescently labeled PMMA spheres of size $\sigma_\mathrm{c} = 1.3~\mu$m and polymer as a depletant with $R_g = (43 \pm 1)$ nm. As described before, we prepare colloidal suspensions with $\phi_\mathrm{c} = 0.10$ by adding the stock solution

of the polymer at $c_p = 7.0$ mg/ml to the dry colloidal particles and then vortex the mixture for 5-10 min. Before experiments, the particle suspension is allowed to equilibrate for at least 3-4 days. The suspensions is then transferred to an electric-field cell as shown in Fig. 2.2 (Chapter 2) with cell thickness $\approx 180\mu$m. Samples are visualized using a Nikon C1 confocal microscope using a 60x magnification oil immersion objective lens with numerical aperture NA = 1.4 and an excitation wavelength of 488nm. Images are recorded at a scanning speed of approximately 1.49 frames per second where 2D xy cross-sectional images have a field of view 256×256 pixels (1 pixel is 0.276^2 μm^2).

The electric field in the experiment is generated using a function generator (Tektronix AFG 3022) and a wide band amplifier (Krohn-Hite7602M).

4.4   Results and Discussion

4.4.1   Kinetics during phase transition from ordered/disordered structures to a steady state

Reversibility in different regimes

We have examined reversibility in the colloidal structures observed in the dipolar-depletion phase diagram in Chapter 3 (Fig. 3.6(a)). All the experiments described have been carried out by increasing the field amplitude from 0 to 0.53 V/μm in 7 steps (as shown in Fig. 3.6). In this section, we do the same, but examine the zero-field structures both in the absence of history, and at the end of one cycle, i.e., with the field turned off. Fig. 4.1(a,b,c), at $c_p = 3$ mg/ml, 6 mg/ml and 10.3 mg/ml, respectively,

shows radial distribution functions $g(r)$ (black and red curves at left). The black curve corresponds to the middle images in Fig. 4.1(a,b,c), which is taken from the left-most column of Fig. 3.6(a) with no history of applied field in the sample. The maximum field in the phase diagram experiments was 0.53 V/μm, images of which are shown in the right-most column of Fig. 3.6(a). The red curve corresponds to the right image in Fig. 4.1(a,b,c), which is obtained 300 s after turning off the field from 0.53 V/μm to 0 V/μm.

At $c_p = 3$ mg/ml (Fig. 4.1(a)), the black and red curves are similar, with coinciding peaks at $r \approx 1.6$ μm or $1.2\sigma_c$, which means the original structure is observed again at the end of cycle 1, implying no history or memory in the sample after turning off the field. At $c_p = 6$ mg/ml (Fig. 4.1(b)), the no-history peak is still at 1.6 μm ($1.2\sigma_c$), but the red (cycle 1) peak becomes smaller and shifts to $r \approx 2$ μm ($1.5\sigma_c$), with a tiny peak at $r \approx 1$ μm for cycle 1 which is due to string-like structures observed during cycle 1 as shown in the 2D image on the right. The fact that the cluster peak occurs at $r < \sigma_c$ is an artifact due to the 2D g(r) analysis of a 3D cluster. There is thus a small remnant effect of the field applied during cycle 1. At $c_p = 10.3$ mg/ml with no history (Fig. 4.1(c), black curve), there is once again a peak at $r \approx 2$ μm and a small peak in $g(r)$ at $r \approx 1$ μm. After cycle 1, the $g(r)$ peak at $r \approx 2$ μm becomes more extended, owing to particle aggregation, and the string-like clusters are readily apparent (increasing the $g(r)$ peak at $r \approx 1\mu$m). Hence, history or memory effects due to field cycling are significantly enhanced at higher polymer concentrations.

In order to quantitatively understand the reversibility in a colloidal structure when the applied field is turned off, we determine $g(r_1)$ as a function of time at r_1, i.e., the position of first peak, for all the polymer concentrations (Fig. 4.2(a)). $g(r_1)$ exponentially decays with time, yielding a characteristic time τ for the colloidal
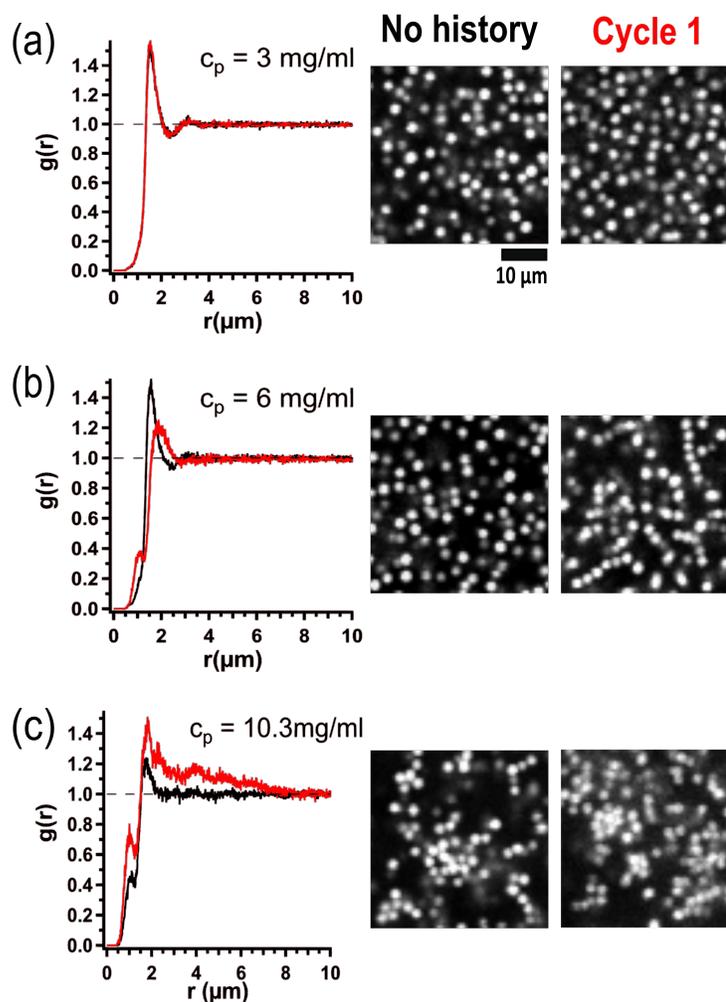
Figure 4.1: Reversibility in the dipolar-depletion phase diagram. Comparison of the radial distribution function, $g(r)$, and representative snapshots, with no history and after one cycle of turning the field on and off at **(a)** $c_p = 3$ mg/ml, **(b)** 6 mg/ml and **(c)** 10.3 mg/ml respectively. The black $g(r)$ curve denotes no history of electric field in the sample, i.e., before the field is applied, while the red $g(r)$ curve is cycle 1 (field OFF). 2D images (64 pixels $\times$ 64 pixels) corresponding to the graphs are captured before turning ON the field (no history) and after turning OFF the field (Cycle 1)
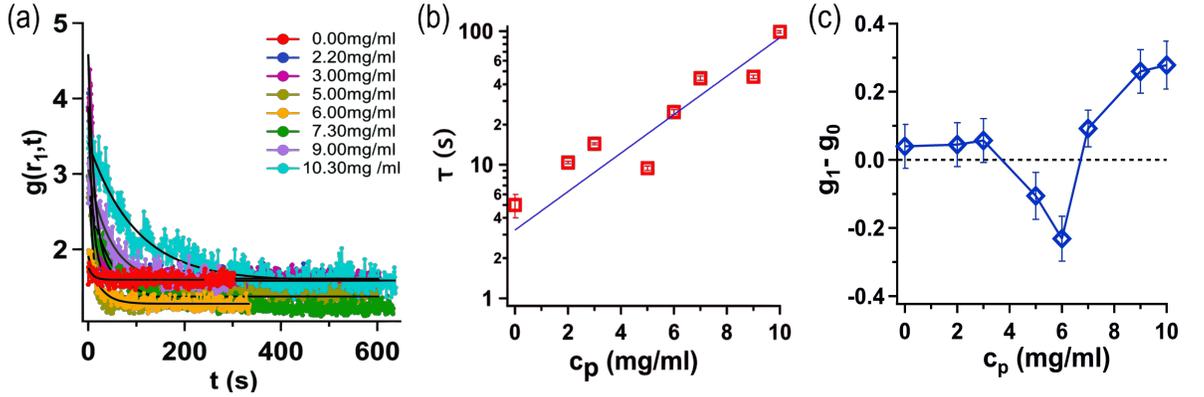
Figure 4.2: **a)** Structural relaxation kinetics $g(r_1, t)$ for all the c_p after field is turned off is well fit to an exponential decay with time constant τ. **b)** The characteristic decay time (τ) taken by colloidal structures to disintegrate and reach a steady state increases exponentially with c_p. **c)** Comparing $g(r)$ (no history) with its value after cycle 1 i.e., $g_1 - g_0$, provides a quantitative measure of reversibility: $g_1 - g_0$ is zero (reversible) in the DIO regime, but non-zero at higher c_p.

structure to come apart and reach a steady-state plateau value $g_1 = g(r_1, t \rightarrow \infty)$. We extract τ and g_1 as functions of c_p from exponential fits like those shown in Fig. 4.2(a). We find that τ increases with c_p (Fig. 4.2(b)), and the increase is well fit to $\tau = \tau_0 \exp\left(\frac{c_p}{c_2}\right)$ with $\tau_0 = (3.2 \pm 1.9)$ s and $c_2 = (3.0 \pm 0.6)$ mg/ml which is close to $c^* = 4.5 \pm 0.1$ mg/ml.

Kilfoil *et al.* and Teece *et al.* used the delay time (τ) of sedimentation profiles at fixed volume fractions and varying c_p [101, 2, 102] to determine the increase in the interparticle interaction energy with c_p. They found that the delay time exponentially increases with c_p i.e., $\tau = \tau_0 \exp(\beta c_p)$, with β depending on ϕ. For our system, $\beta = \frac{1}{c_2}$ where $c_2 = 3.0$ mg/ml ≈ 0.256 wt%. Comparing the expected Arrhenius form $\tau = \tau_0 \exp(U_0/k_B T)$ of any structural relaxation time with our observed exponential dependence of τ on c_p, we obtain the strength of the attractive potential $U_0/k_B T \equiv c_p/c_2$. The Arrhenius expression is assumed to be valid for an increase in thermal

energy having an order of few k_BT. This is tabulated in Table 4.1. For example, for $c_\mathrm{p} = 3$ mg/ml, where the system is in the fluid state at zero field, $U_0/k_BT = 1.0$, while for $c_\mathrm{p} = 10.3$ mg/ml, where we see a transition from a cluster liquid to a gel state, $U_0/k_BT = 3.4$. These estimates of U_0/k_BT are more reasonable than the much larger values (27 and 85 respectively) that are implied by free-volume theory (column 3 in Table 4.1). The reason for unphysically large U_0/k_BT is possibly related to the breakdown of the simple free-volume-theory in the semi-dilute regime of polymer concentration [103]. They are also consistent with previous experiments [63] as well as simulations that report the range of well depths for the onset of aggregation and phase separation [64].

Table 4.1: Polymer concentration (c_p) and corresponding attractive potential strength (U_0/k_BT) estimated from the equation, $U_0/k_BT = c_\mathrm{p}/c_2$ where c_2 is the fitting parameter obtained from the graph in Fig.4(e) and U_{FVT}/k_BT from the Free-Volume Theory (FVT) model [2]

c_p (mg/ml)	U_0/k_BT	U_{FVT}/k_BT
0	0	0
0.5	0.2	4.1
1.2	0.4	10.5
2.2	0.7	19.6
3.0	1.0	26.6
4.0	1.3	35.0
5.0	1.7	43.2
6.0	2.0	51.2
7.3	2.4	61.4
10.3	3.4	84.5

The attractive potential strength has previously been quantified [18, 2] in the context of the free-volume/Asakura-Oosawa theory [41, 48], and phenomenologically, using cluster-size distributions [19]. It is challenging to quantify an interaction potential strength for a system with multiple interactions. Therefore, we use the relaxation time of structures coming apart upon turning off the field to calculate the strength of the depletion attraction strength.

Next, in Fig. 4.2(c), we plot the difference in $g(r_1)$ between the steady state zero-field structure after cycle 1 (g_1) and zero-field structure prior to field application (i.e., no history, g_0). A structure is reversible, showing no history dependence, when $g_1 - g_0$ is 0. At $c_p < 5$ mg/ml, colloidal structures exhibit no history dependence, whereas for $c_p \geq 5$ mg/ml, $g_1 - g_0$ deviates from 0, i.e., we begin observing effects of aging, i.e., dynamically arrested and irreversible structures. At $c_p = 6$ mg/ml (Fig. 4.1(f)), there is a significant negative dip due to the formation of string-like structures as shown in the cycle 1 image in Fig. 4.1(b). It should be noted that the primary $g(r)$ peak contain only part of the information for $c_p > 3$ mg/ml because of the emergence of the cluster peak at $r = 1$ μm. At $c_p > 6$ mg/ml, $g_1 - g_0$ is greater than 0 and increases further at higher c_p as structures remain aggregated during cycle 1 (Fig. 4.1(c)) and shows a strong dependence on the history of the applied field.

Accelerated Aging

Given the above aging effects, it is reasonable to ask if cycling the field can accelerate the natural aging in the gel state. To this end, we use field cycling to probe kinetic pathways at $c_p = 7$ mg/ml where fluid and small clusters coexist at $E = 0$ V/μm. We apply an external field to the sample from $E = 0$ V/μm to 0.42 V/μm, just before the onset of large aggregates (Fig. 3.6(a), 2nd last row), and then turn off the

field (E.F. OFF) to 0 V/μm as shown in Fig. 4.3(a) with the corresponding images in the xy plane for each cycle. First, we record a movie of time length 300 s before turning ON the electric field (E.F. ON) and we call it "no history". Then we switch the field to $E = 0.42$ V/μm, and when we turn it OFF (E.F. OFF) after 15 min, $g(r_1)$ exponentially decays with time and plateaus in a few seconds (Fig. 4.3(a)); this plateau region is labelled cycle 1. We repeat the same procedure on the same sample by again turning ON the field (E.F. ON) to $E = 0.42$ V/μm and turning it off (E.F. OFF) to 0 V/μm to obtain the plateau region that is shown in different colors in Fig. 4.3(a) for each cycle. We record a movie with a 256×256 pixel field of view for four cycles. We observe $g(r_1)$ vary with the number of cycles as shown in (Fig. 4.4(a)). $g(r_1)$ is greater for cycle 4 as clusters persists even after turning off the field, whereas for no history and cycle 1, $g(r_1)$ remains the same. Cycling through the field ages the structures, which take longer to relax to a steady state (increasing τ in Fig. 4.4(b)), and the steady state in turn increasingly deviates from the original state increasing $g_n - g_0$ with increasing cycle number n in Fig. 4.4(c).

In order to check if the particles during cycle 4 (Fig. 4.3(a)) return to their original state with no history, i.e., if the cycling is progressing irreversibly towards a gel state, we kept the sample undisturbed for a few days. On day 7 we captured the image shown in Fig. 4.3(b) where emergence of a big network of clustered particles is observed. Field cycling consequently accelerates particle aggregation, facilitating the formation of large networks of non-equilibrium immobile gel-like clusters in the field-off state.

We also quantify aging in the structure by determining τ from the exponentially decaying $g(r_1)$ with time (Fig. 4.3(a)). In Fig. 4.4(b), the increase in τ with no. of cycles shows stronger attraction strength between particles as it takes longer for the particles in a cluster to come apart. Also, the structural measure of reversibility,
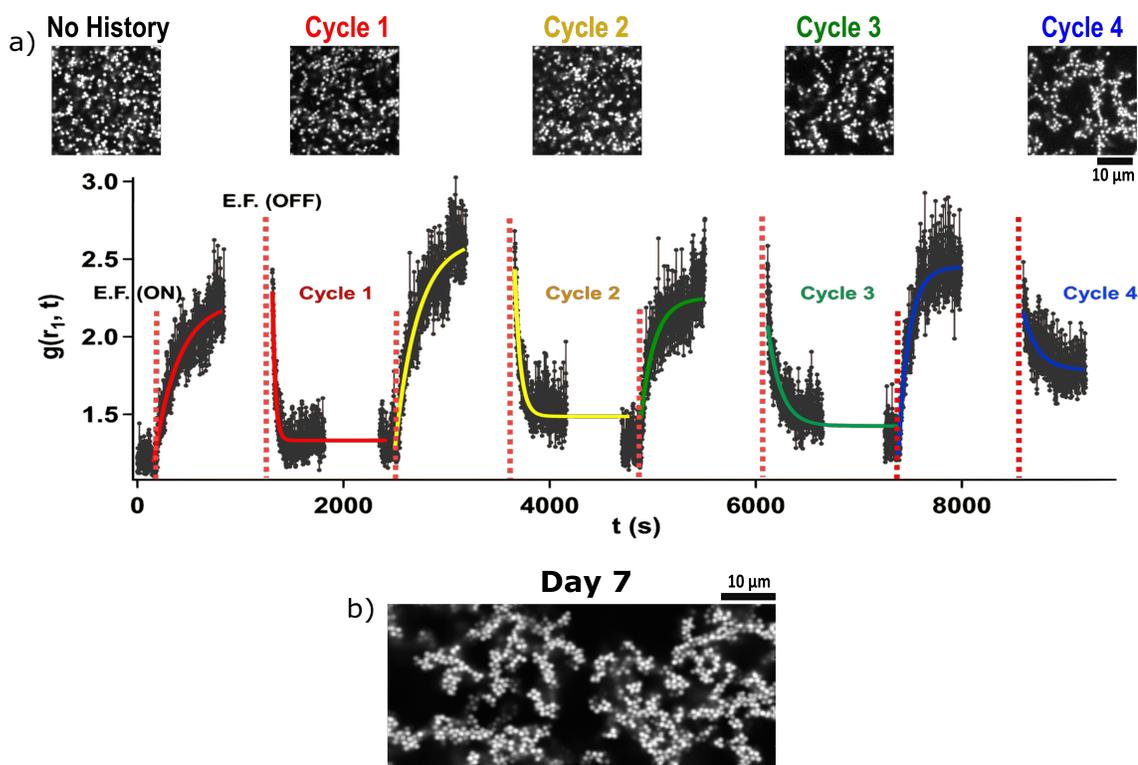
Figure 4.3: Multiple times cycling through the field. **a)** Kinetics at $c_\mathrm{p} = 7$ mg/ml to probe reversibility is labeled by number of cycles with corresponding 2D microscopy images of size 128×128 pixels for no history and different cycles. Four colors indicate different cycles of the experiment. Cycle 1 (red) starts when the applied field is turned off for the first time and is denoted as E.F. (OFF). The experiment is repeated multiple times by turning on (E.F. ON) and off (E.F. OFF) the electric field to obtain $g(r_1)$ as a function of time (t). **b)** 2D image (256×120pixel) of the same sample captured on day 7 and averaged over a time of 13.5 sec showing immobility in the network of clusters.
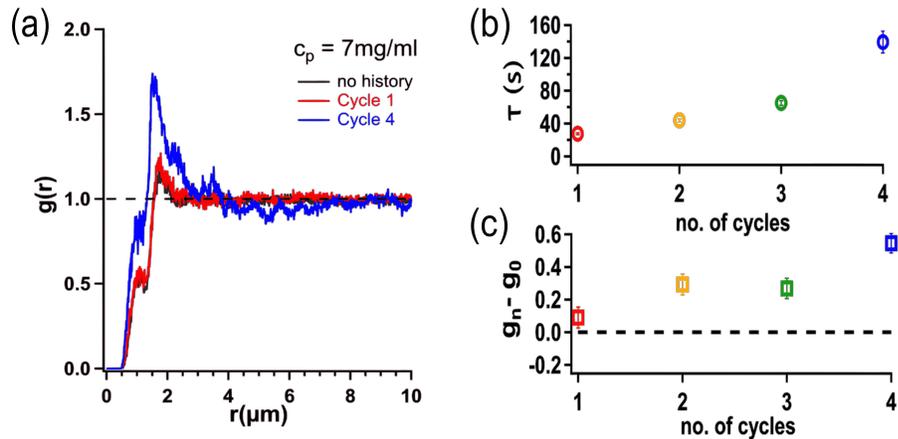
Figure 4.4: Accelerated aging. **a)** The first peak of $g(r)$ for cycle 4 increases as compared to no history and cycle 1, as clusters in cycle 4 persist for a long time after turning off the field. **b)** Decay time (τ) for colloidal structures to come apart in each cycle increases with number of cycles, showing progressive aging in structure during cycle 4. **c)** structures are far away from equilibrium as we increase the number of cycles. During cycle 4, colloidal structure becomes immobile and takes much longer to return to its original state with no history.

$g_1 - g_0$ is shown in Fig. 4.4(c), that is much larger for cycle 4 compared to the first three cycles.

4.4.2 Steady-state colloidal dynamics in an external electric field

The dynamical properties of a system can be quantified using single particle trajectories. A common parameter to quantify the dynamics is the mean squared displacement, MSD. In this section, the MSD in both zero field and at different electric fields, and the probability distribution of displacements, $P(x)$, is discussed.

Sub-diffusive behaviour in an electric field

Anomalous diffusion is most commonly observed in living systems. It can arise when particles interact with the medium in which they move [104] or due to strong correlations in diffusive motion [105]. In a living system, the high density of the cell environment creates many obstacles for the molecule along its path that leads to anomalous diffusion [106, 107]. Therefore, it is likely the result of obstacles to diffusion, i.e, particles are intermittently trapped in multiple locations for a period of time, with traps having a distribution of binding energies or escape times [107].

In a colloidal system, anomalous kinetics is observed near the glass transition. The local motion of the particles give rise to subdiffusive behaviour for a range of time scales [92, 108, 109, 110]. The experimental study by Weeks and Weitz [110] showed that the temporal correlations in the particle motions are due to the cage effect of glassy systems. This particle caging is directly connected to the subdiffusive motion. On the other hand, the long time behaviour of the MSD is diffusive, where cage rearrangements allow particles to move large distances. Furthermore, Zaccarelli and Poon [109] discussed that each diffusing particle carries with it memory of its bonded neighbors and hence leading to a subdiffusive behavior.

In this section, we characterize the dynamics of the system under an external electric field for different c_p. First, we calculate the two-dimensional MSD, $\langle \Delta r^2(t) \rangle$, from particle centroids as a function of time. We then fit the data to a power law, $\langle \Delta r^2(t) \rangle = 4Dt^\alpha$, where α is the exponent. For normal Brownian motion, $\alpha = 1$, while motions that are sub-diffusive result in $\alpha < 1$.

Consider the example of a sample at $c_\mathrm{p} = 3$ mg/ml at different fields (Fig. 4.5). For $E = 0$, MSD $\propto t$, and one can obtain the diffusion coefficient from the slope,
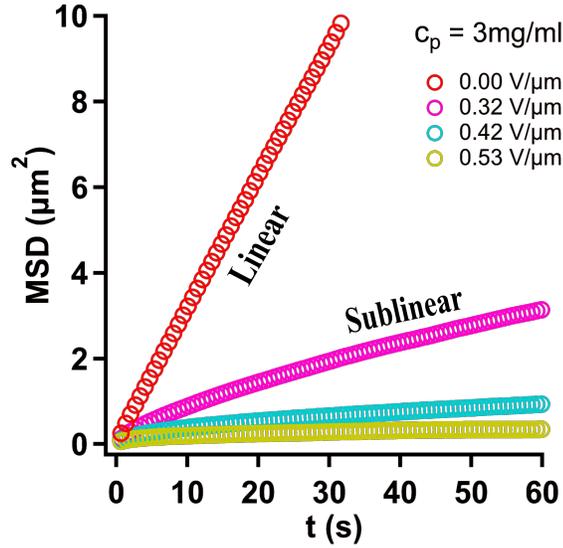
Figure 4.5: Mean square displacements for $c_\mathrm{p} = 3$ mg/ml at $E = 0$ V/μm, 0.32 V/μm, 0.42 V/μm, and 0.53 V/μm.

$D = 0.078 \pm 0.001$ μm^2/s. Very similar behaviour is observed for $E = 0.11$ and 0.21 V/μm. As one increases the field above $E = 0.21$ V/μm, the dependence becomes sub-linear. In Fig. 4.5, we show a linear plot of MSD vs t where at $E = 0$ V/μm diffusion is Brownian and becomes subdiffusive at $E > 0.21$ V/μm for $c_\mathrm{p} = 3$ mg/ml.

Fig. 4.6 shows $\log(\mathrm{MSD})$ as a function of $\log(t)$ for $c_\mathrm{p} = 0$ mg/ml, 3 mg/ml, 5 mg/ml and 7.3 mg/ml (column 1 of Fig. 3.6, Chapter 3) at different field strengths. For $c_\mathrm{p} = 0$ mg/ml and $E = 0$ V/μm (no field) (Fig. 4.6(a)), we observe that $\alpha = 1$, indicating normal diffusion. As the field strength increases, the dynamics become sub-diffusive with $\alpha < 1$. In Fig. 4.6(a), above $E = 0.2$ V/μm, α decreases significantly and is always less than 1. The decrease in α as E increases can also be seen in Fig. 4.7, where we plot α as a function of E.

In our system, we change the particle interaction strength by varying c_p and E while keeping the particle density constant. For $c_\mathrm{p} = 0$ mg/ml (Fig. 4.6(a)), the deviation from normal diffusion, $\alpha < 1$, is observed above $E = 0.2$ V/μm where
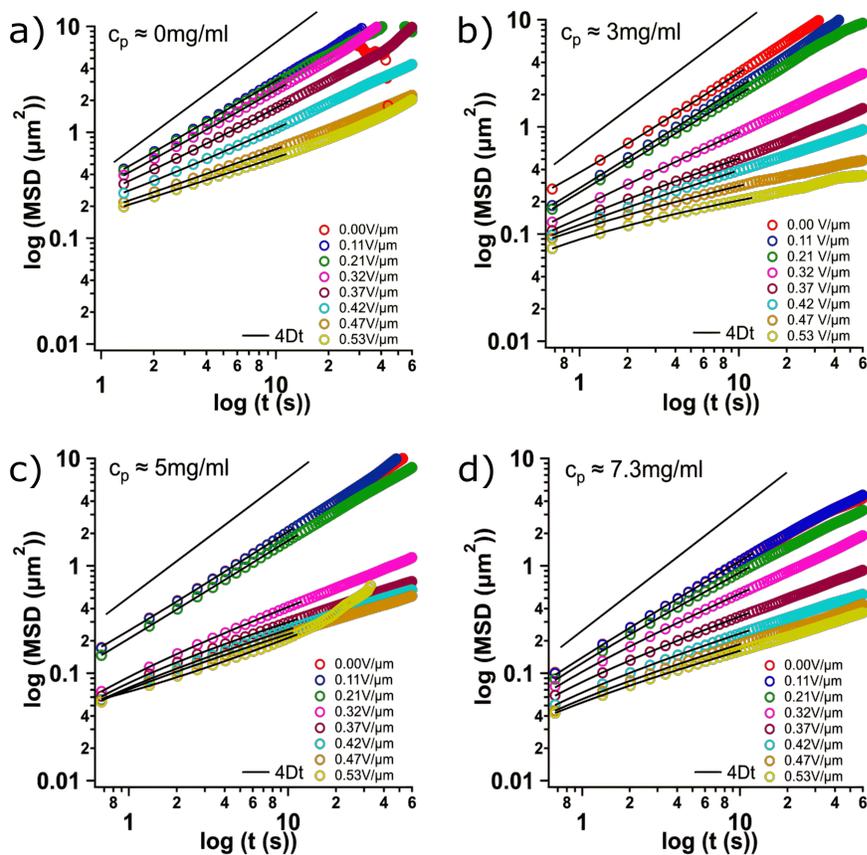
Figure 4.6: Mean square displacements at (a) $c_p = 0$ mg/ml (b) $c_p = 3$ mg/ml (c) $c_p = 5$ mg/ml (d) $c_p = 7.3$ mg/ml. Solid black line at the top of each graph is a reference line of slope $\alpha = 1$.

particles rearrange themselves to form chains in the z-direction. An increase in E increases the particle-particle interaction leading to an increase in the local packing fraction. With an increase in E, growth of dipolar chains along the direction of the field increases and prevents particles in a chain from moving large distances. This restricted motion at high E due to stiffness in chains and increase in local packing fraction of particles leads to subdiffusive motion. Similarly, for $c_p = 3$ mg/ml and 5 mg/ml, sub-diffusive behavior in particle dynamics increases with E (Fig. 4.6(b) and (c)).

The dependence of dynamics and structure of the system on both the particle concentration and the magnitude of an oscillating field is discussed in Ref. [111]. Firstly, the authors observed that an increase in particle concentration leads to subdiffusive behavior. At higher concentrations, particles are trapped in small cages, resulting in slowing down of the dynamics. Secondly, in the presence of a magnetic field, the motion is diffusive at lower fields, and becomes subdiffusive as the field increases. They report that this subdiffusivity is due to the slowing down of the particle dynamics (via a smaller diffusivity) and is expected as the magnetic field induces chain formation in the direction of the field. At high magnetic field, particle positions are correlated with the initial positions, causing subdiffusivity.

In our experiments, the attractive interaction between the particles is further increased by adding more polymer. At $c_p = 7.3$ mg/ml and $E = 0$ V/μm, there is a coexistence of small clusters and individual particles. This increase in depletion strength slows down the particle motion, and clustering induces strong correlations of particles with their initial positions. Therefore, at $c_p = 7.3$ mg/ml when no external field is applied, $\alpha = 0.865 \pm 0.001$, as shown in Fig. 4.6(d) and Fig. 4.7. As E increases, chain formation starts in the z direction, leading to the formation of big aggregates
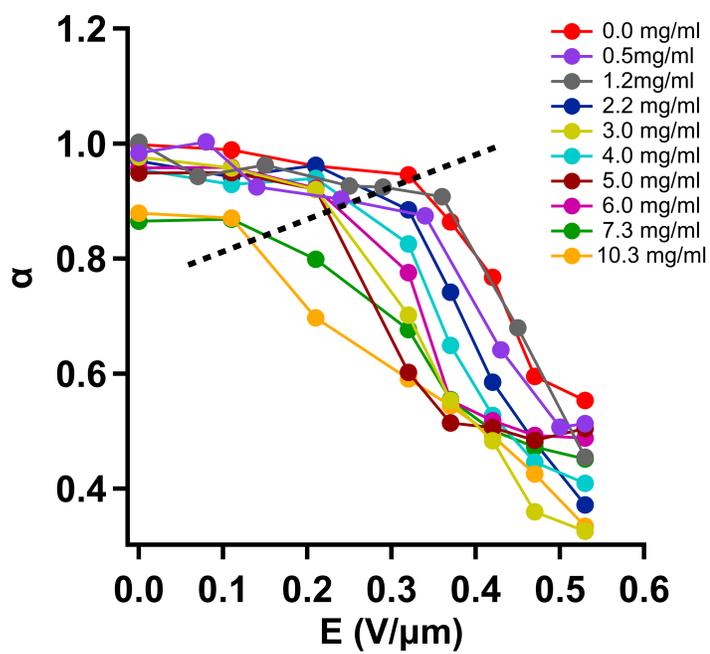
Figure 4.7: The anomalous exponent, α, decreases as the field strength increases. The black dashed line indicates the cross-over regime where the dynamics of the system change and becomes subdiffusive.
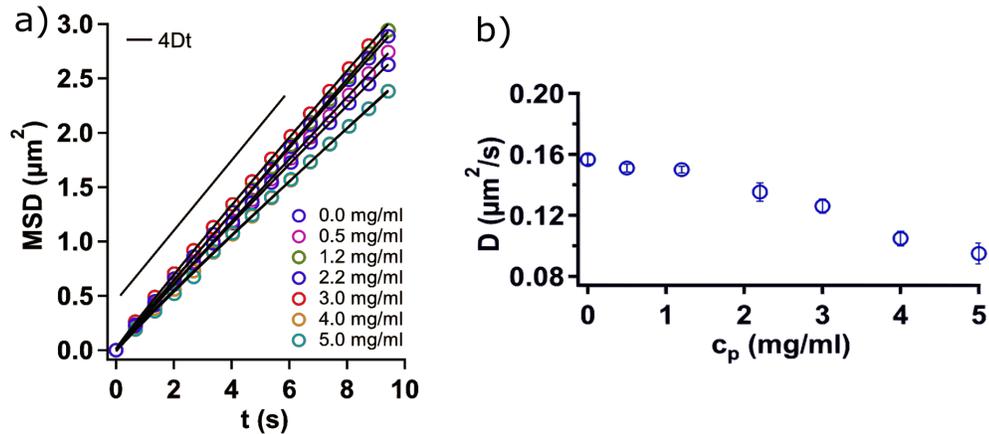
Figure 4.8: MSD at $E = 0$ for c_p from 0 to 5 mg/ml. **a)** MSD increases linearly with t where $\alpha \sim 1$. **b)** Diffusion coefficient D is obtained from the slope of MSD vs t plot where $\alpha \approx 1$.

in the xy plane where particles are trapped and do not move large distances. Thus we observe a further decrease in α. In Fig. 4.7, a dashed line shows the cross-over region beyond which α significantly decreases.

What causes subdiffusive motion, i.e., $\alpha < 1$, as opposed to just slower diffusivity with $\alpha = 1$? Subdiffusion could be due to steric and energetic barriers to particle diffusion with a broad distribution of escape times, here attributable to heterogeneous environments within clusters [104]. Further, each diffusing particle may carry along with it a remnant of its initial geometric cage because of the existence of interparticle attraction [109]. Within the temporal range probed in our experiments, we observe subdiffusivity.

Fig. 4.8(a) shows the linear increase in MSD as t increases for c_p ranging from 0 to 5 mg/ml. In this range of polymer concentrations $\alpha \sim 1$ (Fig. 4.7). At $c_p = 0$ mg/ml, $D \approx 0.160 \pm 0.001$ μm^2/s (Fig. 4.8(b)) and the radius obtained from Stokes-Einstein equation (Eq. 2.5) is close to 1.3 μm.

Probability distribution function

We determine the probability distribution of particle displacements ($P(x)$) in the x direction in the different regimes of the dipolar-depletion phase diagram (Fig. 4.9). $P(x)$ is calculated in the steady state from particle trajectories by averaging over multiple time origins. In Fig 4.9, we show $P(x)$ for $c_\text{p} = 0$ mg/ml, 3 mg/ml, 5 mg/ml, 7.3 mg/ml and 10.3 mg/ml at $t = 10.095$ s and at different field strengths: no field (0 V/μm), intermediate (0.32 V/μm) and high (0.53 V/μm). We measure $P(x)$ only for relatively short times as the statistics get poorer for longer times. We observed for c_p ranging from 0 mg/ml to 7.3 mg/ml that $P(x)$ has a Gaussian form, as shown in Fig. 4.9(a)-(d), consistent with liquid-like structure. In contrast, in Fig. 4.6 (a, b and c), we notice that the MSD as a function of time on a $\log - \log$ plot shows subdiffusive behavior, and furthermore the degree of subdiffusivity increases with E. For example, at $E = 0.21$ V/μm, α decreases from 0.96 to 0.69 with increasing c_p, while at $E = 0.53$ V/μm, α decreases from 0.55 to 0.33 with increasing c_p. Also, for c_p = 7.3 mg/ml (Fig. 4.6 (d)), we observe subdiffusive behaviour even for $E = 0$ which becomes more subdiffusive at high E. For $c_\text{p} = 0$ to 5 mg/ml, the Gaussian behavior indicates that each particle experiences the same homogeneous environment with no signs of non-Brownian motion in a system that is also consistent with MSD vs t for no field as shown in Fig. 4.8(a) [112]. Thus, $P(x)$ does not yet look significantly non-Gaussian at times up to 10 s while the sub-diffusive MSD vs t looks non-Brownian. This behavior seems interesting and warrants further study.

For $c_\text{p} = 10.3$ mg/ml, in Fig. 4.9(e), the distribution is distinctly non-Gaussian (in fact, exponential, with a cusp at zero displacement) where gel-like clusters are observed and becomes more non-Gaussian with increasing E. Therefore, a transition of probability distribution from liquid-like structure to a gel can be seen already
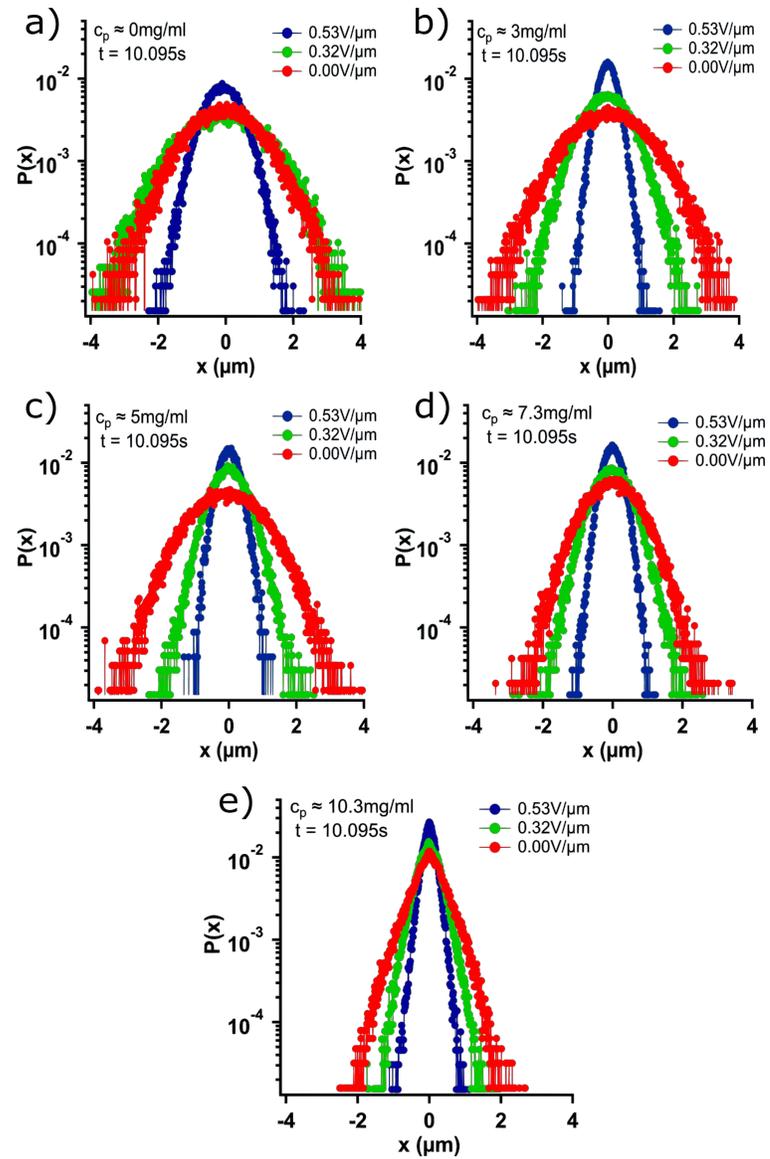
Figure 4.9: Probability distribution of displacements at $t = 10.095$ s and different field strengths: 0 V/μm, 0.32 V/μm (intermediate), 0.53 V/μm (high) for **a)** $c_p = 0$ mg/ml **b)** $c_p = 3$ mg/ml **c)** $c_p = 5$ mg/ml **d)** $c_p = 7.3$ mg/ml **e)** $c_p = 10.3$ mg/ml.

at $t = 10.095$ s in Fig. 4.10(a). $P(x)$ has a Gaussian form if a particle experiences Brownian motion [99]. Therefore, the non-Gaussian dynamics at $c_p = 10.3$ mg/ml is due to the immobilized clusters that is also a characteristic of a gel-like structure. Similar phenomena were reported (in the absence of a field) by Dibble *et al.* [18], who discussed the slow dynamic behavior and strong departures from a Gaussian distribution due to immobile clusters at high depletion strength (or c_p).

To further quantify the accelerated aging observed in Fig. 4.3 and Fig. 4.4, we measure $P(x)$ for $c_p = 7$ mg/ml at $t = 10.095$ s. We calculate $P(x)$ for the case where no external field is applied (no history), and for all the four cycles where $g(r, t)$ plateaus as shown in Fig. 4.3(a). $P(x)$ for no history shows Gaussian behaviour (Fig. 4.10(b)). As we cycle through the field, the interparticle attraction increases: this is reflected in the increase of τ with cycle number shown in Fig. 4.4(b). Additionally, $P(x)$ becomes progressively and significantly more non-Gaussian (Fig. 4.10(b)) with each cycle. This highly non-Gaussian behaviour shows particles become progressively more localized with each cycle. We further examine this surprising behaviour by analysing the 2D mean-squared displacement (MSD). We find that the 2D MSD also becomes increasingly sub-diffusive after each cycle (Fig. 4.10(c)).

4.5 Conclusion and future work

We have provided the first experiments exploring colloidal kinetics using switchable dipolar interactions as a tool to probe reversibility in both ordered and disordered regimes of the phase diagram. We find that the structural relaxation time at $E = 0$ increases exponentially with concentration through all three regimes. Thus, the breaking apart of structures upon turning off the field takes longer as c_p increases.
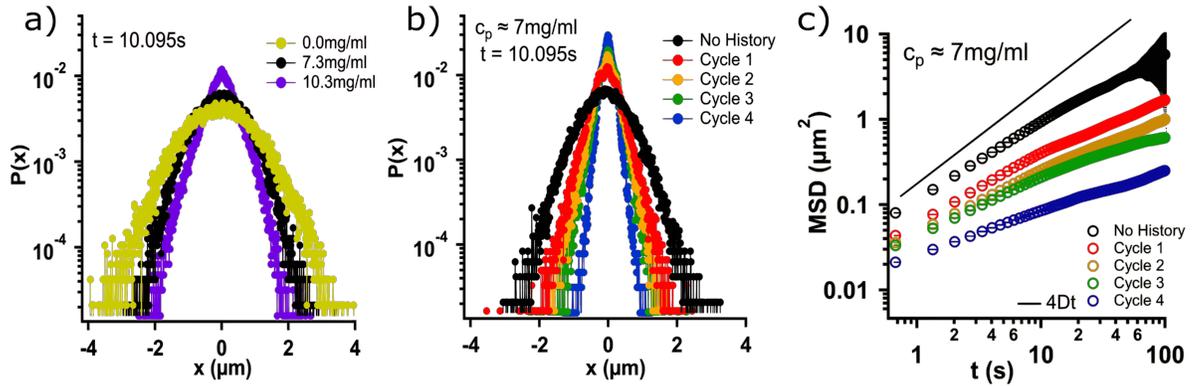
Figure 4.10: From Gaussian to non-Gaussian. **a)** Transition from a Gaussian distribution to non-Gaussian in a gel-regime for $c_p \approx 10.3$ mg/ml at $t = 10.095$ s when no field is applied. **b), c)** show probability distribution of displacement and mean square displacement (MSD) for repeated cycling of the external field that is labeled with cycle no. as shown in Fig. 4.3(a) at $c_p \approx 7$ mg/ml and $t = 10.095$ s.

We use this relaxation time (τ) of structures coming apart to calculate the potential strength that gives more realistic values compared to free-volume theory [11, 50] (as shown in Table 4.1). We determine τ as a function of c_p, finding that τ exponentially increases through all three regimes. A static structural measure of reversibility, $g_1 - g_0$, clearly identifies only the lowest c_p (DIO) regime as exhibiting reversibility. A dynamic measure, the probability distribution of displacements, exhibits a crossover from Gaussian, at low c_p, to non-Gaussian with increasing c_p, and the mean-squared displacements also become progressively more sub-diffusive.

We can accelerate aging by repeated field cycling. This is shown for a sample at $c_p = 7$ mg/ml, that at zero field (no history) is in a cluster liquid state. All quantities probed show consistent behaviours with increasing cycle number n. The structural relaxation time τ increases. A structural measure of reversibility, $g_n - g_0$, deviates further from zero. The distribution of displacements goes from near-Gaussian to

strongly non-Gaussian (exponential with a cusp at zero displacement). The mean-squared displacement becomes increasingly sub-diffusive. A week after the end of field-cycling, the structure is still that of a gel, only somewhat more coarsened.

As an example application of our aging method, in some gels, the time required to see gel collapse can be months or even years, making the study of such collapse untenable. Our accelerated aging may allow such studies.

In our experiments, we determine interaction energy from τ that varies exponentially with c_p at $\phi = 0.1$. As a further study, one can experimentally find how τ varies at different volume fractions as a function of c_p. In an experimental study by Kilfoil *et al.* [101], delay time τ depends exponentially on c_p for a single ϕ, i.e, $\tau = \tau_0 \exp(\beta c_p)$, where β shows the dependence on ϕ. Therefore, in our system such scaling behaviour of τ with ϕ can also be expected. This relation between τ and ϕ as a function of c_p can determine the onset time for instability or irreversibility in a colloid-polymer system.

Furthermore, electrorheology (ER) experiments at high c_p can help to understand the gel formation from the yield stresses at which the behaviour changes from liquid-like to solid-like. Such field-induced interactions can be useful in exploring new materials for electrorheological fluids.

Chapter 5

Study of electrokinetics in a colloidal suspension using microelectrophoresis

5.1 Introduction

In the early 19th century, Reuss was the first to observe electrokinetic phenomena [113]. Reuss carried out two simple experiments with an apparatus consisting of a U-tube with two electrodes [114]. In the first experiment, he put a plug of clay in the U-tube and observed that the water level rose in one part of the tube on application of an electric field. This phenomenon is electro-osmosis. In another experiment, he put quartz sand above the clay plug and observed the field-driven directional flow of suspended clay particles through the sand layer, which is known as electrophoresis [115].

In this chapter, we study the electrophoresis phenomenon for a colloidal suspension in a solvent mixture of CHB and cis-trans decalin that contains the salt, tetrabutyl ammonium bromide (TBAB), used to control the Debye length. In such a system,

colloidal particles can attain surface charges in multiple ways: dissociation of the surface group on the colloidal particle, and adsorption of tetrabutyl ammonium ions from the solution. Therefore, applying an electric field can be useful for manipulating and characterizing the behavior or properties of the system. The electric field affects the interaction between the components in a system in many ways, such as polarization of charges (discussed in Chapter 1). The interactions in a system includes short-range interactions like the excluded volume and van der Waals interactions, and long-range interactions, such as electrostatic and hydrodynamic interactions. These interactions strongly affect the equilibrium and dynamical properties of a system. Studying such a system has applications in the real-world, such as xerography, where the application of an electric field moves charged particles to a charged surface that forms a real image on the electronic template, and related but more recent, electronic paper.

Colloidal particles in a suspension are surrounded by an electric double layer of oppositely charged ions due to the electrostatic interaction. Some ions in a suspension strongly bind to the surface of colloids, which is called the Stern layer, whereas the diffuse layer is characterized by weakly bound, mobile ions. The thickness of the diffuse layer is of the order of Debye screening length, κ^{-1}. When an electric field is applied to the suspension of negatively charged particles, the particles will move towards the positively charged cathode, whereas surrounding ions in the double-layer will move in the opposite direction. This process is known as the electrophoresis. Therefore, the presence of electrical charges at the particle surface and in the solvent cannot be neglected.

In an aqueous solution, the motion of double-layer ions in the opposite direction to that of particle motion exerts a friction force on the particles. The electrophoretic mobility, μ_e, of the particle in such a system is given by the ratio between the terminal

velocity, v and the applied electric field, E.

$$\mu_e = \frac{v}{E}. \tag{5.1}$$

The electrophoretic mobility of a particle depends on the particle size (σ_c), κ^{-1} and the electric potential at the boundary of the double layer, known as the zeta potential. The zeta potential is denoted by the Greek letter ζ. The relation between μ_e, and the ζ-potential is reasonably well captured by the Smoluchowksi and Hückel formulae and the Henry formula (described below).

Smoluchowksi obtained the following relation between μ_e, and ζ–potential for the screening length, $\kappa\sigma_c \gg 1$ (thin double layer):

$$\mu_e = \frac{\epsilon\zeta}{\eta}, \tag{5.2}$$

here $\epsilon = \epsilon_s\epsilon_0$ is the permittivity of the solution and η is the shear viscosity of the fluid. For the opposite extreme condition, i.e. $\kappa\sigma_c \ll 1$ (thick double layer), Hückel derived the following equation,

$$\mu_e = \frac{2\epsilon\zeta}{3\eta}, \tag{5.3}$$

where retardation and polarization forces due to the movement of counterions were neglected. Henry derived an expression for the varying double-layer thickness due to screening of charges by adding salt or intermediate values of $\kappa\sigma_c$ with the electrophoretic mobility taking the form [116],

$$\mu_e = \frac{2\epsilon\zeta}{3\eta} f_1(\kappa\sigma_c) \tag{5.4}$$

where $f_1(\kappa\sigma_c)$ is a scaling function that interpolates between the Smoluchowski and Hückel formulae. One may write a dimensionless $\zeta-$potential, $\Psi = \zeta e/k_B T$ and a dimensionless mobility $M = 3\eta e\mu_e/2\epsilon k_B T$; in these units,

$$\Psi = \frac{E}{f_1(\kappa\sigma_c)}. \tag{5.5}$$

It is possible to determine the particle's surface potential and charge using electrophoresis measurements. The surface potential and charge can be determined from the electrophoretic mobility of a particle. Electrophoretic mobilities can be measured using several techniques like laser Doppler anemometry, optical tweezers, and confocal microscopy. In this chapter, we discuss a refractive index and density matched system, which allows the use of confocal microscopy for measuring mobility at different depths, and hence this method is known as microelectrophoresis. This is an excellent method, because one can establish the entire depth-dependent particle velocity profile, which is composed of both particle electrophoresis and a spatially varying electro-osmotic fluid flow.

Previously, microelectrophoresis studies have been done on the non-aqueous colloidal suspension discussed in this chapter, by Vissers *et al.* [117] and Hayden *et al.* [1]. Vissers *et al.* [117] studied the effect of strong DC electric fields on the electrophoretic mobility in a concentrated suspension at different depths in a capillary. Hayden *et al.* [1] showed the extension to microelectrophoresis through AC measurements in a non-polar solvent. They discussed the frequency-dependent colloid microelectrophoresis using AC fields at a layer close to the top surface of a capillary

and also reported, using impedance spectroscopy, that the electrode polarization effects become significant below a characteristic frequency f_c. In aqueous systems, there have been suggestions that the internal electric field should be suppressed because of the charge accumulation on the electrodes (electrode polarization) [118, 119]. Ma *et al.* [120] have also perfomed AC electrophoresis experiments in aqueous systems at different frequencies using a technique based on optical tweezers. In their paper, they do not account for electrode polarization and show a linear regime where mobilities are independent of frequencies for f between 1 Hz and 100 Hz.

In our experiments, we report mobility values at much lower frequencies i.e., $f <$ 1 Hz where attenuation of the internal electric field is expected to be appreciable (based on impedance spectroscopy carried out by Hayden *et al.* [1]). In non-aqueous colloidal systems there has, to our knowledge, been no prior examination of electrode polarization at all (except [1]). Therefore, there is a reasonable expectation that the DC mobilities could be affected due to electrode polarization. In order to know the effects induced by charge accumulation, we perform AC microelectrophoresis as a function of frequency. In a review article by Zhou and Schmid [121], the advantages of AC electrophoresis over DC electrophoresis are highlighted. In AC electrophoresis, it is possible to tune the frequency and the phase of AC fields, unlike in the DC method, to study the dynamical process on a selective time scale [122]. Also, the AC experiment enables checking for and possibly eliminating electrode polarization effects as well as electro-osmotic flows [121]. Therefore, we need to have a better understanding of the inter-relationship between the methods.

In this chapter we address the questions: does a DC measurement provide realistic values of electrophoretic mobility for charged PMMA colloids in a low-polar solvent mixture of CHB and decalin? What is the frequency dependence of the electrophoretic

mobility? We use both AC and DC microelectrophoresis to measure the charge on a colloidal particle and also to see if the results obtained from both the methods agree with each other. We first calculate electrophoretic mobilities at the stationary layer from the parabolic profile in a closed capillary (discussed in section 5.1.1 and 5.3). We then compare the mobilities obtained from both the AC and DC methods. Finally, we switch the waveform of AC driving from sinusoidal to square-wave - the peak amplitudes should differ by a factor of $\pi/2$ – as a crosscheck of consistency.

Once we know the electrophoretic mobility of particles in both AC and DC fields, it is easy to calculate the zeta-potential of a particle by using the O'Brien and White scheme, which numerically obtains the nonlinear relationship between the dimensionless ζ potential Ψ and the dimensionless mobility M as a function of $\kappa\sigma_c$ (Eq. 5.5) [123]. Thereafter, the ζ potential can further be converted into a particle charge Z, by using the following empirical relation [65, 1]

$$Z = 4\pi\epsilon_s\epsilon_o\frac{k_BT}{e}\kappa a \left[2\sinh\left(\frac{\Psi}{2}\right) + \frac{4}{\kappa a}\tanh\left(\frac{\Psi}{4}\right)\right].\qquad(5.6)$$

Here, ϵ_s is the dielectric constant of the solvent, ϵ_0 is the vacuum permittivity, k_B is the Boltzmann constant, T is the temperature, κ^{-1} is the Debye length, a is the particle radius and $\Psi=\zeta e/k_BT$.

In this chapter, we first discuss the electrophoresis phenomenon in a closed capillary and the method of calculating velocity at the stationary layer in section 5.1.1. Further, in section 5.1.2, we discuss the phenomenon of electrode polarization. The experimental details, including sample and sample cell preparation, are discussed in section 5.2. Section 5.3 reports the results and includes a discussion of all the methods used to obtain the mobilities for the case of DC electrophoresis (section 5.3.1)

and AC electrophoresis with sinusoidal driving (section 5.3.2). In the same section, we also report the charge on a particle. In section 5.4, we present our conclusions.

5.1.1 Electrophoresis
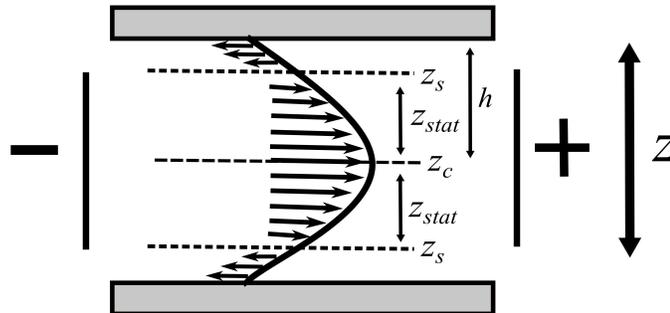
Figure 5.1: The electrophoretic flow in a closed rectangular glass capillary

The application of an electric field to a sample in a closed capillary sets the counterions near the charged wall in motion. These counterions then drag along the fluid (near the wall), resulting in an electro-osmotic flow (EOF) as shown in Fig. 5.1. To counterbalance this flow, a counterpressure builds up, and a parabolic Poiseuille flow (PF) arises in the opposite direction that causes a zero net flow at a stationary layer (z_s) on either side of the midplane of depth z_c (Fig. 5.1). Thus, the velocity of colloidal particles (v_p) at depth z and height h due to the electric field, in a rectangular capillary, is the sum of their true velocity (v_e) and the local liquid velocity ($v_l(z)$) (section 4.1.3 of Ref. [124]),

$$v_p(z) = v_e + v_l(z)$$
$$v_p(z) = v_e + \frac{v_{eo}}{2}\left(\frac{3z^2}{h^2} - 1\right)$$

(5.7)

where v_{eo} is the electro-osmotic velocity and h is the distance from the centre, z_c, of

the rectangular capillary to either of the walls. Therefore, near the wall the particle velocity must be,

$$v_p(\pm h) = v_e + v_{eo} \tag{5.8}$$

and on the axis (centre) of the cell is,

$$v_p(0) = v_e - \frac{v_{eo}}{2} \tag{5.9}$$

At the stationary layer, $z_s = \frac{h}{\sqrt{3}}$, the effects of the flow cancel, giving

$$v_p(z_s) = v_e. \tag{5.10}$$

The above assumes that the rectangular capillary has a very large ratio of width to depth (k). In general, for a rectangular capillary $z_s = z_c \pm z_{stat}$, where z_{stat} is [116]

$$\frac{z_{stat}}{h} = \sqrt{\frac{1}{3} + 4 \left(\frac{2}{\pi} \right)^5 \frac{1}{k}}. \tag{5.11}$$

In our experiment setup, we use a rectangular capillary having a cross-section of 2 mm $\times$ 0.1 mm that has $k = 20 \pm 1$, the ratio between the major and minor cross-section, $h = 50$ μm is the distance from the center of the channel to either of the walls, and z_{stat} is the distance from the center of the channel to one of the stationary layers (Fig. 5.1). z_{stat} for our rectangular glass capillary is 29.75$\pm$0.24 μm, and is measured from the center of the capillary.

5.1.2 Electrode Polarization

An external electric field applied to a sample in a rectangular capillary with electrodes on both ends of the capillary, shown in Fig. 5.2, sets the particles in motion. The cloud of ions surrounding the particles will become distorted, leading to a change in both the local electric field and deformation of the double-layer around the particles. When an oscillatory electric field (AC field) is applied, there will be charges near the electrodes within the partly developed double layer that compensate the charges due to the external electrical field [125]. Hence, electric field will be screened over a distance of the order of the Debye length. Therefore, due to electrode polarization, the electric field in bulk, E_{int} is always smaller than the applied electric field, E. Kang and Dhont [125] have derived an expression for an electric field E_{int}, in terms of E and an attenuation factor γ_{e} accounting for electrode polarization, i.e., $E_{\text{int}} = \gamma_{\text{e}} E$, where

$$\gamma_{\text{e}} = \frac{\Omega}{\sqrt{4 + \Omega^2}}. \tag{5.12}$$

$\Omega = f/f_c$ is a dimensionless frequency, with $f_c = D/(2\pi L \kappa^{-1})$, L is electrode spacing, D is the ion diffusion coefficient and κ^{-1} is the Debye screening length. The experimental work of Hayden $et\ al.$ [1] have estimated the electrophoretic mobility of a particle by taking electrode polarization into account. In our work, $D \sim 0.5 \times 10^{-9} \text{m}^2/\text{s}$, L = 5.4 ± 0.1 mm, and $\kappa^{-1} = (0.095 \pm 0.005) \mu$m, so $f_c \sim 0.15$ Hz. At 0.15 Hz in our system, the attenuation factor would be predicted to be $\gamma_e \sim 0.5$. Indeed, Hayden $et\ al.$ suggested that DC measurements, such as by Vissers $et\ al.$ [117], should be very strongly affected by electrode polarization effects. In the experiments discussed in this chapter, we make a direct test of this and compare the raw, measured AC
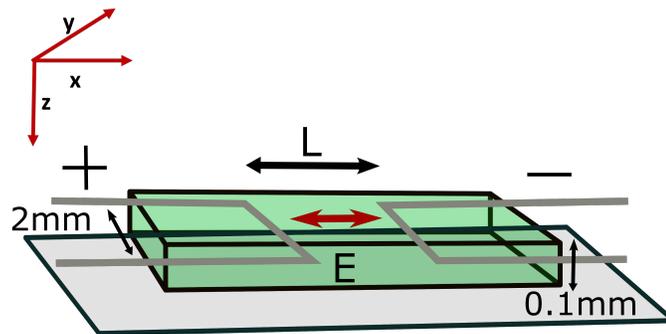
Figure 5.2: Schematic diagram of a rectangular glass capillary with cross-section dimensions 0.1 mm × 2 mm

electrophoretic mobility values with the DC values.

5.2 Experimental Details

Dry PMMA particles are dispersed in a clean solvent mixture of 20 w% of cis-trans decalin in CHB with salt (TBAB) added to it. Particles suspended in a low polar solvent mixture slightly swell over time as particles soak up some of the solvent. Therefore, suspension is allowed to equilibrate for at least two days prior to the experiments. We use fluorescently labeled colloidal particles of diameter 1.3 μm and $\phi = 0.008$ for the electrophoresis measurements. The Debye length of the solvent is 0.095 ± 0.005 μm. The particle suspension is transferred to a rectangular glass capillary (Vitrocom 0.1 × 2.00 mm), shown in Fig. 5.2 and Fig. 5.3, such that no air bubble emerges. Fig. 5.2 is a 3D schematic diagram of a field cell used in the experiments as shown, from a top view, in Fig. 5.3. Fig. 5.3 shows a rectangular glass capillary equipped with two 50 μm diameter nickel alloy wires (Goodfellow) bent twice into 90° angles, at the opposing ends, and the space between the electrodes $L = 5.4 \pm 0.1$ mm. Then, the sample cell is filled with colloidal suspension and
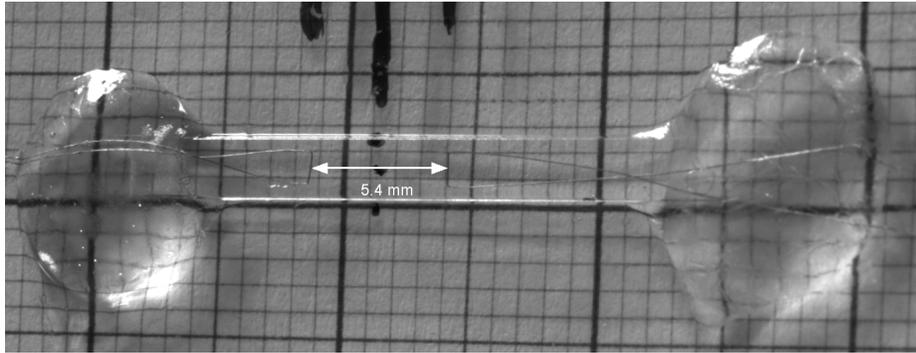
Figure 5.3: A rectangular glass capillary with cross-section dimensions 0.1 mm $\times$ 2 mm filled with colloidal suspension and two nickel alloy wires at the opposing ends with a space between the electrodes $L = 5.4 \pm 0.1$ mm.

electrodes are connected on both ends of the capillary. The capillary is then sealed using UV-glue (Norland optical adhesive, N68) and the UV glue is cured with UV light ($\lambda = 350$ nm, UVGL-58 UV lamp) for 10-15 min. During this process, the sample area is covered with aluminum foil to protect the suspension from UV radiation to avoid the bleaching of particles. All the electrophoretic measurements are done using the Visitech confocal microscope ($\lambda = 488$ nm), using a 60x magnification oil objective lens with numerical aperture NA = 1.4.

A low-frequency electric field is generated using a function generator (Tektronix AFG 3022) and a wideband amplifier (Krohn-Hite, Model 7602M). The sample is mounted on the stage, the distance between the capillary walls (upper and lower wall) in the z-direction is determined using the z-stage on the confocal microscope. For the mobility measurements, time series of images are recorded at different depths along the z-axis of the capillary. We typically probe 9 different positions along the z axis of the capillary. Then using a particle tracking algorithm, the velocity of the particles in the electric field at different depths is determined by extracting the trajectories of particles from a sequence of images obtained using the confocal microscope. Thus,

we obtained a velocity profile that is well fitted to a parabolic function to obtain the velocity and electrophoretic mobility at the stationary layer. Images are recorded with a field of view 480×480 pixels at a scanning speed of 20 frames/second at low frequencies and 100 frames/second at higher frequencies and 1 pixel is 0.108 μm.

5.3   Results and Discussion

In this section, we describe and compare AC and DC electrophoresis methods to calculate μ_e. We use this quantity to calculate the ζ-potential and charge on the colloidal particles.

5.3.1   DC electrophoresis

In the DC electrophoresis experiment, we must change the direction of motion of particles periodically in order to avoid accumulation of particles at one electrode. This change in direction of the field thus has an associated time scale. Therefore, no experiment is truly DC. An electric field in a capillary directs the flow of particles in one direction (along x). In an example DC experiment, we first apply an offset voltage of -20V that leads the particles to flow towards the positive electrode. It shows our colloidal particles are negatively charged. We first wait for 30 s and then, record a movie with 295 frames for 30 s. After recording the movie, we switch the offset voltage to +20V (colloids begin to move in the opposite direction) and again wait for 30 s. Then, we record a 30 s movie in the other direction. Using this timescale, we estimate the frequency based on the time over which the experiment is carried out i.e., 60 s of movie recording and 60 s of waiting time, we calculate a frequency $f \approx$ 0.008 Hz.

To identify the particles and extract their trajectories, some changes were made to the existing tracking algorithm. Due to the driving electric field, a particle moves more than one diameter between successive frames [117]. This can result in incorrect identification. First, a uniform displacement was estimated between the successive frames using Fiji (imaging software). Then, the average displacement is added to a particle's (x, y) coordinate in frame i such that it is close to the (x, y) coordinate of the particle in the next frame $i + 1$. If we add the correct average displacement to each particle in frame i then the mean square displacement to their nearest particle in frame $i + 1$ will be minimal. In this way, we correct for the average drift of the particles.

In the presence of an electric field, the mean-squared displacements (MSD) along the x and y directions are,

$$\langle x^2(t) \rangle = 2Dt + v^2 t^2 \ , \ \ \langle y^2(t) \rangle = 2Dt. \tag{5.13}$$

In this discussion, $x(t)$ is in fact the displacement, i.e., if we denote the positions as x', then $x(t) \equiv x'(t + t_0) - x'(t_0)$ where t_0 is the reference time. It should also be noted that the angle brackets average over reference times t_0. By subtracting the MSD along the non-driven (y) direction from the driven (x) direction, the electrophoretic contribution motion is,

$$X^2{}_{\mathrm{driv}} = \langle x^2(t) \rangle - \langle y^2(t) \rangle = v^2 t^2 \tag{5.14}$$

Using this equation, we obtain the velocity at different depths and plot a velocity profile as a function of z in the sample at a field strength $E = 3.33$ V/mm, Fig. 5.4(a).

The velocity profile is then well fit to a parabolic function $S(z) = Az^2 + Bz + C$, to obtain the electrophoretic velocity v_e near the stationary layer z_s. In Fig. 5.4, the green dashed line denotes z_s and the black dashed line indicates the walls of the rectangular capillary that is located at $h = 50\ \mu m$ and $-50\ \mu m$. Then, the electrophoretic mobility μ_e at z_s is calculated from the ratio of $v_p(z_s)$ and E (Fig. 5.4(b)).
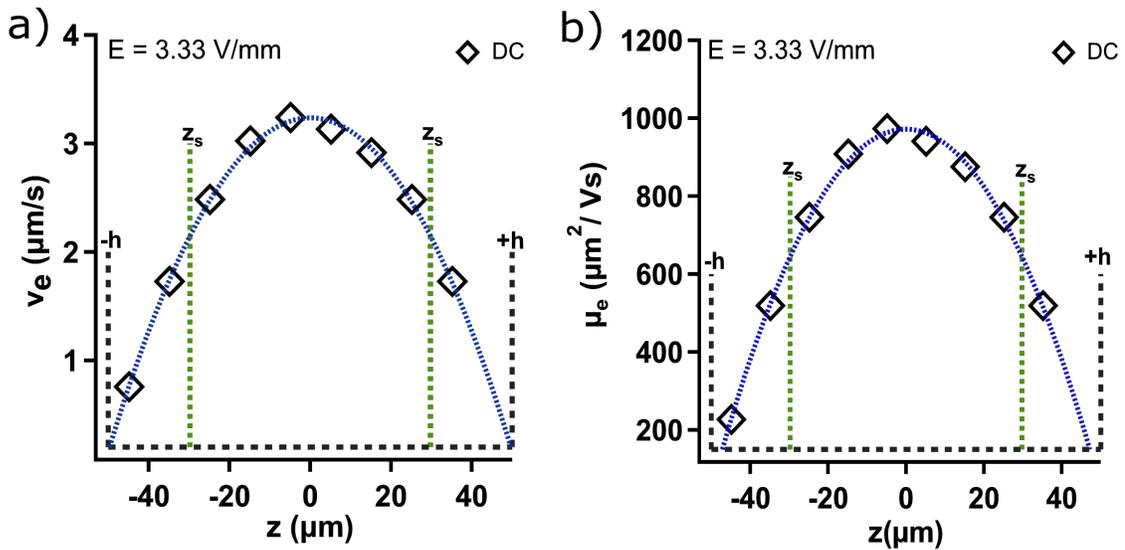
Figure 5.4: DC electrophoresis. **a)** Electrophoretic velocity (v_e) at a field strength $E = 3.33$ V/mm and **b)** Electrophoretic mobility (μ_e) profile as a function of z in a closed capillary of depth $z = 100\ \mu m$ at a frequency $f = 0.008$ Hz. The walls of the rectangular capillary are located at $h = +50\ \mu m$ and $+50\ \mu m$, and the stationary layers z_s indicated by green dashed line. Parabolic fits to the measured profile is drawn as solid blue line.

5.3.2 AC electrophoresis

When an AC field is applied to a colloidal suspension, the particle position varies with time as a periodic sinusoidal wave. The advantage of AC electric fields over DC fields is that the particle motion can be efficiently controlled by adjusting field parameters like magnitude, frequency and wave shape [126, 127]. In addition, the accumulation

of charged species on electrodes can be avoided using AC fields [122].

In AC electrophoresis, above a certain amplitude of voltage, the sine wave output from the amplifier gets distorted. In our experiments for both AC and DC experiments, we use $E = 3.33$ V/mm to avoid this problem.

In the AC method, μ_e is extracted using a sinusoidal AC electric field in a frequency ranging from 0.05 Hz to 5.5 Hz. In the absence of an electric field, particles undergo diffusive motion in both x and y direction, whereas in an external field, there is also a driven motion along the x direction (Fig. 5.5). In the absence of the electric field,

$$\langle x^2(t) \rangle = \langle y^2(t) \rangle = 2Dt, \tag{5.15}$$

where D is the diffusion coefficient of particles. In the presence of an electric field, the mean square displacement along x is described as [1]

$$\langle x^2(t) \rangle = 2Dt + 2A^2 \left(\sin \left(\frac{\omega t}{2} \right) \right)^2, \tag{5.16}$$

where $\omega = 2\pi f$ is the angular frequency of the electrophoretic driving motion and A is the amplitude of the sinusoidal displacement. Similarly, in the y direction,

$$\langle y^2(t) \rangle = 2Dt \tag{5.17}$$

If we assume that there is no coupling between diffusion and driven motion, then the diffusive motion is identical along x and y and the electrophoretic contribution to the motion is given by,

$$x^2_{driv} = \langle x^2(t) \rangle - \langle y^2(t) \rangle$$

$$= 2A^2 \left(\sin \left(\frac{\omega t}{2} \right) \right)^2 \qquad\qquad (5.18)$$

$$= A^2 (1 - \cos(\omega t))$$
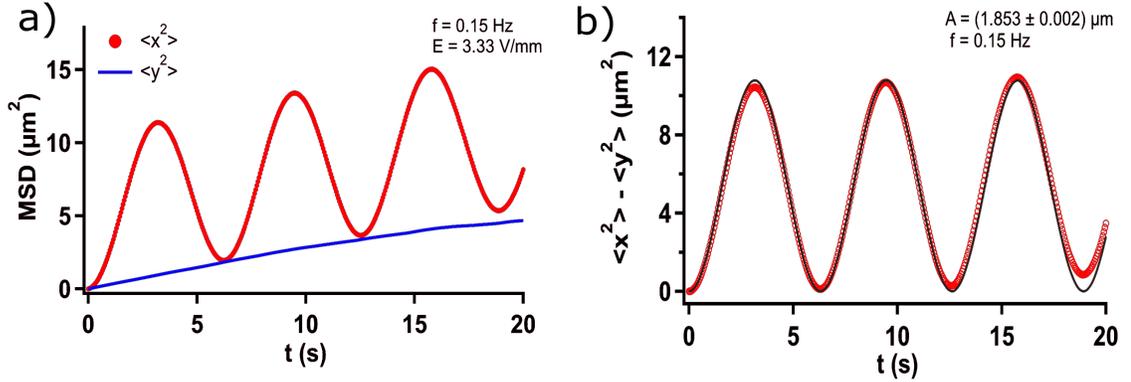
Figure 5.5: Response to a sinusoidal AC electric field at $f = 0.15$ Hz and $E = 3.33$ V/mm. **a)** MSD along x and y direction as a function of time. **b)** The difference in the MSD along the x-direction (driving field) and y-direction. We use Eq. 5.18 to fit the curve and determine the amplitude, A.

We show in Fig. 5.5 that the mean square displacement along x is a sum of a sinusoidal oscillatory term and a linear diffusive term. A plot of $\langle x^2 \rangle - \langle y^2 \rangle$ as a function of t, for $f = 0.15$ Hz and $E = 3.33$ V/mm, in Fig. 5.5(b) shows the time dependence is sinusoidal with the expected frequency. To calculate the velocity, $v_e = 2\pi f A$, we fit the plot in Fig. 5.5(b) using eq. 5.18 to obtain the amplitude, A. Next, v_e is obtained at different z for each frequency. The velocity profile is then fitted using a parabolic function, $S(z) = Az^2 + Bz + C$ to obtain the velocity near the stationary layer z_s. In Fig. 5.6, the green dashed line denotes z_s and the black dashed line indicates the wall of the capillary at $z = h$. Then, the electrophoretic mobility μ_e is calculated the same way as for the DC method, from the ratio of v_e and E (Fig. 5.6(b)). It was independently verified that we were in a regime where
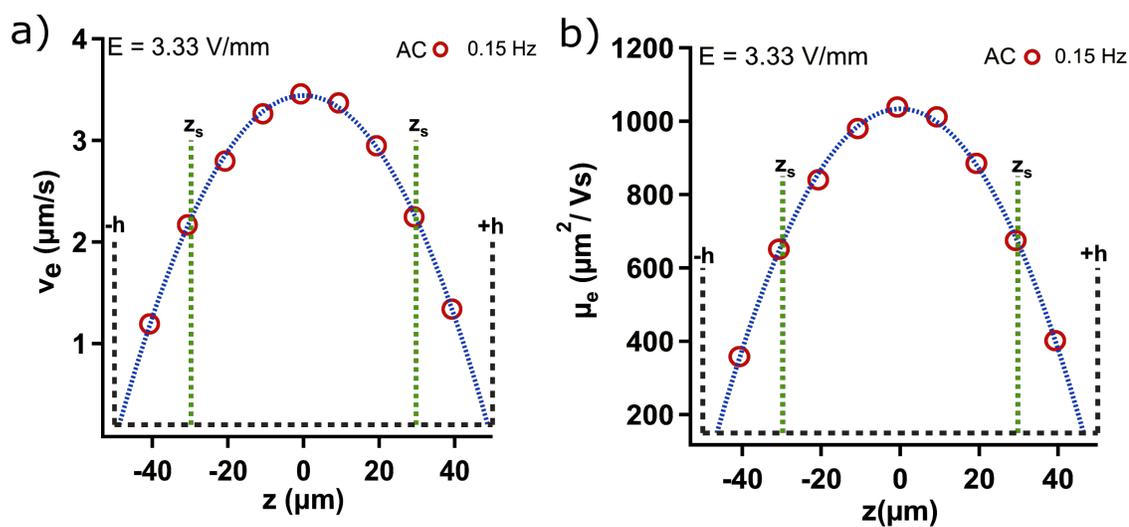
Figure 5.6: AC electrophoresis at frequency $(f) = 0.15$ Hz and $E = 3.33$ V/mm. **a)** v_e and **b)** μ_e profile of PMMA particles suspended in CHB/cis-trans decalin.
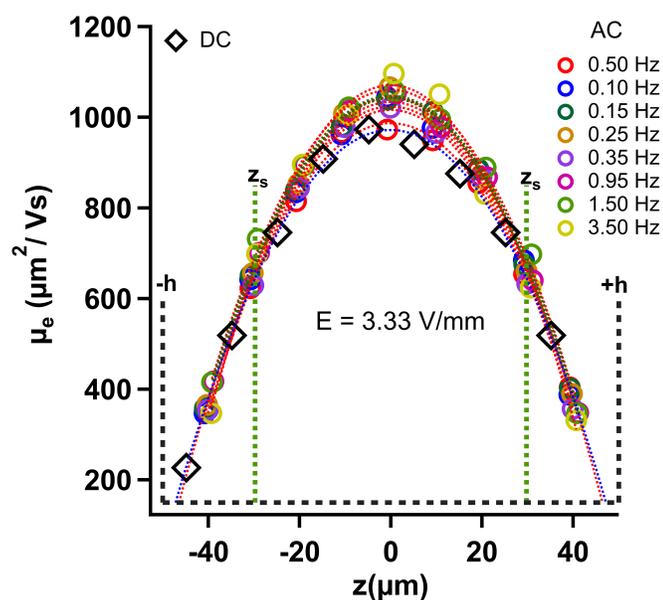
Figure 5.7: AC (sine wave) and DC electrophoretic mobilities μ_e. The mobility profile measured in a closed capillary with $z = 100$ μm at different frequencies as a function of z. This plot shows that μ_e is independent of f, because the mobility values at $z = z_s$ are very close for all frequencies.
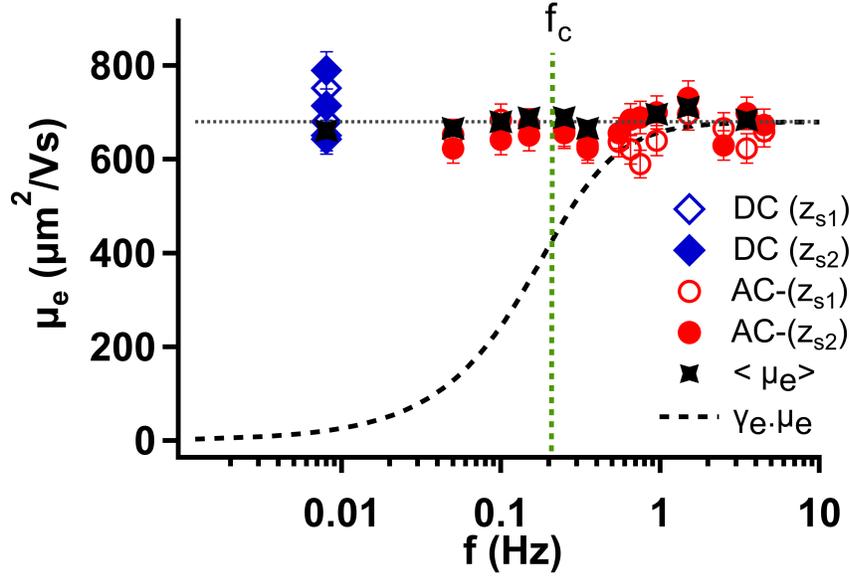
Figure 5.8: Electrophoretic mobilities μ_e as a function of f. **a)** The two measurements z_{s1} and z_{s2} are obtained from the two stationary layers on either side of the parabolic depth (z) profile. The difference between the mobilities value measured at z_{s1} and z_{s2} for AC is $\sim 30\ \mu\mathrm{m}^2/Vs$ and for DC, it is $\sim 40\ \mu\mathrm{m}^2/Vs$. Both the AC and DC mobilities are in agreement with each other within the uncertainty. The attenuation factor γ_e (shown as a dashed line that decreases to zero at low frequency) is significant for $f < f_c$.

$v_E \propto E$ by calculating μ_e as a function of E.

The mobility profiles at different frequencies as a function of z is shown in Fig. 5.7. From the obtained mobility profiles, we calculate μ_e at z_s as a function of f (Fig. 5.8). In Fig. 5.8, we plot μ_e obtained from the two stationary layers on either side of the parabolic profile as shown in Fig. 5.7. The red circles indicate AC measurements and the blue diamond denotes the DC measurements. All the mobilities are in the same range. Hence, DC and AC experiments agree with each other and μ_e is independent of f.

Ma *et al.* [128] report a regime in an aqueous system for frequencies $f < 100\mathrm{Hz}$ where μ_e is independent of f and above a certain frequency, μ_e decreases: this is
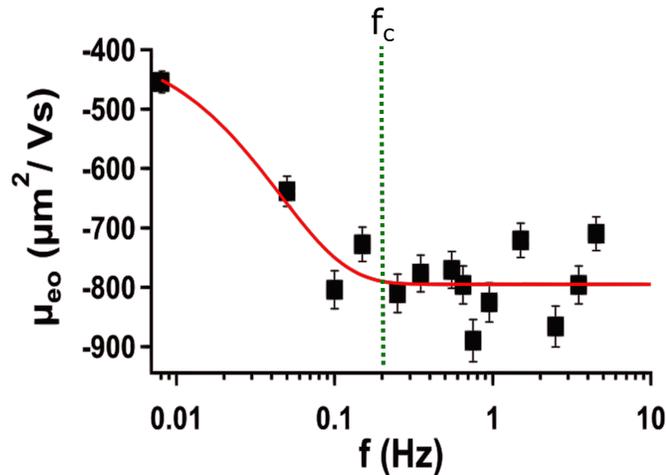
Figure 5.9: Electro-osmotic mobilities μ_{eo} as a function of f. μ_{eo} decreases with increasing frequency and is constant at higher frequencies, i.e, $f > f_c$.

called the corner frequency. In their work, the corner frequency is independent of the electrode polarization characteristic frequency f_c; it is set by the time it takes for ions to accumulate at the colloidal double layer, and possibly to form a condensed layer of ions, as the voltage is increased. This corner frequency changes with the salt concentration. Ma et $al.$ also pointed out that electrode polarization is expected to be relevant when $\Omega = 2\pi f L/D\kappa \sim 0.5$, corresponding to $f_c \sim 0.15$ Hz in our experiments.

We, however, observe that μ_e does not change much when the frequency is decreased. That is, we neither see evidence for a corner frequency below which the observed mobility increases, nor the electrode polarization effect below f_c (shown by the vertical green dashed line, Fig. 5.8). Indeed, even the DC measurement gives the same μ_e. A crude estimate for a lower bound for the corner frequency is simply given by $D\kappa/(2\pi a) \sim 1200$ Hz, and would not be observable in our experiments. On the other hand, the predicted μ_e, incorporating an electrode polarization correction given by the product $\gamma_e.\mu_e$, decreases below f_c as shown (dashed line) in Fig. 5.8.

Thus, contrary to our initial expectations, DC measurements provide realistic values of electrophoretic mobilities in a low polar solvent. This could be due to less ions present in the suspension and in a low polar solvent, we can not add salt beyond a threshold value. In any case, charge induced effects appear to be more significant in aqueous systems.

In Fig. 5.7, we also notice that the parabolic profiles do not overlap on the axis (centre) of the capillary. From eq. 5.9, we know that $v_p(0) = v_e + v_{eo}/2$, hence it is possible this non-overlap comes from the electro-osmotic contribution. We, therefore, calculate the electro-osmotic mobility μ_{eo} using eq. 5.9 and eq. 5.10 and plot it as a function of f in Fig. 5.9. We find that μ_{eo} decreases with increasing frequency and remains constant at $f > f_c$.

We carried out an additional check. The average electrophoretic mobility, calculated as $\langle \mu_e \rangle = \frac{1}{2h} \int_{-h}^{+h} v_p(z) dz$ should also give the electrophoretic mobility (Ref. [124] in section 4.3.1) and this method uses the entire profile. These values for $\langle \mu_e \rangle$ are also shown in Fig. 5.8, and these values (black stars) are consistent.

Further, we switch the function generator from sine wave to square wave as that mimics the DC driving over shorter and shorter timescales. In this method, we change the AC sine wave to a square wave using the function generator. This means that we do not need to manually switch the direction of particle motion like we did in the DC experiments (section 5.3.1). Therefore, we can directly get the time associated with the particle motion from a periodic square wave unlike the DC experiment.

In Fig. 5.10, we show an example of a square wave experiment at $f = 0.05$ Hz and compare it with the AC sine wave at $f = 0.05$ Hz. The displacement response to a sine wave driving should be sinusoidal, while the displacement response to a square wave should be triangular. The MSD for a sine wave is also sinusoidal (as shown

in section 5.3.2). In contrast, for displacement that is a triangular wave, the MSD should be concave. Instead, we see, once again, a response that appears sinusoidal (Fig. 5.10). This is likely due to the fact that our MSD is averaged over start times.

Regardless, as a rough indicator of the difference between sine and square wave driving, one can use the values of the first peak of the MSD. In Fig. 5.10, for sinusoidal driving (at 0.15 Hz) the peak is at 147 μm^2, while for square-wave driving it is at 227 μm^2, and the diffusive part is 3.0 μm^2 at the t corresponding to the sinusoidal peak. This indicates an MSD ratio of $(227\text{-}3)/(147\text{-}3) = 1.56$ and theoretically, it should be $\pi/2$, which is 1.57 [129]. Thus the square wave response is consistent with the sine wave response.

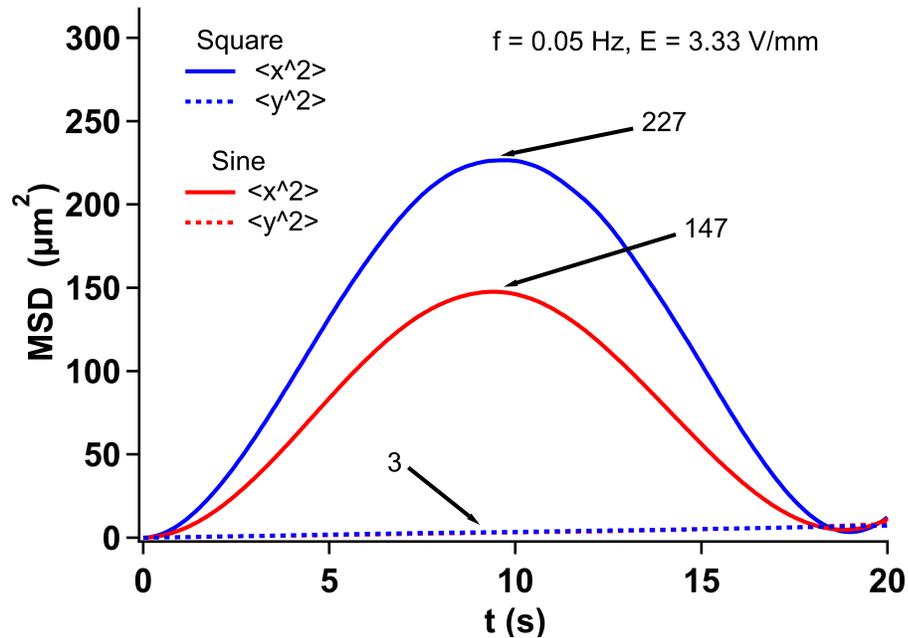Figure 5.10: Comparison between AC sine and square wave experiment where output of the AC sine wave is a sine wave (red curve) with peak at 147 μm^2 and for a square wave is again a sine wave (blue curve) with peak at 227 μm^2. The diffusive part is at 3 μm^2 corresponding to the sinusoidal peak. The ratio of square and sine wave amplitudes, i.e., $(227\text{-}3)/(147\text{-}3)$, is equivalent to $\pi/2$.

We conclude that the mobilities from the DC and AC experiments are in agreement with each other. So, we average over all the mobilities and thus obtain $\mu_e \approx (680 \pm 10)\mu m^2/\text{Vs}$. We use the obtained μ_e to calculate the ζ-potential. For dielectric constant $\epsilon = 6.1 \pm 0.3$ and viscosity $\eta = 2.12 \pm 0.05$ mPas, the dimensionless mobility $M = 3\eta e\mu_e/2\epsilon_s\epsilon_o k_B T = 1.6 \pm 0.1$. The dimensionless zeta potential Ψ, obtained for $\kappa a = 7.2 \pm 0.1$ and $M = 1.6 \pm 0.1$ by using O'Brien and White's plot [123] is approximately $\Psi = 1.5 \pm 0.1$ and the ζ-potential $= \Psi k_B T/e \approx (38 \pm 3)$ mV. This is further used to calculate the particle charge (Z) using eq. 5.6. Hence, $Z = 891 \pm 117e$.

5.4 Conclusions and future work

We perform AC colloidal microelectrophoresis experiments at different frequencies that has not been carried out before in a partially polar solvent. We use a combination of confocal laser scanning microscopy, electrophoresis and particle tracking algorithms to calculate the mobility of a charged colloidal particle. Many researchers have previously suggested that it is important to make AC electrophoresis measurements in order to check for electrode polarization effects in both aqueous systems and non-aqueous systems [1, 121, 128]. Therefore, we carried out AC measurements at different frequencies and compared it with the DC measurements. Effectively, no measurement is truly DC; we estimate our "DC" measurement has a direction-switching frequency of 0.008 Hz. Nevertheless, it appears that at least for our non-aqueous colloidal system (which does not have very high ion concentrations) we do not see a noticeable electrode polarization effect at $f < f_c$. In addition, we find that DC measurements provide realistic values of electrophoretic mobilities in a low polar solvent.

We find that the electrophoretic mobilities are independent of f whereas electroos-motic mobilities decreases with increasing f and then saturate at $f > f_c$ (Fig. 5.9). There is limited literature on the frequency dependence of the electroosmotic mobil-ity. Further theoretical work would help us in understanding the effect of frequency on electroosmotic mobility.

We report electrophoresis measurements at much lower frequencies than what Ma *et al.* [128] reported in their work with aqueous suspensions i.e, $f < 1$ Hz and in this regime mobilities are independent of frequency, whereas significant attenuation of field is expected even for our non-aqueous system. For an aqueous system, Ma *et al.* [128] suggested the need to consider electrode polarization when the dimensionless frequency $\Omega \approx 1$. Therefore, as a future work one can perform both DC and AC experiment for colloids in an aqueous solvent as a function of f to see any effects due to polarization. Further, we calculate the charge Z on particles by taking average over all the mobilities. By using the theory of electrophoresis for $\kappa\sigma \gg 1$, we obtain $Z = 891 \pm 117e$.

In our experiments, in order to obtain a hard-sphere-like system, we add the salt tetrabutylammonium chloride to the colloidal suspension (discussed earlier in this thesis). In such a system, it has previously been reported that there is a charge reversal on colloids when salt is added because of the accumulation of counterions near the colloidal particles [65, 130]. In a low-polar solvent, we do not know the threshold salt concentration at which the charge reversal happens. In the future, one could use the AC microelectrophoresis technique to study the kinetics of particles to determine the threshold salt concentration at which the charge reversal first occurs.

Chapter 6

Summary

Colloids are microscopic particles, with a dimension ranging from few nanometers to several micrometers, that are suspended in a fluid and undergo Brownian motion. When colloids are suspended in a solvent that contains positive and negative ions, an electric double layer forms around the colloids. The inner layer consists of the ions located on the surface or near the particles, for example, a negatively charged particle has negative ions in the inner layer. The outer or diffuse layer consists of the counterions and is thicker than the inner layer. The thickness of the double layer can be varied by changing the salt concentration in the solvent. This thickness is a measure of the distance over which the colloids interact electrostatically with other colloids via a screened Coulomb potential.

The micron-sized colloids used in this thesis are sufficiently large to study with light microscopy. We closely match the refractive index of the colloids and solvent to suppress the scattering of light that allows confocal microscopy studies of colloidal suspensions. In this thesis, confocal microscopy is used as the main experimental technique to study the colloidal system in real-time, real space and at a single-particle level.

The colloid-colloid interaction can be further manipulated, for example, by adding non-adsorbing polymer to induce the attractive "depletion" interaction or by using various other methods to produce anisotropic interactions. Depletion interactions between colloids, first predicted by Asakura and Oosawa, lead to a separation between colloid-rich (liquid-like) and colloid-poor (gas-like) phases, and at high polymer concentration, can lead to network-forming gels. A second interaction is the electric-field-induced dipolar anisotropic interaction, that behaves as a switch and provides active control of a colloidal system. Using these two interactions in tandem provides fine, tunable control over colloidal phase transitions. At sufficiently large external electric field, the polarization of the colloids due to the external field results in structural transitions.

In Chapter 1, we discuss the background theory of colloid-polymer research and recent developments, and put them in a broader perspective. In Chapter 2, we discuss our colloidal system consisting of fluorescent-labeled polymethyl methacrylate (PMMA) spherical colloids suspended in the solvent mixtures of cyclohexyl bromide (CHB) and cis-trans decahydronapthalene (decalin). In such a system, it is possible to create an electrical double layer that can be adjusted by adding the salt tetrabutyl ammonium bromide (TBAB) to the suspension to screen the electrostatic interactions. Also, we characterize the polymer and measure its size in CHB/decalin by using NMR and DLS.

As polymer concentration increases, the colloid-colloid attractive interaction becomes stronger. In such a system we examine the effect of an electric-field induced dipolar interaction. In Chapter 3, we report a new "dipolar-depletion" phase diagram by varying both the polymer concentration (depletion interactions) and field strength

(dipolar interactions). We present phase transitions in the dipolar-depletion phase diagram where the external electric field is used as a switch to reversibly and repeatedly change phase in a sample. The competition between dipolar and depletion interactions gives rise to a rich phase behaviour that includes ordered (DIO) and disordered (DID and DCG) regimes. In our experiments, we use hard-sphere-like colloids and polymer of size much smaller than the size of a colloid.

A switchable control parameter means that we have access to studying time-dependent phenomena. In Chapter 4, we discuss time-dependent phenomena in the dipolar-depletion phase diagram: both transient kinetics during phase change as well as steady-state colloidal particle dynamics. We present the first experiments exploring colloidal kinetics using switchable dipolar interactions as a tool to probe reversibility in both ordered and disordered regimes of the dipolar-depletion phase diagram. In addition, we establish a method to accelerate aging in a colloid-polymer mixture by cycling through the field. We believe our accelerated aging may allow the studies of processes in a system where the time required to see collapse in gels can be months or even years. Such field-induced interactions can also be useful in finding applications for electrorheological fluids.

Electrokinetics in colloids in aqueous media, where the dielectric constant $\epsilon_s \sim 80$ and the electrical conductivity is large, is well studied. In apolar media, where $\epsilon_s \sim 2$, the conductivity is extremely low, and such apolar systems behave like pure dielectrics. In the partially polar solvents used in this study, with $\epsilon_s \sim 6$ and a small but measurable conductivity, electrokinetics has been studied extensively. In Chapter 5, we describe micro-electrophoresis measurements at different AC frequencies: these are the first such measurements for colloids in a partially-polar solvent. We compare our AC micro-electrophoresis measurements with a DC micro-electrophoresis method

that has previously been used to calculate the mobility and charge in a low polar solvent. It has been suggested previously that effects due to accumulation of charge on the electrodes, or electrode polarization, should be significant in static (DC) fields. In our experiments, we find that the AC and DC mobilities are in the same range: thus there are no effects due to electrode polarization. We also measured the electro-osmotic flows as a function of frequency, and this does show an increase at the lowest frequencies. As a final point, from the micro-electrophoresis measurements, we obtain the Zeta potential and charge on the colloids, thus completely characterizing our model system.

We hope that this model system will find extensive use in understanding the kinetics of cluster-forming systems and systems undergoing gelation.

Bibliography

[1] E. Hayden, Z. Aljabal, and A. Yethiraj. Frequency-dependent solvent impedance and colloid microelectrophoresis measurements in partially polar solvents. *Langmuir*, 33(19):4781–4788, 5 2017.

[2] L. J. Teece, M. A. Faers, and P. Bartlett. Ageing and collapse in gels with long-range attractions. *Soft Matter*, 7(4):1341–1351, 2011.

[3] R. Brown. A brief account of microscopical observations made in the months of june, july and august 1827, on the particles contained in the pollen of plants; and on the general existence of active molecules in organic and inorganic bodies. *The Philosophical Magazine*, 4(21):161–173, 1828.

[4] A. Einstein. On the movement of small particles suspended in a stationary liquid demanded by the molecular-kinetic theory of heat (english translation, 1956). *Investigations on the theory of the Brownian movement*, 1905.

[5] W. B. Russel, D. A. Saville, and W. R. Schowalter. *Colloidal dispersions*. Cambridge University Press, 1991.

[6] P. N. Pusey and W. Van Megen. Phase behaviour of concentrated suspensions of nearly hard colloidal spheres. *Nature*, 320(6060):340–342, 1986.

[7] W. C. K. Poon. Colloids as big atoms. *Science*, 304(5672):830–831, 5 2004.

[8] A. van Blaaderen and P. Wiltzius. Real-space structure of colloidal hard-sphere glasses. *Science*, 270(5239):1177–1179, 11 1995.

[9] K. Lin, J. C. Crocker, V. Prasad, A. Schofield, D. A. Weitz, T. C. Lubensky, and A. G. Yodh. Entropically driven colloidal crystallization on patterned surfaces. *Physical Review Letters*, 85(8):1770–1773, 8 2000.

[10] J. A. Weiss, D. W. Oxtoby, D. G. Grier, and C. A. Murray. Martensitic transition in a confined colloidal suspension. *The Journal of Chemical Physics*, 103(3):1180–1190, 7 1995.

[11] A. P. Gast and W. B. Russel. Simple ordering in complex fluids. *Physics Today*, 51(12):24–30, 12 1998.

[12] K. N. Pham. Multiple glassy states in a simple model system. *Science*, 296(5565):104–106, 4 2002.

[13] J. K. G. Dhont. *An introduction to dynamics of colloids*. Elsevier, 1996.

[14] H. Löwen and G. Kramposthuber. Optimal effective pair potential for charged colloids. *Europhysics Letters*, 23(9):673, 1993.

[15] S. Alexander, P. M. Chaikin, P. Grant, G. J. Morales, P. Pincus, and D. Hone. Charge renormalization, osmotic pressure, and bulk modulus of colloidal crystals: Theory. *The Journal of Chemical Physics*, 80(11):5776–5781, 1984.

[16] B. Derjaguin and L. Landau. The theory of stability of highly charged lyophobic sols and coalescence of highly charged particles in electrolyte solutions. *Acta Physicochim. URSS*, 14(633-52):58, 1941.

[17] E. J. W. Verwey, J. T. G. Overbeek, and K. Van Nes. *Theory of the stability of lyophobic colloids: the interaction of sol particles having an electric double layer*. Elsevier Publishing Company, 1948.

[18] C. J. Dibble, M. Kogan, and M. J. Solomon. Structure and dynamics of colloidal depletion gels: Coincidence of transitions and heterogeneity. *Physical Review E - Statistical, Nonlinear, and Soft Matter Physics*, 74(4):1–11, 2006.

[19] P. J. Lu, J. C. Conrad, H. M. Wyss, A. B. Schofield, and D. A. Weitz. Fluids of clusters in attractive colloids. *Physical Review Letters*, 96(2):1–4, 2006.

[20] J. H. Cho, R. Cerbino, and I. Bischofberger. Emergence of multiscale dynamics in colloidal gels. *Physical Review Letters*, 124(8):88005, 2020.

[21] J. C. Loudet, P. Poulin, and P. Barois. Edge dislocations of colloidal chains suspended in a nematic liquid crystal. *Europhysics Letters*, 54(2):175–181, Apr 2001.

[22] Q. Chen, J. K. Whitmer, S. Jiang, S. C. Bae, E. Luijten, and S. Granick. Supracolloidal reaction kinetics of janus spheres. *Science*, 331(6014):199–202, 2011.

[23] Z. Gong, T. Hueckel, G.-R. Yi, and S. Sacanna. Patchy particles made by colloidal fusion. *Nature*, 550(7675):234–238, 2017.

[24] Z. Zhang and S. C. Glotzer. Self-assembly of patchy particles. *Nano letters*, 4(8):1407–1413, 2004.

[25] U. Dassanayake, S. Fraden, and A. van Blaaderen. Structure of electrorheological fluids. *The Journal of Chemical Physics*, 112(8):3851–3858, 2 2000.

[26] R. Tao and J. M. Sun. Three-dimensional structure of induced electrorheological solid. *Physical Review Letters*, 67(3):398–401, 7 1991.

[27] J. E. Martin, J. Odinek, and T. C. Halsey. Evolution of structure in a quiescent electrorheological fluid. *Physical Review Letters*, 69(10):1524–1527, 9 1992.

[28] A. Kuijk, T. Troppenz, L. Filion, A. Imhof, R. van Roij, M. Dijkstra, and A. van Blaaderen. Effect of external electric fields on the phase behavior of colloidal silica rods. *Soft Matter*, 10(33):6249–6255, 7 2014.

[29] M. Kamp, N. A. Elbers, T. Troppenz, A. Imhof, R. Dijkstra, M.and van Roij, and A. van Blaaderen. Electric-field-induced lock-and-key interactions between colloidal spheres and bowls. *Chemistry of Materials*, 28(4):1040–1048, 2 2016.

[30] H. R. Vutukuri, A. F. Demirörs, B. Peng, P. D. J. van Oostrum, A. Imhof, and A. van Blaaderen. Colloidal analogues of charged and uncharged polymer chains with tunable stiffness. *Angewandte Chemie International Edition*, 51(45):11249–11253, 2012.

[31] J. P. Singh, P. P. Lele, F. Nettesheim, N. J. Wagner, and E. M. Furst. One- and two-dimensional assembly of colloidal ellipsoids in ac electric fields. *Physical Review E*, 79(5):50401, 5 2009.

[32] A. M. Almudallal and I. Saika-Voivod. Simulation of a two-dimensional model for colloids in a uniaxial electric field. *Physical Review E - Statistical, Nonlinear, and Soft Matter Physics*, 84(1):1–9, 2011.

[33] R. Tao and Qi Jiang. Simulation of structure formation in an electrorheological fluid. *Physical Review Letters*, 73(1):205–208, 1994.

[34] J. E. Martin, J. Odinek, T. C. Halsey, and R. Kamien. Structure and dynamics of electrorheological fluids. *Physical Review E*, 57(1):756–775, 1 1998.

[35] A. Yethiraj and A. van Blaaderen. A colloidal model system with an interaction tunable from hard sphere to soft and dipolar. *Nature*, 421(6922):513–517, 1 2003.

[36] A. Yethiraj, A. Wouterse, B. Groh, and A. van Blaaderen. Nature of an electric-field-induced colloidal martensitic transition. *Physical Review Letters*, 92(5):4, 2004.

[37] M. E. Leunissen, C. G. Christova, A.P. Hynninen, C. P. Royall, A. I. Campbell, A. Imhof, M. Dijkstra, R. van Roij, and A. van Blaaderen. Ionic colloidal crystals of oppositely charged particles. *Nature*, 437(7056):235–240, 9 2005.

[38] A. K. Agarwal and A. Yethiraj. Low-density ordered phase in brownian dipolar colloidal suspensions. *Physical Review Letters*, 102(19), 5 2009.

[39] P. S. Mohanty, P. Bagheri, S. Nöjd, A. Yethiraj, and P. Schurtenberger. Multiple path-dependent routes for phase-transition kinetics in thermoresponsive and field-responsive ultrasoft colloids. *Physical Review X*, 5(1):11030, 3 2015.

[40] V. J. Anderson and H. N. W. Lekkerkerker. Insights into phase transition kinetics from colloid science. *Nature*, 416(6883):811–815, 4 2002.

[41] S. Asakura and F. Oosawa. On interaction between two bodies immersed in a solution of macromolecules. *The Journal of Chemical Physics*, 22(7):1255–1256, 7 1954.

[42] A. V. Vrij. Polymers at interfaces and the interactions in colloidal dispersions. *Pure and Applied Chemistry*, 48(4):471–483, 1976.

[43] R. I. Feigin and D. H. Napper. Depletion stabilization and depletion flocculation. *Journal of Colloid and Interface Science*, 75(2):525–541, 1980.

[44] B. Vincent, P. F. Luckham, and F. A. Waite. The effect of free polymer on the stability of sterically stabilized dispersions. *Journal of Colloid And Interface Science*, 73(2):508–521, 1980.

[45] A. Yethiraj, C. K. Hall, and R. Dickman. Interaction between colloids in solutions containing dissolved polymer. *Journal of Colloid And Interface Science*, 151(1):102–117, 1992.

[46] S. Ramakrishnan, M. Fuchs, K. S. Schweizer, and C. F. Zukoski. Concentration fluctuations in a model colloid-polymer suspension: Experimental tests of depletion theories. *Langmuir*, 18(4):1082–1090, 2002.

[47] A. P. Gast, C. K. Hall, and W. B. Russel. Polymer-induced phase separations in nonaqueous colloidal suspensions. *Journal of Colloid And Interface Science*, 96(1):251–267, 1983.

[48] H. N. Lekkerkerker, W. C. Poon, P. N. Pusey, A. Stroobants, and P. B. Warren. Phase behaviour of colloid + polymer mixtures. *Europhysics Letters*, 20(6):559–564, 1992.

[49] P. N. Pusey, W. C. K. Poon, S. M. Ilett, and P. Bartlett. Phase behaviour and structure of colloidal suspensions. *Journal of Physics: Condensed Matter*, 6(23A):A29, 1994.

[50] F. L. Calderon, J. Bibette, and J. Biais. Experimental phase diagrams of polymer and colloid mixtures. *Europhysics Letters*, 23(9):653, 1993.

[51] S. M. Ilett, A. Orrock, W. C. K. Poon, and P. N. Pusey. Phase behavior of a model colloid-polymer mixture. *Physical Review E*, 51(2):1344–1352, 2 1995.

[52] A. Vrij. Polymers at interfaces and the interactions in colloidal dispersions. *Pure and Applied Chemistry*, 48(4):471–483, 1 1976.

[53] C. P. Royall, D. G. A. L. Aarts, and H. Tanaka. Fluid structure in colloid–polymer mixtures: the competition between electrostatics and depletion. *Journal of Physics: Condensed Matter*, 17(45):S3401–S3408, 11 2005.

[54] A. Fortini, M. Dijkstra, and R. Tuinier. Phase behaviour of charged colloidal sphere dispersions with added polymer chains. *Journal of Physics: Condensed Matter*, 17(50):7783–7803, 12 2005.

[55] A. I. Campbell, V. J. Anderson, J. S. van Duijneveldt, and P. Bartlett. Dynamical arrest in attractive colloids: The effect of long-range repulsion. *Physical Review Letters*, 94(20):208301, 2005.

[56] P. J. Lu and D. A. Weitz. Colloidal particles: Crystals, glasses, and gels. *Annual Review of Condensed Matter Physics*, 4(1):217–233, 2013.

[57] D. Bonn and M. M. Denn. Yield stress fluids slowly yield to analysis. *Science*, 324(5933):1401–1402, 2009.

[58] J. Rouwhorst, C. Ness, S. Stoyanov, A. Zaccone, and P. Schall. Nonequilibrium continuous phase transition in colloidal gelation with short-range attraction. *Nature Communications*, 11(1):1–8, 2020.

[59] P. J. Lu, E. Zaccarelli, F. Ciulla, A. B. Schofield, F. Sciortino, and D. A. Weitz. Gelation of particles with short-range attraction. *Nature*, 453(7194):499–503, 2008.

[60] D. A. Weitz and M. Oliveria. Fractal structures formed by kinetic aggregation of aqueous gold colloids. *Physical Review Letters*, 52(16):1433–1436, 1984.

[61] C. P. Royall, M. A. Faers, S. L. Fussell, and J. E. Hallett. Real space analysis of colloidal gels: Triumphs, challenges and future directions. *Journal of Physics Condensed Matter*, 33(45):453002, 2021.

[62] S. Aime, L. Ramos, and L. Cipelletti. Microscopic dynamics and failure precursors of a gel under mechanical load. *Proceedings of the National Academy of Sciences of the United States of America*, 115(14):3587–3592, 2018.

[63] N. A. M. Verhaegh, D. Asnaghi, H. N. W. Lekkerkerker, M. Giglio, and L. Cipelletti. Transient gelation by spinodal decomposition in colloid-polymer mixtures. *Physica A: Statistical Mechanics and its Applications*, 242(1-2):104–118, 1997.

[64] E. Zaccarelli, S. V. Buldyrev, E. La Nave, A. J. Moreno, I. Saika-Voivod, F. Sciortino, and P. Tartaglia. Model for reversible colloidal gelation. *Physical Review Letters*, 94(21), 6 2005.

[65] M. E. Leunissen. *Manipulating colloids with charges and electric fields*. Utrecht University, 2007.

[66] T. Vissers. *Oppositely charged colloids out of equilibrium*. Utrecht University, 2010.

[67] R. M. Fuoss. Dependence of the walden product on dielectric constant. *Proceedings of the National Academy of Sciences of the United States of America*, 45(6):807, 1959.

[68] M. N. van der Linden. *Long-range repulsive charged colloids in and out of equilibrium*. Utrecht University, 2013.

[69] L. Antl, J. W. Goodwin, R. D. Hill, R. H. Ottewill, S. M. Owens, S. Papworth, and J. A. Waters. The preparation of poly(methyl methacrylate) latices in non-aqueous media. *Colloids and Surfaces*, 17(1):67–78, 1986.

[70] F. Brochard and P. G. De Gennes. Dynamical scaling for polymers in theta solvents. *Macromolecules*, 10(5):1157–1161, 1977.

[71] C. Clasen, J. P. Plog, W.-M. Kulicke, M. Owens, C. Macosko, L. E. Scriven, M. Verani, and G. H. McKinley. How dilute are dilute solutions in extensional flows? *Journal of Rheology*, 50(6):849–881, 11 2006.

[72] Q. Ying and B. Chu. Overlap concentration of macromolecules in solution. *Macromolecules*, 20(2):362–366, 1987.

[73] B. Dünweg, D. Reith, M. Steinhauser, and K. Kremer. Corrections to scaling in the hydrodynamic properties of dilute polymer solutions. *The Journal of Chemical Physics*, 117(2):914–924, 7 2002.

[74] L. J. Fetters, N. Hadjichristidis, J. S. Lindner, and J. W. Mays. Molecular weight dependence of hydrodynamic and thermodynamic properties for well-defined linear polymers in solution. *Journal of Physical and Chemical Reference Data*, 23(4):619–640, 7 1994.

[75] M. Minsky. Memoir on inventing the confocal scanning microscope. *Scanning*, 10(1 988):128–138, 1987.

[76] J. P. Hoogenboom. *Colloidal epitaxy: a real-space analysis*. PhD thesis, [s.n.], S.l., 2002.

[77] V. Prasad, D. Semwogerere, and E. R. Weeks. Confocal microscopy of colloids. *Journal of Physics: Condensed Matter*, 19(11):113102, 3 2007.

[78] J. C. Crocker and D. G. Grier. Methods of digital video microscopy for colloidal studies. *Journal of Colloid and Interface Science*, 179(1):298–310, 1996.

[79] J. C. Crocker and E. R. Weeks. Particle tracking using idl. http://www.physics.emory.edu/faculty/weeks//idl/.

[80] P. J. Steinhardt, D. R. Nelson, and M. Ronchetti. Bond-orientational order in liquids and glasses. *Physical Review B*, 28(2):784–805, 1983.

[81] C. A. Murray. *Bond-Orientational Order in Condensed Matter Systems*. Springer-Verlag, New York., 1992.

[82] W. Lechner and C. Dellago. Accurate determination of crystal structures based on averaged local bond order parameters. *Journal of Chemical Physics*, 129(11), 2008.

[83] P. Bagheri, A. M. Almudallal, A. Yethiraj, and K. M. Poduska. Quantitative metrics for assessing positional and orientational order in colloidal crystals. *Langmuir*, 31(30):8251–8259, 2015.

[84] J. A. Weiss, D. W. Oxtoby, D. G. Grier, and C. A. Murray. Martensitic transition in a confined colloidal suspension. *The Journal of Chemical Physics*, 103(3):1180–1190, 1995.

[85] A. Yethiraj, A. Wouterse, B. Groh, and A. van Blaaderen. Nature of an electric-field-induced colloidal martensitic transition. *Physical Review Letters*, 92(5):4, 2004.

[86] D. T. Lee and B. J. Schachter. Two algorithms for constructing a Delaunay triangulation. *International Journal of Computer & Information Sciences*, 9(3):219–242, 1980.

[87] A. P. Gast, W. B. Russel, and C. K. Hall. An experimental and theoretical study of phase transitions in the polystyrene latex and hydroxyethylcellulose system. *Journal of Colloid and Interface Science*, 109(1):161–171, 1 1986.

[88] W. C. K. Poon. The physics of a model colloid polymer mixture. *Journal of Physics: Condensed Matter*, 14(33):R859–R880, 8 2002.

[89] A. Stukowski. Visualization and analysis of atomistic simulation data with OVITO-the Open Visualization Tool. *Modelling and simulation in materials science and engineering*, 18(1), 1 2010.

[90] U. Gasser, E. R. Weeks, A. Schofield, P. N. Pusey, and D. A. Weitz. Real-space imaging of nucleation and growth in colloidal crystallization. *Science*, 292(5515):258–262, 2001.

[91] A. E. Larsen and D. G. Grier. Like-charge attractions in metastable colloidal crystallites. *Nature*, pages 230–233, 1997.

[92] E. R. Weeks, J. C. Crocker, A. C. Levitt, A. Schofield, and D. A. Weitz. Three-dimensional direct imaging of structural relaxation near the colloidal glass transition. *Science*, 287(5453):627–631, 2000.

[93] H. Tanaka, J. Meunier, and D. Bonn. Nonergodic states of charged colloidal suspensions: Repulsive and attractive glasses and gels. *Physical Review E - Statistical, Nonlinear, and Soft Matter Physics*, 69(3 1):1–6, 2004.

[94] G. Foffi, G. D. McCullagh, A. Lawlor, E. Zaccarelli, K. A. Dawson, F. Sciortino, P. Tartaglia, D. Pini, and G. Stell. Phase equilibria and glass transition in colloidal systems with short-ranged attractive interactions: Application to protein crystallization. *Physical Review E - Statistical Physics, Plasmas, Fluids, and Related Interdisciplinary Topics*, 65(3):1–17, 2002.

[95] N. Koumakis and G. Petekidis. Two step yielding in attractive colloids: Transition from gels to attractive glasses. *Soft Matter*, 7(6):2456–2470, 2011.

[96] H. Sedgwick, S. U. Egelhaaf, and W. C. K. Poon. Clusters and gels in systems of sticky particles. *Journal of Physics: Condensed Matter*, 16(42):S4913–S4922, 10 2004.

[97] F. Sciortino. One liquid, two glasses. *Nature Materials*, 1(3):145–146, 2002.

[98] K. A. Dawson. The glass paradigm for colloidal glasses, gels, and other arrested states driven by attractive interactions. *Current Opinion in Colloid and Interface Science*, 7(3-4):218–227, 2002.

[99] R. Metzler. Brownian motion and beyond: first-passage, power spectrum, non-Gaussianity, and anomalous diffusion. *Journal of Statistical Mechanics: Theory and Experiment*, 2019(11):ab4988, 2019.

[100] J. L. Barrat and J. P. Hansen. *Basic concepts for simple and complex liquids*. Cambridge University Press, 2003.

[101] M. L. Kilfoil, E. E. Pashkovski, J. A. Masters, D. A. Weitz, P. Warren, M. Nicodemi, W. T. Coffey, B. U. Felderhof, and R. C. Ball. Dynamics of weakly aggregated colloidal particles. *Philosophical Transactions of the Royal Society A: Mathematical, Physical and Engineering Sciences*, 361(1805):753–766, 2003.

[102] L. J. Teece, J. M. Hart, K. Y. N. Hsu, S. Gilligan, M. A. Faers, and P. Bartlett. Gels under stress: The origins of delayed collapse. *Colloids and Surfaces A: Physicochemical and Engineering Aspects*, 458(1):126–133, 2014.

[103] G. J. Fleer and R. Tuinier. Analytical phase diagrams for colloids and non-adsorbing polymer. *Advances in colloid and interface science*, 2008.

[104] I. Golding and E. C. Cox. Physical nature of bacterial cytoplasm. *Physical Review Letters*, 96(9):098102, 2006.

[105] J. P. Bouchaud and A. Georges. Anomalous diffusion in disordered media: statistical mechanisms, models and physical applications. *Physics reports*, 195(4-5):127–293, 1990.

[106] E. Barkai, Y. Garini, and R. Metzler. of single molecules in living cells. *Physics Today*, 65(8):29, 2012.

[107] M. J. Saxton and K. Jacobson. Single-particle tracking: applications to membrane dynamics. *Annual Review of Biophysics and Biomolecular Structure*, 26(1):373–399, 1997.

[108] W. K. Kegel and A. van Blaaderen. Direct observation of dynamical heterogeneities in colloidal hard-sphere suspensions. *Science*, 287(5451):290–293, 2000.

[109] E. Zaccarelli and W. C. K. Poon. Colloidal glasses and gels: The interplay of bonding and caging. *Proceedings of the National Academy of Sciences*, 106(36):15203–15208, 2009.

[110] E. R. Weeks and D. A. Weitz. Subdiffusion and the cage effect studied near the colloidal glass transition. *Chemical Physics*, 284(1-2):361–367, 2002.

[111] F. Donado, J. M. Sausedo-Solorio, and R. E. Moctezuma. Dynamical and structural properties of a granular model for a magnetorheological fluid. *Physical Review E*, 95(2):1–10, 2017.

[112] R. Poling-Skutvik, R. Krishnamoorti, and J. C. Conrad. Size-Dependent Dynamics of Nanoparticles in Unentangled Polyelectrolyte Solutions. *ACS Macro Letters*, 4(10):1169–1173, 2015.

[113] F. Booth. Theory of electrokinetic effects. *Nature*, 161(4081):83–86, 1 1948.

[114] S. Wall. The history of electrokinetic phenomena. *Current Opinion in Colloid & Interface Science*, 15(3):119–124, 2010.

[115] O. D. Velev, S. Gangwal, and D. N. Petsev. Particle-localized AC and DC manipulation and electrokinetics. *Annual Reports Section "C" (Physical Chemistry)*, 105:213, 2009.

[116] R. J. Hunter. *Foundations of colloid science.* Oxford University Press, Oxford ; New York, 2nd ed edition, 2001.

[117] T. Vissers, A. Imhof, F. Carrique, Á. V. Delgado, and A. van Blaaderen. Electrophoresis of concentrated colloidal dispersions in low-polar solvents. *Journal of Colloid and Interface Science*, 361(2):443–455, 9 2011.

[118] T. Lin, T. Kodger, and D. Weitz. Transport of charged colloidal particles in a nonpolar solvent in response to an electric field. In *APS March Meeting Abstracts*, volume 2013, pages A30–002, 2013.

[119] J. Zhou and F. Schmid. Computer simulations of charged colloids in alternating electric fields. *European Physical Journal: Special Topics*, 222(11):2911–2922, 2013.

[120] J. Ma, T. Stangner, and F. Kremer. Frequency dependence of the electrophoretic mobility for single colloids as measured using optical tweezers. *Physical Review Fluids*, 2(10):104306, 10 2017.

[121] J. Zhou and F. Schmid. Computer simulations of charged colloids in alternating electric fields. *The European Physical Journal Special Topics*, 222(11):2911–2922, 11 2013.

[122] J. Zhou and F. Schmid. Computer simulations of single particles in external electric fields. *Soft Matter*, 11(34):6728–6739, 2015.

[123] R. W. O'Brien and L. R. White. Electrophoretic mobility of a spherical colloidal particle. *Journal of the Chemical Society, Faraday Transactions 2: Molecular and Chemical Physics*, 74:1607–1626, 1978.

[124] R. J. Hunter. *Zeta potential in colloid science: principles and applications.* Academic Pr, London, 3. print edition, 1988.

[125] K. Kang and J. K. G. Dhont. Electric-field induced transitions in suspensions of charged colloidal rods. *Soft Matter*, 6(2):273–286, 2010.

[126] O. D. Velev and K. H. Bhatt. On-chip micromanipulation and assembly of colloidal particles by electric fields. *Soft Matter*, 2(9):738–750, 2006.

[127] K. H. Bhatt and O. D. Velev. Control and modeling of the dielectrophoretic assembly of on-chip nanoparticle wires. *Langmuir*, 20(2):467–476, 2004.

[128] J. Ma, T. Stangner, and F. Kremer. Frequency dependence of the electrophoretic mobility for single colloids as measured using optical tweezers. *Physical Review Fluids*, 2(10):1–13, 2017.

[129] E. Delatour and M. Hanss. Apparatus for alternating fields microelectrophoresis. *Review of Scientific Instruments*, 47(12):1531–1535, 1976.

[130] C. Schneider, M. Hanisch, B. Wedel, A. Jusufi, and M. Ballauff. Experimental study of electrostatically stabilized colloidal particles: Colloidal stability and charge reversal. *Journal of Colloid and Interface Science*, 358(1):62–67, 2011.